SUPERNOVA SHRAPNEL:
NEARBY SUPERNOVAE AND DUST TRANSPORT IN THE ISM

BY

BRIAN JOSEPH FRY

DISSERTATION

Submitted in partial fulfillment of the requirements
for the degree of Doctor of Philosophy in Astronomy
in the Graduate College of the
University of Illinois at Urbana-Champaign, 2016

Urbana, Illinois

Doctoral Committee:

Professor Brian D. Fields, Chair
Professor Paul M. Ricker
Professor Leslie W. Looney
Professor Jon J. Thaler

Abstract

The last 2 decades have seen the proposal, detection, and confirmation of live ^{60}Fe radioisotopes from an extra-solar source on Earth, showing an event outside the Solar System directly delivered material to the Earth since its formation. This work examines the possible sources for the ^{60}Fe and models the passage of the material from its source through the Solar System to the ocean floor. We consider the production and deposition on Earth of isotopes with half-lives in the range 10^5 to 10^8 years that might provide signatures of nearby stellar explosions, extending previous analyses of Core-Collapse Supernovae (CCSNe) to include Electron-Capture Supernovae (ECSNe), Super-Asymptotic Giant Branch (SAGBs) stars, Thermonuclear/Type Ia Supernovae (TNSNe), and Kilonovae/Neutron Star Mergers (KNe). We revisit previous estimates of the ^{60}Fe and ^{26}Al signatures, and extend these estimates to include ^{244}Pu and ^{53}Mn. We show that (i) the ^{60}Fe yield rules out the TNSN and KN interpretations, (ii) the ^{60}Fe signals highly constrain a SAGB interpretation but do not completely them rule out, (iii) are consistent with a CCSN origin, and (iv) are highly compatible with an ECSN interpretation.

We also examine various influences on the path of interstellar dust carrying ^{60}Fe from a SN through the Heliosphere, with the aim of estimating the final global distribution on the ocean floor. We study the influences of magnetic fields, angle of arrival, wind and ocean cycling of SN material on the concentrations at different locations. We find that the passage of SN material through the mesosphere/lower thermosphere (MLT) is the greatest influence on the final global distribution, with ocean cycling

causing lesser alteration as the SN material sinks to the ocean floor. SN distance estimates in previous works that assumed a uniform distribution are a good approximation. Including the effects on surface distributions, we estimate a distance of 46^{+10}_{-6} pc for an ECSN progenitor. We note that the SN dust retains directional information to within 1° through its arrival in the inner Solar System, so that SN debris deposition on inert bodies such as the Moon will be anisotropic, and thus could in principle be used to infer directional information.

Lastly, we examine the various influences on the path of dust within a SN remnant (SNR) to determine when/if the dust decouples from the plasma, how much it is sputtered, and where within the ejecta the dust is located. We find that the inclusion of Rayleigh-Taylor (R-T) instabilities are important in studying dust survival as R-T instabilities influence the location of the SN's reverse shock. We also find the presence of a magnetic field within the shocked ISM material will limit the passage of SN dust grains reflecting them or trapping within the heart of the SNR.

This dissertation is dedicated to my wife, Ashley, and my parents, Don and Cindy Fry.

Acknowledgments

I would like to thank my advisor, Brian Fields, and collaborator, John Ellis, for their guidance, assistance, and suggestions in producing all the material contained herein. I would also like to thank my PhD committee members for their suggestions and critiques, and Ryan Foley for his thoughts and discussions regarding supernovae. Lastly, I would like to thank Athol Kemball for sorting through all of the bureaucracy that made it possible to perform this work at Illinois at all.

Chapter 2: We would like to thank Jenny Feige and Shawn Bishop for their discussions regarding the radioisotope measurements, Thomas Johnson and Craig Lundstrom for illuminating discussions of isotope geology, and Friedrich-Karl Thielemann and Ivo Seitenzahl for their informative discussions of supernova radionuclide synthesis.

Chapter 3: We would like to thank Nicole Riemer, Sandip Dhomse, and John M. C. Plane for the their enlightening discussions of aerosols in the atmosphere, and Eric Mamajek for drawing our attention to and discussing his work on the Tuc-Hor group as a strong candidate for the SN site.

Chapter 4: We would like to thank Paul Duffell for his assistance in using the RT1D code, and Shinya Wanajo for kindly sharing his ECSN data.

Table of Contents

List of Tables

List of Figures

Chapter 1

Introduction

Like the basis of a good disaster movie, supernovae (SNe) are powerful, overwhelmingly huge in scale, best viewed from a distance, and unstoppable up-close. It should not be a surprise then that SNe, or simply "exploding stars," have made appearances in such roles on film, inevitably blasting apart some unfortunate planet(s). A basic calculation using a planet's cross-sectional area, gravitational binding energy, and a typical SN explosive energy shows this level of destruction to be extremely unlikely, but the fascination with SNe continues.[1]

SNe have been getting humanity's attention for at least the last 1000 years, such as SN1006 and SN1054 (the number refers to the year it was observed) appearing as "guest" stars to astronomers of yesteryear (Green, 2000; Zhao et al., 2006). These bright spots of light in the sky have been benign introductions to one of the universe's most destructive events. In the last couple centuries, modern technology has allowed us examine the remnants of these explosions as they expand, and understand that SNe represent the catastrophic destruction of a star.[2]

Our modern concept of nuclear physics has also allowed us to understand the creation that also occurs within the star. As a massive star (about eight or more times the mass of the Sun, $\gtrsim 8M_{\odot}$) goes through its life, it assembles increasingly heavier elements, taking simple hydrogen (H) atoms and building up to iron (Fe) and nickel (Ni) using the enormous heat and pressure caused by its own mass and gravity. Towards the end of its life, the star will have a stratified structure like an onion, with different elements being formed in each layer, and it is this process that keeps the star from collapsing under its own weight. Eventually, the energy release reaches a limit at Fe-Ni, and at this point, without a SN, the new, heavy elements would be trapped

[1]For example, in order for the Earth to be destroyed in such a manner, the SN would have to be about 14 AU away. The Sun is not nearly massive enough to explode as a SN, and any star that is would likely be greater than 14 AU in radius, so basically, the Earth is fine.

[2]SNe can be generally separated into two categories: a thermonuclear SN (TNSN, also referred to as a Type Ia SN) and a core-collapse SN (CCSN, also referred to as Type Ib, Ic, or II SN). A TNSN is caused by runaway fusion of a white dwarf (WD), and a CCSN is the explosion of a massive star. This introduction exclusively refers to the later case.

within the star. But the SN scatters a huge portion of these new elements, leaving behind a neutron star (NS, or possibly a black hole, BH, depending on how massive the star was). In addition, as the shock wave of the SN propagates through the star, it is powerful enough to generate elements heavier than Fe, like copper (Cu), silver (Ag), and gold (Au), or possibly super-heavy elements like thorium (Th), uranium (U), and plutonium (Pu). This creative side of the SN generates new elements and delivers them back into space, some eventually making their way to the paper or computer screen you are reading this on. Your/mine/our connection with SNe is where this dissertation focuses.

In his book, *Death From the Skies!: The Science Behind the End of the World*, Philip Plait (2009) describes in great detail how SNe are a hazard to your health; however, the possibility of a SN hazard dates back to Schindewolf (1954), Shklovskii & Sagan (1966), and Ruderman (1974). The study by Alvarez et al. (1980) found that the mass extinction of dinosaurs at the Cretaceous-Tertiary transition was caused by a giant impactor rather than a SN, but the possibility with other past mass extinctions is still an open question (for recent references, see, e.g., Melott & Thomas, 2011; Beech, 2011; Dartnell, 2011; Atri & Melott, 2014; Thomas et al., 2016). SN occur at a rate of $\sim 1-3$ per century in our galaxy (e.g., Adams et al., 2013, and references therein), and we see massive stars nearing the end of their life cycles (e.g., η Carinae, Betelgeuse, Antares) and SN remnants (e.g., Vela, Geminga) in relatively close proximity to Earth (≤ 300 pc). The Geminga pulsar located ~ 250 pc away (Faherty et al., 2007) is the remnant of a SN explosion estimated to have occurred ~ 300 kyr ago, and may be partly responsible for the low density of the interstellar medium (ISM) around the Solar System (Bignami & Caraveo, 1996). Similarly, ^{26}Al gamma-ray line emission and large-angle Hα filaments suggest a SN towards the Antlia constellation $60 - 240$ pc away (McCullough et al., 2002). If this event created a neutron star associated with the high-proper-motion pulsar PSR J0630-2834, then the explosion occurred about 1.2

Myr ago at about 140 pc (Tetzlaff et al., 2013). Even if the SN is not close enough to cause a mass extinction, it may still be close enough to splash the Earth will debris from the explosion. It is reasonable to expect that at some point in Earth's history, one (probably more) SN events have occurred close enough to have a detectable effect on the Earth.

As mentioned above, you and I are made of leftovers from SNe; the iron in our blood was created in an exploding star, but this could have occurred before the Solar System was formed or afterwards. In order to look for recent activity, Ellis et al. (1996); Korschinek et al. (1996) surveyed possible isotope signatures of a nearby SN explosion and suggested searching for terrestrial signatures of ^{60}Fe and/or ^{244}Pu. These isotopes are special because, first, they are radioactive with long lifetimes ($\tau_{1/2} \sim$ Myr) meaning any ^{60}Fe and ^{244}Pu that existed when the Solar System formed has long decayed away, and second, because they are not manufactured within the Solar System.[3] If any ^{60}Fe or ^{244}Pu[4] are detected, we know they had to have come from outside of the Solar System. Motivated by this study, Knie et al. (1999) searched for an anomaly in the ^{60}Fe abundance in a deep-ocean ferro-manganese (Fe-Mn) crust, and found and excess within the past 5 Myr. In the expanded study by Knie et al. (2004), a distinctive ^{60}Fe spike was detected $\sim$ 2.2 Myr ago. Although primordial Solar System composition shows enrichment from extra-solar origins, to our knowledge, this is the first such specific extra-solar event to be identified.

In the following years, the study of near-Earth SN has expanded on three fronts: measuring radioisotopes to further characterize the detection, observational studies to identify the source of the ^{60}Fe, and theoretical studies identifying the relevant physics/chemistry necessary to describe the journey of the ^{60}Fe from the source to Earth and the consequences of the theory, with considerable overlap between each

[3]It is possible to make ^{60}Fe with cosmic rays onto Fe-Ni meteorites, but these are trace amounts that can be accounted for.

[4]The same is true for ^{26}Al, ^{41}Ca, and ^{53}Mn as well as some other isotopes.

front. Fields & Ellis (1999) interpreted the initial detection, and possible corroborating isotope signatures were discussed in Fields et al. (2005). The measurement studies continued with Fitoussi et al. (2008) confirming the detection of Knie et al., and expanded into sea sediment studies. Benítez et al. (2002) proposed that the event arose in the Sco-Cen OB association,[5] which was $\sim$ 130 pc away at the time of the ^{60}Fe-producing event (Preibisch & Mamajek, 2008). Fields et al. (2008) presented hydrodynamic models for the SN blast impact with the solar wind, and Benítez et al. (2002); Athanassiadou & Fields (2011) highlighted the importance of the ejecta condensation into dust grains.

In recent years, isotope studies have not found detections using other radioisotopes like ^{244}Pu (Wallner et al., 2000, 2004, 2015a) or ^{26}Al (Feige et al., 2013; Feige, 2014), but continue to find not only terrestrial ^{60}Fe (Feige, 2014; Wallner et al., 2016), but also lunar ^{60}Fe (Fimiani et al., 2016). Additionally, cosmic ray studies by Kachelrieß et al. (2015) and Savchenko et al. (2015) have found a signature suggesting an injection of cosmic rays associated with a SN occurring $\sim$2 Myr ago, and the discovery of ^{60}Fe in cosmic rays by Binns et al. (2016) suggest a SN origin within the last $\sim$ 2.6 Myr located $\lesssim$ 1 kpc of Earth. Studies of the Sco-Cen OB association by Breitschwerdt et al. (2012, 2016) have examined the SN history of the association showing SN shocks could have reached to the Solar System. The recently discovered Tuc-Hor association (Zuckerman & Webb, 2000; Zuckerman et al., 2001) is $\sim$ 45 pc away, and an examination of Tuc-Hor by Mamajek (2016) presented it as an additional possible source for the ^{60}Fe signal.

The following dissertation details my research examining the theoretical aspects of a near-Earth SN. Chapter 2 contains my study of the possible sources of the extra-solar ^{60}Fe, and shows that the most likely source was, in fact, a SN. Specifically, the

[5] An OB association is a group of O-type and B-type stars that move together. Basically, it's a gang of really bright, massive stars.

source was most likely and Electron-Capture SN (ECSN, a special sub-set of core-collapse SNe from a star $8 - 10\ M_{\odot}$), and details the likely time-resolved ^{60}Fe profile from such a SN. Chapter 3 examines the processes encountered by dust carrying ^{60}Fe after entering the Solar System, and leads to a better understanding of how to best interpret the ^{60}Fe measurements. This study details the journey of the ^{60}Fe through the atmosphere to the ocean floor, showing that the atmosphere completely removes any direction information the dust may have had upon entering the Solar System, but such information should be retained in lunar samples. Chapter 4, is my current work on the movement of dust within a SNR and examines the processes encountered by dust after they are created until they reach the Solar System. Preliminary results suggest an accurate description of the SN's reverse shock, including Rayleigh-Taylor instabilities are extremely important, as well as knowledge of the magnetic field within the SN remnant. Lastly, Chapter 5 will outline my future work efforts and open questions. Each chapter has a separate introduction that outlines more specific background to that particular study, but the overarching theme of this dissertation is describe how the ^{60}Fe from SN(2.2 Myr BCE) came to the Earth.

Chapter 2

Astrophysical Shrapnel: Discriminating Among Near-Earth Stellar Explosion Sources of Live Radioactive Isotopes

This chapter was published in the The Astrophysical Journal under the authorship Fry, B., Fields, B., & Ellis, J.

2.1 Introduction

The most violent stellar explosions are the sources of most of the heavy elements on Earth, and supernovae (SNe) in particular are estimated to occur at a rate of $\sim 1-3$ per century in our Galaxy (e.g., Adams et al., 2013, and references therein). It is inevitable that, over the course of geological time, some such explosions will have occurred within $\sim$ 100 pc of the Earth, close enough to have deposited some ejecta on the Earth and Moon (e.g., Shklovskij, 1969; Fields, 2004, and references therein). Indeed, the Geminga pulsar located $\sim$ 250 pc away (Faherty et al., 2007) is the remnant of a SN explosion estimated to have occurred $\sim$ 300 kyr ago, and may be partly responsible for the low density of the interstellar medium (ISM) around the Solar System (Bignami & Caraveo, 1996). Similarly, ^{26}Al gamma-ray line emission and large-angle Hα filaments suggest a SN towards the Antlia constellation $60-240$ pc away (McCullough et al., 2002); if this event created a neutron star associated with the high-proper-motion pulsar PSR J0630-2834, then the explosion occurred about 1.2 Myr ago at about 140 pc (Tetzlaff et al., 2013). The question then arises whether some closer astrophysical explosion might have left detectable traces on the Earth itself in the form of geological isotope anomalies. Moreover, with a closer astrophysical explosion, the possibility for biological damage, even a mass extinction arises (for recent references, see, e.g., Melott & Thomas, 2011; Beech, 2011; Dartnell, 2011; Atri & Melott, 2014).

Discussions of this possibility date back to the pioneering study of Alvarez et al. (1980). These authors discovered an iridium anomaly associated with the Cretaceous-Tertiary transition that they argued could not, in fact, be associated with a SN explosion, but instead with a giant impact. Subsequently, Ellis et al. (1996) surveyed possible isotope signatures of a nearby SN explosion, including ^{26}Al, ^{53}Mn, ^{60}Fe, and ^{244}Pu. Motivated by this study, Knie et al. (1999) searched for an anomaly in the ^{60}Fe abundance in a deep-ocean ferro-manganese (Fe-Mn) crust, and found one that

appeared ~ 2.2 Myr ago. Although primordial Solar System composition shows enrichment from extra-solar origins, to our knowledge, this is the first such specific extra-solar event to be identified. Following the Knie et al. (1999) discovery, its interpretation was discussed in Fields & Ellis (1999) and possible corroborating isotope signatures were discussed in Fields et al. (2005). Benítez et al. (2002) proposed that the event arose in the Sco-Cen OB association, which was ~ 130 pc away at the time of the ^{60}Fe-producing event. Fields et al. (2008) presented hydrodynamic models for the SN blast impact with the solar wind, and Athanassiadou & Fields (2011) highlighted the importance of the ejecta condensation into dust grains.

The ^{60}Fe signal has subsequently been confirmed in another Fe-Mn crust sample (Knie et al., 2004; Fitoussi et al., 2008) and in lunar regolith (Cook et al., 2009; Fimiani et al., 2012, 2014), but no other accompanying isotope anomaly has been found in studies of ^{26}Al abundances (Feige et al., 2013). Searches for ^{244}Pu have produced just a single count, albeit with no stable isobar background (Wallner et al., 2000, 2004).

In this paper, we broaden our previous analyses in four ways. In a first step, we provide yields for isotopes from the CCSNe considered previously and extend our analysis to include the cases of ECSNe, TNSNe (also known as a Type Ia SN), KNe (also known as Neutron Star Mergers), and SAGBs, which have not been considered previously in this context. For this paper, we distinguish between ECSNe and the more massive CCSNe since there are qualitative differences in the collapse and explosion mechanism as well as nucleosynthesis of these two classes. Secondly, we revisit the formalism surrounding the deposition calculations, including the impact and some geology of the uptake factor, and also the possibility of using sediments to get time-resolved signals and give predictions for these profiles. We also discuss the filtering processes impacting the transport of the signal via dust. Next, we discuss the compatibility between the terrestrial and lunar evidence for a ^{60}Fe anomaly, and we

also analyze the existing limits on the ^{26}Al abundance from samples bracketing the ^{60}Fe anomaly. In combination with these previous steps, as a fourth and final step, we survey the possible interpretations of the ^{60}Fe anomaly and make predictions for upcoming measurements.

We find that a TNSN and a KN would yield too little ^{60}Fe, and can be ruled out as possible sources for the Knie et al. (2004) ^{60}Fe signal. Additionally, we find a SAGB source constrained, but not eliminated due to uncertainty in the Local Bubble's magnetic field and the location of a possible SAGB source. CCSNe from our set of masses and ECSNe can not be ruled out based on the available measurements.

2.2 Progenitors and Delivery to the Solar System

Previous papers have focused on CCSNe as the likeliest progenitor for the ^{60}Fe signal. However, there are other astrophysical ejections that are thought to produce ^{60}Fe but have not been considered previously. These include TNSNe, ECSNe, KNe, and SAGBs. Table 2.1 summarizes the yields for possible CCSNe, ECSNe, and SAGBs progenitors as used in our model calculations; yields are expressed in units of $M_{\odot}$.

2.2.1 Supernovae

SNe include both CCSNe and TNSNe; CCSNe are the results of massive stars completing Fe/Ni fusion in their cores and collapsing under the influence of gravity whereas TNSNe result from runaway nuclear fusion in a C-O white dwarf near its Chandrasekhar limit. Both types have similar explosive energies and modes of transporting ejecta. However, although known to be sources of stable iron isotopes, TNSNe are calculated to produce relatively little ^{60}Fe, namely $\sim 2.3 \times 10^{-9}$ $M_{\odot}$, according to the W7 Type Ia Model of Nomoto, Thielemann & Yokoi (1984). ECSNe form a special

subcategory of CCSNe with significantly different radioactive isotope yields. While the ^{60}Fe yields for CCSNe and ECSNe are similar ($\sim 10^{-6} - 10^{-3}\ M_{\odot}$, Rauscher et al., 2002; Limongi & Chieffi, 2006), their yields for other isotopes (e.g., ^{26}Al and ^{53}Mn) are vastly different (Wanajo et al., 2013). For the purposes of this paper, ECSNe will refer to SNe from $8 - 10\ M_{\odot}$ stars, CCSNe will refer to SNe with progenitor masses $> 10\ M_{\odot}$, and SNe will refer to CCSNe, ECSNe, and TNSNe. It should be noted that the yields for ^{244}Pu were calculated using the same method from Fields et al. (2005); the proportions of r-process elements are generally consistent to that found in metal-poor globular clusters and in the Sun. In this paper, however, the yields for ^{244}Pu were based on the yields for ^{182}Hf from Rauscher et al. (2002) using the ratios given in Fields et al. (2005).

SNe can show large variations in their isotope yields. TNSN ^{60}Fe yields show variations over several orders of magnitude ($\sim 10^{-18} - 10^{-7}\ M_{\odot}$) due to variations in the number and location of ignition points and the transition from deflagration to detonation (Seitenzahl et al., 2013).[1] CCSNe/ECSNe yields are highly dependent on a number of factors including when different layers are mixed. This can be seen in the variations of yields from one mass to another (Rauscher et al., 2002). The yields within a given mass are also subject to uncertainties in nuclear reaction rates (3-α and ^{12}C(α,γ)^{16}O) which can lead to an almost order of magnitude shift in the production of ^{26}Al and ^{60}Fe (Tur et al., 2010). In §4.6, Figure 2.3, we show the calculated distances with uncertainties indicated by dashed lines for a factor of 5 variation in the ^{60}Fe yield for each CCSN/ECSN type.

Fiducial parameters for the explosions and the interstellar medium are chosen as follows: We assume CCSNe and TNSNe deposit $E_{\mathrm{CCSN\ \&\ TNSN}} = 10^{51}$ erg into their ejecta, while ECSNe deposit $E_{\mathrm{ECSN}} = 10^{50}$ erg (Wanajo et al., 2009). Because

[1] We adopt a fiducial TNSN ^{60}Fe yield of $\sim 10^{-9} M_{\odot}$, which is consistent with the classic W7 result (Nomoto, Thielemann & Yokoi, 1984) and is larger than almost all Seitenzahl et al. (2013) models.

the Local Bubble shows evidence of multiple SN explosions, we will assume that if a SN were the source of the ^{60}Fe signal, it would be the most recent SN, meaning the SN occurred in an already depleted ISM, but not as depleted as the current density of the Local Bubble (i.e., $n_{\text{Average ISM}} = 1.0$ cm^{-3} $> n_{\text{ISM}} > n_{\text{Local Bubble}} = 0.005$ cm^{-3}). Therefore, we estimated a SN would have occurred in an ISM of density, $n_{\text{ISM}} = 0.1$ cm^{-3}, temperature, $T = 8000$ K, and sound speed, $c_s = 10$ km s^{-1} (i.e., approximate values for the Local Cloud, Fields et al., 2008).

2.2.2 Kilonovae

KNe are thought to result from Neutron Star-Neutron Star (NS-NS) or in some cases Neutron Star-Black Hole (NS-BH) mergers (Li & Paczyński, 1998; Metzger et al., 2010; Tanvir et al., 2013). For this paper, we only consider the KN explosion's lower-energy, spherical/torical ejection and not its highly beamed gamma-ray burst jet. The rapid decompression and ejection of neutron-rich NS matter makes these events a natural site for the r-process (Lattimer & Schramm, 1974; Symbalisty & Schramm, 1982). While KNe are less energetic than SNe ($E_{\text{KN}} = 10^{49}$ erg, Goriely et al., 2011), we will consider a possible KN source of the ^{60}Fe signal as occurring in the same ISM conditions as a SN. However, given the axisymmetric nature of NS-NS mergers, we will not apply the same constraints to KNe as SNe, but will instead evaluate KNe with respect to isotope yields and frequency.

While there has been some modeling of KN yields, none we are aware of have specifically stated a yield for ^{60}Fe. However, it is possible to determine an upper limit on the range for a KN. In Goriely et al. (2011), they list mass fractions for every atomic number up to ~ 200 for a NS-NS merger with a total merger mass of 2.7 $M_{\odot}$. If we assume all of the isotopes with $A = 60$ are in the form of ^{60}Fe ($M_{\text{ej,total}} = 10^{-3} - 10^{-2}$, $X_{^{60}\text{Fe}} = 10^{-5}$) then the upper limit to the mass of ejecta in ^{60}Fe is 10^{-7} $M_{\odot}$.

2.2.3 Super-Asymptotic Giant Branch Stars

SAGBs ($6.5 - 9\ M_\odot$) are post-main sequence stars that produce large amounts of dust (see, e.g., Ventura et al., 2012) and have strong winds (~ 30 km s^{-1}) capable carrying dust great distances. SAGBs produce $10^{-6} - 10^{-5}\ M_\odot$ of ^{60}Fe (Doherty et al., 2013), but are distinguishable from SNe in that they produce practically no ^{53}Mn (Wasserburg et al., 2006; Fimiani et al., 2014). We note that SAGB yields are subject to an uncertainty in the onset of the super-wind phase (Doherty et al., 2013); a delayed onset results in generally increased yields. The implication for distance is shown with dashed error bars on SAGB results in §4.6, Figure 2.3. In contrast to SNe, we do not expect a SAGB wind to affect the density of the Local Bubble appreciably, and we assume that a SAGB source for the ^{60}Fe signal would have occurred in an ISM like that found in the Local Bubble today (i.e., $n_{\rm ISM} = 0.005$ cm^{-3}, temperature, $T = 10^6$ K, and sound speed, $c_s = 100$ km s^{-1}). Finally, we assume the initial velocity of the SAGB grains to be: $v_{\rm grain,0} = 30$ km s^{-1}.

2.2.4 Dust Transport to the Solar System

Regardless of the source, any ^{60}Fe arriving in the Solar System will need to be in the form of dust. Fields et al. (2008) showed that the solar wind will keep any gaseous isotopes from reaching the Earth (unless a SN is sufficiently close, but this will be used as a constraint later in §2.3.1 and §4.6). We assume that the dust grains are spherical and select as our fiducial values for dust grains: density, $\rho_{\rm grain} = 3.5$ g cm^{-3} (an average value for silicates), radius, $a = 0.2\ \mu$m (this selection is based on discussion in §2.4.2), and voltage, $\mathcal{V} = 0.5$ V. Departures from these values will be specifically stated.

2.3 Formalism

In order to identify the most likely progenitor, we will attempt to constrain the source and its allowable distances using the measured ^{60}Fe fluence and calculated yields. In the future, with additional measurements of other isotopes, we can use the other isotope yields to constrain the source using the observed isotope to ^{60}Fe ratio.

Several previous works have presented the formalism for calculating deposited material from a SN (Ellis et al., 1996; Fields & Ellis, 1999; Fields et al., 2005). These works focused primarily on short ranges (SN distances, $D \sim 10$ pc) and on the isotope ^{60}Fe. For such short distances, the losses due to decay of live radionuclides en route from the SN to Earth amount to $\lesssim 1\%$ and can be ignored. At greater ranges ($D \sim 100$ pc) and for shorter-lived isotopes (in particular, ^{26}Al with $\tau_{1/2,^{26}\mathrm{Al}} = 0.717$ Myr) decays en route become a significant issue. Accounting for this, the observed fluence today, $\mathcal{F}_{\mathrm{obs},i}$, for each isotope, i, in atoms per area on the surface of the Earth within a given substance (e.g., crust, sediment, etc.) becomes:

$$\mathcal{F}_{\mathrm{obs},i} = \left(\frac{1}{4}\right)\left(\frac{M_{\mathrm{ej},i}}{4\pi D^2 A_i m_u}\right) U_i \; f_i \; e^{-(t_{\mathrm{arr}}+t_{\mathrm{travel}})/\tau_i} \tag{2.1}$$

where $M_{\mathrm{ej},i}$ is the mass of the ejecta by isotope, D is the distance from the progenitor to Earth, A_i is the atomic number of the isotope, m_u is the atomic mass unit, t_{arr} is the time from today since the ejecta arrived at Earth, and t_{travel} is the time the ejecta traveled from the source to Earth. Also, τ_i is the mean lifetime of the isotope ($\tau_i = \tau_{1/2,i}/\ln 2$).

The uptake, $U_i \equiv$ (Amount Collected)/(Amount Deposited), is the fraction of the isotope deposited on a surface that is collected by that material. The quantity is dimensionless, and ranges from 1 (the material collects 100% of deposited element) to 0 (the material collects 0% of deposited element).[2] It is further discussed in §2.4.1.

[2]It is possible to have $U_i > 1$ if, for example, a marine sample can chemically scavenge the element

Additionally, the dust fraction, f_i, is the amount of the isotope in the form of dust that arrives at Earth (§2.4.2). It is similar to uptake in that it is also dimensionless and ranges from 1 (all of the isotope is in the form of dust and reaches Earth) to 0 (none of the isotope is dust and/or reaches Earth). There is a factor of (1/4) from the ratio of the Earth's cross sectional to surface areas, because it is assumed material is distributed evenly over Earth's entire surface through collisional accretion only. Equation (2.1) also assumes an isotropic dispersal of material from the source ($4\pi D^2$ factor for spherical distribution), that no additional isotopes are created after the ejection from the progenitor, and that the ejected material passes through a homogeneous ISM.

There are three other fluence quantities that appear in the literature: "decay-corrected" fluence, "surface" fluence, and "interstellar" fluence. The decay-corrected or arrival fluence, $\mathcal{F}_{\mathrm{arr},i}$, is the total number of atoms per area that would have been measured at the time the signal arrived. It is calculated by correcting our previous description of fluence (see Equation (2.1)) for radioactive decay since the isotope was deposited $\mathcal{F}_{\mathrm{arr},i} = e^{t_{\mathrm{arr}}/\tau_i}\mathcal{F}_{\mathrm{obs},i}$. The surface fluence or global mean fluence, $\mathcal{F}_{\mathrm{surface},i}$, is the total number of atoms per area that arrive at the surface of the Earth regardless of what substance they might be incorporated into, and is found by dividing the decay-corrected fluence by the uptake (i.e., $\mathcal{F}_{\mathrm{surface},i} = \mathcal{F}_{\mathrm{arr},i}/U_i$). It will be used in §2.5 and §4.6 and will be specifically stated when used. The interstellar fluence, $\mathcal{F}_{\mathrm{interstellar},i}$, also appears in the literature (e.g., Fitoussi et al., 2008; Cook et al., 2009), namely the number of atoms per area on the surface of the spherical shock front. It is related to the surface fluence by a factor of 4, the ratio of Earth's cross section to surface area (i.e., $\mathcal{F}_{\mathrm{interstellar},i} = 4\mathcal{F}_{\mathrm{surface},i}$). Interstellar fluence will not be used in this paper, but the reader should be aware of the distinction when reviewing the literature.

In order to find the time delay, t_{travel}, from ejection to deposition on Earth, we

of interest so efficiently that it collects more than the amount deposited in the water column directly over the sample.

must account for the propagation of the ejection through the intervening ISM, which depends on the progenitor. SNe transmit material via an explosive shock, whereas SAGBs use a wind-driven ejection. In the case of SNe, we will assume that the shock has transitioned from the free-expansion phase into the adiabatic/energy-conserving phase. For SAGBs, we will assume dust has been blown by winds from the star and experiences drag as it travels to Earth.

2.3.1 SN Expansion Profile and Constraints

For SNe in the adiabatic/energy-conserving phase, the shock follows a self-similar or Sedov-Taylor expansion profile. With the explosion at time $t = 0$, a shock is launched with radius, $R_{\rm SN}$, at elapsed time, t, given by:

$$R_{\rm SN} = \xi_0 \left(\frac{E_{\rm SN} t^2}{\rho_{\rm ISM}} \right)^{1/5} \tag{2.2}$$

for a SN explosion depositing energy $E_{\rm SN}$ into the ejecta, propagating into a local interstellar medium of density $\rho_{\rm ISM} = m_u n_{\rm ISM}$. The quantity ξ_0 is a dimensionless constant that is of order unity for $\gamma = 5/3$ using the derivation in Zel'dovich & Raizer (1967). Thus the time interval to traverse distance, D, is:

$$t_{\rm travel,SN} = \left(\frac{D}{\xi_0} \right)^{5/2} \left(\frac{\rho_{\rm ISM}}{E_{\rm SN}} \right)^{1/2} \tag{2.3}$$

where we have assumed a uniform ISM density. While we know this is a crude approximation (see e.g., Abt, 2011), deviations from the uniform case would be encoded into the signal and could be determined if the signal is time-resolved (for examples of non-uniform media, see Book, 1994). We use the uniform ISM case as a baseline.

The density versus radius profile for a SN signal may be approximated by a "saw-tooth" profile. As will be described in greater detail in §2.3.3, §2.3.4, and Appendix

2.9, measurements in sediment open the possibility to making time-resolved fluence measurements. A saw-tooth pattern gives a better approximation of the more exact Sedov solution than a uniform shell profile. The saw-tooth pattern reaches its maximum density value at the outer edge of the shock, then decreases linearly to a fraction of the total shock radius, ϵ, where the density is zero from that point to the center of the remnant. See Appendix 2.9 for a comparison of the exact Sedov, saw-tooth, and uniform shell profiles.

Possible SNe will be constrained by an inner "kill" distance and an outer "fade-away" distance. The kill distance is the range at which a SN can occur and create extinction-level disruptions to the Earth's biosphere. The primary mechanism for a SN to accomplish this is for ionizing radiation (i.e., gamma-rays, hard X-rays, and cosmic-rays) to destroy O_3 and N_2 in the atmosphere producing nitric oxides (NO_y) and leaving the biosphere vulnerable to UVB rays from the Sun (first described by Shklovskii & Sagan, 1966, described in detail by Ruderman 1974, and updated by Ellis & Schramm 1995). This can be accomplished either by direct exposure (i.e., an X-ray flash from the SN) or by a "descreening" boost in cosmic-ray flux.[3] Gehrels et al. (2003) calculated a kill distance $R_{\rm kill} \lesssim 8$ pc for the direct exposure case using the galactic gamma-ray background and SN rates, although, as pointed out by Melott & Thomas (2011), this is probably an underestimation based on more recent rate estimations. This work was expanded upon by Ejzak et al. (2007) and Thomas et al. (2008) to include X-rays and showed that for exposure durations up to 10^8 s, the effects on the biosphere were the same and that the critical value for an extinction-level SN event was an energy fluence of 10^8 erg cm^{-2} (not to be confused with the description of fluence used throughout the rest of this paper). As noted in Melott & Thomas (2011), these direct exposure calculations use SN rate and photon and cosmic-ray emission

[3]Note, our kill distance does not include the case of a gamma-ray burst given their narrowly-beamed emission.

information that are improving, but still subject to large uncertainties.

Here we calculate the kill distance using the descreening case described in Fields et al. (2008); it yields the same range as the direct exposure calculations, and is scalable to the energy of the SN, $E_{\rm SN}$. The descreening kill distance is the range at which a SN can occur and its shock will penetrate the Solar System to within 1 AU of the Sun. It is determined by setting the solar wind pressure, $P_{\rm SW}$, equal to the pressure of the SN shock (see, e.g., Fields et al., 2008). In this case, the pressure from the SN has little effect on the Earth, but by pushing back the solar wind, the Earth is inside the SN remnant and now directly exposed to the SN cosmic-rays that would normally diffuse out over 10^4 yr (Fujita et al., 2010) in addition to an increased galactic cosmic-ray background. In-turn, these destroy O_3 and N_2 in the atmosphere, just as in the direct exposure case, in addition to increased radionuclide deposition (Melott & Thomas, 2011). Using our fiducial SN values, we find:

$$R_{\rm kill} = 10 \text{ pc } \left(\frac{E_{\rm SN}}{10^{51} \text{ erg}}\right)^{1/3} \left(\frac{2 \times 10^{-8} \text{ dyne cm}^{-2}}{P_{\rm SW}}\right)^{1/3} \tag{2.4}$$

The fadeaway distance is the range at which the SN shock dissipates and slows to the sound speed of the ISM. Because of uncertainty in when SN dust decouples from the rest of the shock, the fadeaway distance is not an absolute limitation like the kill distance, but can serve as a guide to the likelihood of a progenitor. Using the derivation from Draine (2011, Eq. 39.31), we find:

$$R_{\rm fade} = 160 \text{ pc } \left(\frac{E_{\rm SN}}{10^{51} \text{ erg}}\right)^{0.32} \left(\frac{0.1 \text{ cm}^{-3}}{n_{\rm ISM}}\right)^{0.37} \left(\frac{10 \text{ km s}^{-1}}{c_s}\right)^{2/5} \tag{2.5}$$

2.3.2 SAGB Expansion Profile and Constraints

In the case of SAGBs, we assume the dust is ejected radially and that the distance traveled by SAGB dust is determined only by a drag force, $F_{\rm drag}$ (magnetic forces will

be considered later in this section as a constraint). Using the description in Draine & Salpeter (1979), the drag force due to only collisional forces (in cgs units) is:[4]

$$F_{\rm drag} = 2\pi a^2 kT \left(\sum_j n_j \left[G_0(s_j) \right] \right) \tag{2.6}$$

with

$$G_0(s) \approx \frac{8s}{3\sqrt{\pi}} \left(1 + \frac{9\pi}{64} s^2 \right)^{1/2}, \quad s_j \equiv \left(m_j v^2 / 2kT \right)^{1/2} \tag{2.7}$$

where j is the respective species in the ISM (we consider only ionized H; He and free electrons will be neglected), m_j is the particle mass of that respective species, k is the Boltzmann constant, T is the temperature of the ISM, and v is the velocity of the particle relative to the medium. For small v (i.e., $v_{\rm grain} \lesssim 100$ km s^{-1}) the first term in G_0 will dominate, leaving $G_0(s) \approx 8s/(3\sqrt{\pi})$. Making these simplifications, we find:

$$F_{\rm drag} = 2\pi a^2 kT n_{\rm ISM} v_{\rm grain} \left(\frac{8}{3\sqrt{\pi}} \right) \left(\frac{m_p}{2kT} \right)^{1/2} = m_{\rm grain} \ddot{R}_{\rm SAGB} \tag{2.8}$$

where $R_{\rm SAGB}$ is the distance the dust grain has traveled from the SAGB, and $v_{\rm grain} \equiv \dot{R}_{\rm SAGB}$. Integrating twice and setting $R_{\rm SAGB}$ equal to the traverse distance from the progenitor to Earth, D, gives the transit interval:

$$t_{\rm travel,SAGB} = -\zeta_0 \left(\frac{a\rho_{\rm grain}}{c_s \rho_{\rm ISM}} \right) \ln \left(1 - \frac{1}{\zeta_0} \frac{c_s \rho_{\rm ISM}}{a \rho_{\rm grain}} \frac{D}{v_{\rm grain,0}} \right) \tag{2.9}$$

where ζ_0 is a dimensionless constant and of order unity for $\gamma = 5/3$, c_s is the sound speed in the ISM, and $v_{\rm grain,0}$ is the initial velocity of the dust grain when it leaves the SAGB.

We approximate the density profile for a SAGB signal by a uniform shell or "top-hat" shape (we will use "top-hat" profile to avoid confusion with the SN profile dis-

[4]The Coulomb force can be large, however, it is not for our selected grain parameters, so we neglect Coulomb forces (see constraints for $(\phi^2 \ln \Lambda)$ in Draine, 2011, §26.1.1).

cussion). This corresponds to a uniform, steady wind. The top-hat pattern reaches its maximum density value at the leading edge of the signal, retains this value for the duration of the signal, and afterwards the density returns to zero. The SAGB phase is characterized by thermal-pulsing of the star's envelope. Since the duration of each pulse ($\Delta t_{\rm pulse} \sim 1$ yr) and interval between pulses ($\Delta t_{\rm inter} \sim 100$ yr) are much shorter than the SAGB phase ($\Delta t_{\rm SAGB} \sim 100$ kyr $\gg \Delta t_{\rm inter} > \Delta t_{\rm pulse}$) we assume that the amount of ejected material is approximately constant for the duration of the SAGB phase (see Siess, 2010). Furthermore, we assume all parts of the signal experience the same forces from the SAGB to the Earth, so that the duration of the signal remains the same (i.e., $\Delta t_{\rm signal,SAGB} = \Delta t_{\rm SAGB} = 100$ kyr).

Because SAGB winds would not be as devastating to the Earth as a SN shock, we forego establishing an inner kill distance, but establish two outer distances: the drag stopping distance, $R_{\rm drag}$, and the magnetic deflection distance, $R_{\rm mag}$. The distance, $R_{\rm drag}$, is the range of the SAGB dust grains' e-folding velocity, and the $R_{\rm mag}$ is the range at which deflection of the dust grain's trajectory by the ISM's magnetic field becomes significant. Using the derivations from Murray et al. (2004), we find:

$$R_{\rm drag} = 93 \text{ kpc} \left(\frac{\rho_{\rm grain}}{3.5 \text{ g cm}^{-3}}\right) \left(\frac{a}{0.2\ \mu\text{m}}\right) \left(\frac{0.005 \text{ cm}^{-3}}{n_{\rm ISM}}\right) \left(\frac{10^6 \text{ K}}{T}\right)^{1/2} \left(\frac{v_{\rm grain,0}}{30 \text{ km s}^{-1}}\right) \tag{2.10}$$

$$R_{\rm mag} = 0.02 \text{ pc} \left(\frac{\rho_{\rm grain}}{3.5 \text{ g cm}^{-3}}\right) \left(\frac{0.5 \text{ V}}{\mathcal{V}}\right) \left(\frac{5\ \mu\text{G}}{B}\right) \left(\frac{v_{\rm grain,0}}{30 \text{ km s}^{-1}}\right) \left(\frac{a}{0.2\ \mu\text{m}}\right)^2 \tag{2.11}$$

The implications of these limits will be discussed in greater detail in §4.6.

2.3.3 The Radioactivity-based Distance to the Explosion

To estimate the distance, D, to the explosion, we wish to invert Equation (2.1). When the transit time (the time for the shock to travel from the source to Earth) is negligible ($t_{\rm travel} \ll \tau_i$), the procedure is straightforward, since the only distance dependence is

the inverse square dilution of the ejecta, and so $D \propto 1/\sqrt{\mathcal{F}_{\mathrm{obs},i}}$.[5] This has been assumed in work to date. However, if D is sufficiently large, then via Equation (2.2), the distance-dependent transit time can become important and must be included in solving Equation (2.1); we have done this in all of our results.

Another effect occurs when the radioisotope signal is sampled sufficiently finely to resolve the time history of the deposition signal. This occurs when the signal width (the time from the arrival of the signal's leading edge to the departure of the signal's trailing edge) is larger than the sampling time resolution ($\Delta t_{\mathrm{signal}} > \Delta t_{\mathrm{res}}$). In this case, the total radioisotope signal, summed over all time bins, should be used in solving the distance via Equation (2.1); and as we show in §2.3.5 below, the width of $\Delta t_{\mathrm{signal}}$ for a SN probes independently the explosion distance. However, the available Knie et al. (2004) data has a time sampling of $\Delta t_{\mathrm{res}} \sim 880$ kyr, and shows no evidence for a signal that is extended in time. Thus we infer that the signal width $\Delta t_{\mathrm{signal}} \lesssim \Delta t_{\mathrm{res}}$, and indeed we find $\Delta t_{\mathrm{signal}} \lesssim 880$ kyr for most of our possible progenitors. In addition, when solving for distance using the Knie results, we assumed the signal arrived halfway through the sample. Therefore, half of the sampling width is used as a median value rather than assuming the signal arrives right as the sampling window begins or just before it ends.

2.3.4 Expected Behavior of Time-Resolved Signals

Although the time resolution of the deep-ocean ^{60}Fe crust measurements in Knie et al. (2004) data preclude resolution of the time structure of the radioisotope deposition, measurements in sediments can achieve much better time resolution, and so it is of interest to explore the time dependence of the explosion signal. Such work was pioneered by Ammosov et al. (1991) in the context of the ^{10}Be anomalies ~ 35 and 60

[5] This "radioactivity distance" is analogous to the usual luminosity distance: the yield plays the role of luminosity, and radioisotope fluence the role of flux (Looney et al., 2006).

kyr ago in Antarctic ice cores (Raisbeck et al., 1987).

In developing a model for deposition, we examine a Sedov-Taylor profile for a SN shock (a similar examination could be done for the SAGB case if we had more detailed description of its signal width dependence), which implies an energy-conserving (adiabatic) evolution. This also means the shock will remain self-similar as it progresses and that the majority of the material is concentrated near the leading edge. Although the remnant density profile changes once the remnant transitions to the radiative/momentum-conserving phase, we have chosen to maintain the Sedov profile. We did this, firstly, because the profiles are similar in shape (the radiative profile is a thicker shell profile, see, e.g., Shu, 1992, Figure 17.4). Secondly, because the dust will decouple from the gas at some point, either when the shock meets back pressure from encountering the solar wind or at the transition from the adiabatic to the radiative phase when the shock loses its internal radiation pressure (Draine, 2011). The exact nature of this decoupling and resulting profile would require detailed calculations that are beyond the scope of this paper.

We assume that the explosion ejecta are well-mixed within the swept-up matter, so that the ejecta density profile follows that of the blast itself. As described in Appendix 2.9, we approximate the Sedov density profile as a "saw-tooth" that drops linearly from a maximum behind the shock radius $R_{\rm SN}$ to zero at an inner radius $r_{\rm in} = (1-\epsilon)R_{\rm SN}$, with $\epsilon \approx 1/6$. We note that the leading edge of the blast from an event at distance D arrives at a time $t_{\rm travel}$ since the explosion which corresponds to geological time $t_{\rm arr}$; this is given by $D = R_{\rm SN}(t_{\rm arr})$, whereas the trailing edge of the shell arrives at time $t_{\rm dep}$ given by $D = (1-\epsilon)R_{\rm SN}(t_{\rm dep})$. Thus we have $t_{\rm dep} = t_{\rm arr}/(1-\epsilon)^{5/2}$.

With these assumptions we can model the global-averaged flux time profile, $\mathbb{F}$. For radioisotope i, we have:

$$\mathbb{F}_i(D,t) = \left(\frac{t}{t_{\rm arr}}\right)^{-11/5} \left[\frac{(t/t_{\rm arr})^{-2/5} - (t_{\rm dep}/t_{\rm arr})^{-2/5}}{1-(t_{\rm dep}/t_{\rm arr})^{-2/5}}\right] \mathbb{F}_i(D,t_{\rm arr}) \qquad (2.12)$$

as shown in Appendix 2.9; note that here all times are geological and thus increase towards the past.[6] This describes a cusp-shaped decline from an initial flux:

$$\begin{aligned}\mathbb{F}_i(D, t_{\rm arr}) &= \frac{2\mathcal{F}_1}{5t_{\rm arr}} = \left(\frac{3}{40\pi}\right)\left(\frac{\gamma+1}{\gamma-1}\right)\left(\frac{M_{{\rm ej},i}}{m_i D^2}\right)\left(\frac{\xi_0^5 E_{\rm SN}}{m_p n_{\rm ISM} D^5}\right)^{1/2} \\ &= 9.5\times10^5 \text{ atoms cm}^{-2} \text{ kyr}^{-1} \\ &\quad\times\left(\frac{0.1 \text{ cm}^{-3}}{n_{\rm ISM}}\right)^{1/2}\left(\frac{E_{\rm SN}}{10^{51} \text{ erg}}\right)^{1/2}\left(\frac{M_{{\rm ej},i}}{3\times10^{-5}\ M_\odot}\right)\left(\frac{60}{A_i}\right)\left(\frac{100 \text{ pc}}{D}\right)^{9/2}\end{aligned} \tag{2.13}$$

where the numerical values are $m_i = 60 m_u$ and the yield is appropriate for ^{60}Fe.

To test the profile in Equation (2.12), one can fit observed time-resolved data to this form, letting $t_{\rm arr}$ and $t_{\rm dep}$, and $\mathbb{F}_i(D, t_{\rm arr})$ be free parameters. For the Sedov profile, the time endpoints should obey $t_{\rm dep} = t_{\rm arr}/(1-\epsilon)^{5/2}$, which provides a consistency check for the Sedov (adiabatic) approximation. Moreover, as we show in §2.3.5, the interval $t_{\rm dep} - t_{\rm arr}$ provides an independent measure of the explosion distance.

If the radioisotope abundance is sampled over a time interval $[t_1, t_2]$, then the fluence (without radioactive decays) will be the integral of the surface flux over this interval: $\mathcal{F}_i(t_1, t_2) = \int_{t_1}^{t_2} \mathbb{F}_i(t)\ dt$, where we have suppressed the dependence on time-independent parameters such as distance. If the observed time resolution $\Delta t_{\rm res}$ is small compared to $t_{\rm arr}$ and $t_{\rm dep}$, then the fluence profile $\mathcal{F}_i(t - \Delta t_{\rm res}/2, t + \Delta t_{\rm res}/2) \approx \mathbb{F}_i(t)\ \Delta t_{\rm res}$ will recover the flux history.

So far we have calculated the observed fluence without the effect of decay. Since all the atoms were created at the same time, the observed fluence is reduced by a factor $e^{-(t_{\rm arr}+t_{\rm travel})/\tau_i}$. The effects of uptake (§2.4.1) and dust depletion (§2.4.2) introduce

[6] In Equation (2.2) time increases towards the future, but note that elsewhere, unless explicitly stated, times are used in the geological sense, and thus increase towards the past.

further factors of U_i and f_i. We thus arrive at the observed fluence:

$$\mathcal{F}_{\mathrm{obs},i}(t_1, t_2) = U_i f_i e^{-(t_{\mathrm{arr}}+t_{\mathrm{travel}})/\tau_i} \int_{t_1}^{t_2} \mathbb{F}_i(t)\ dt\ . \tag{2.14}$$

One can show that the total integrated fluence $\mathcal{F}_{\mathrm{obs},i}(t_{\mathrm{arr}}, t_{\mathrm{dep}})$ takes precisely the value in Equation (2.1). This reflects the number conservation (aside from decays) of the atoms in the SN ejecta. This also implies that, in a time-resolved measurement, the total fluence is conserved, which means that the area under a fluence vs. time curve will be constant for fixed explosion parameters. This implies that fluence measurements of ^{60}Fe/Fe will show lower values when measured over fewer bins, and finer sampling will show higher fluence over more bins (see Figure 2.1).

2.3.5 A Resolved Signal Timescale Probes the Distance to the Explosion

A time-resolved signal not only encodes information about the shape of the blast density profile, but also about the distance. The relation $D = (1-\epsilon)R_{\mathrm{SN}}(t_{\mathrm{dep}})$ also allows us to write $t_{\mathrm{dep}} = t_{\mathrm{arr}}/(1-\epsilon)^{5/2}$ and thus that:

$$\Delta t_{\mathrm{signal}} = t_{\mathrm{dep}} - t_{\mathrm{arr}} \equiv \alpha t_{\mathrm{arr}} \tag{2.15}$$

where we define a dimensionless parameter, α, that relates the signal width in terms of the arrival time. For our profile, $\alpha = (1-\epsilon)^{-5/2} - 1 \approx 0.577$. We see that the radioisotope width grows in proportion to the blast transit time to Earth, t_{travel}, which itself depends on distance. Thus a measurement of $\Delta t_{\mathrm{signal}}$ from a time resolved radioisotope signal gives an measure of the explosion distance. Within this Sedov

model, $D = R_{\rm SN}(t_{\rm arr})$, and so we can solve for the distance based on "blast timing:"

$$\begin{aligned} D &= \xi_0 \left(\frac{E_{\rm SN} \Delta t_{\rm signal}^2}{\alpha^2 \rho} \right)^{1/5} \\ &= 65 \text{ pc} \left(\frac{\Delta t_{\rm signal}}{100 \text{ kyr}} \right)^{2/5} \left(\frac{E_{\rm SN}}{10^{51} \text{ erg}} \right)^{1/5} \left(\frac{0.1 \text{ cm}^{-3}}{n_{\rm ISM}} \right)^{1/5} \end{aligned} \tag{2.16}$$

This distance measure is independent of the "radioactivity distance" and its associated uncertainties, notably due to uptake, dust fraction, and radioisotope yields. Moreover, as characteristic for Sedov blast waves, the blast-timing distance in Equation (2.16) scales as small powers of the timescale, as well as the energy and density. This will weaken the uncertainties in distance estimate.

Having two independent distance estimates allows a consistency check for the model. Alternatively, if we adopt one of the distance estimates as the correct value, we can deduce the parameters in the other. For example, adopting the blast-timing distance we can use the observed fluence and solve for the product of radioisotope yield, uptake, and dust fraction: $M_{{\rm ej},i} U_i f_i \propto D^2 \, \mathcal{F}_{{\rm obs},i}$. Given a geophysical estimate of uptake, this allows for a measure of the yield and thus a direct probe of the nucleosynthesis output and thus the nature of the explosion (see Figure 2.1 for examples).

2.4 Deposit Factors

The delivery of astrophysical debris to the Solar System and its incorporation into geological and lunar samples is clearly complex. In this section we consider several factors we are aware of that can have a substantial influence on the observed signals.

2.4.1 Uptake

Uptake in the Fe-Mn crust involves a complex chemical process that incorporates material into the crust with a low accumulation rate ~ 2 mm Myr^{-1}. Usual deep-

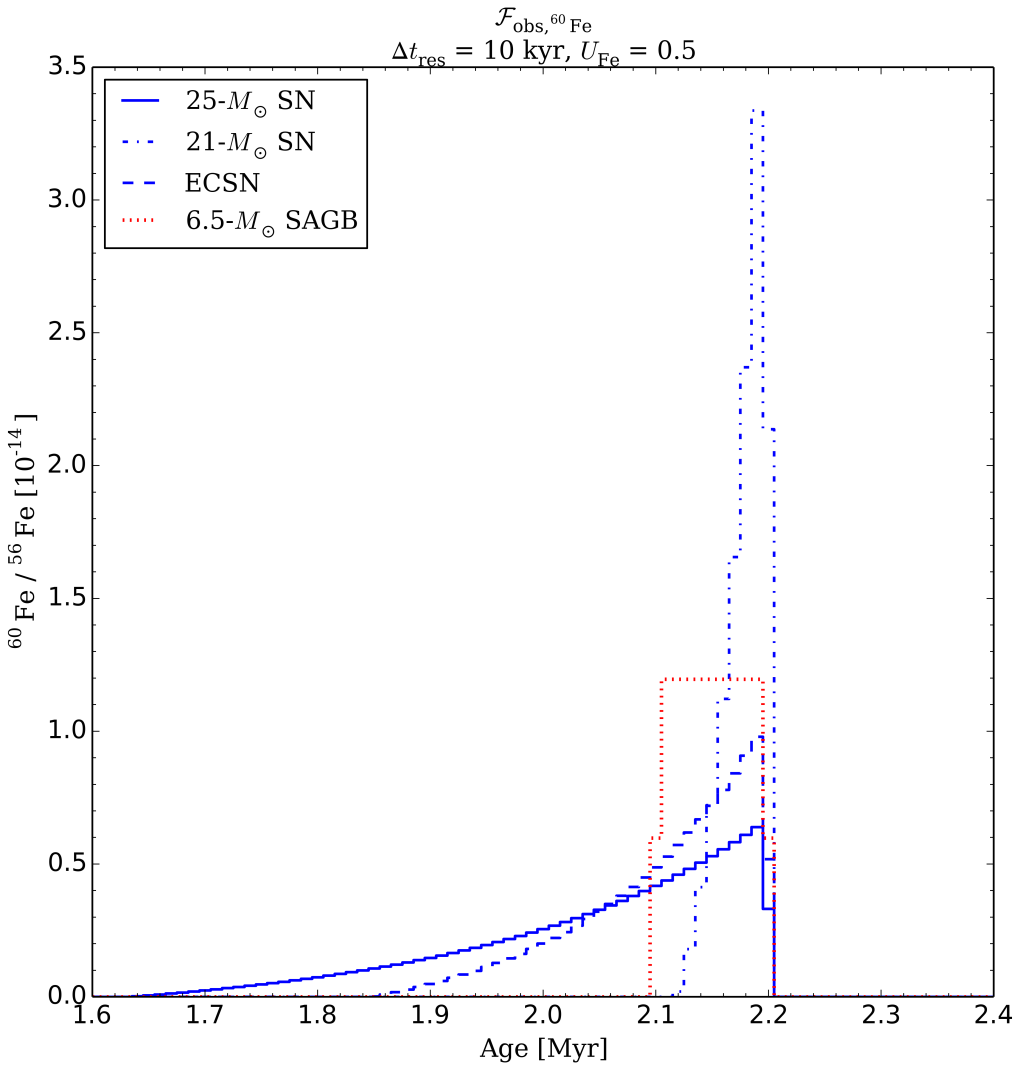

Figure 2.1: *Sample time-resolved calculations of the observed fluence, $\mathcal{F}_{\mathrm{obs},^{60}\mathrm{Fe}}$, for three SNe and a SAGB. Each progenitor is at a different distance: 25-$M_\odot$ SN at 130 pc, 21-$M_\odot$ SN at 59 pc, ECSN at 67 pc, and 6.5-$M_\odot$ SAGB at 79 pc. Of note, each of these progenitors would produce the same measured ^{60}Fe signal by Knie et al. (2004); Fitoussi et al. (2008), but with a finer time-resolution (10 kyr in this case), the shape of the signal is readily discernible. Also note that since the plots produce the same observed fluence, the areas under the curves are the same.*

ocean sediments, on the other hand, do not make such a geochemical selection, and have greater accumulation rates $\sim 3-4$ mm kyr^{-1} (Feige et al., 2012). The Fe uptake factor was calculated by Knie et al. (2004) using the relative concentrations of Fe and Mn in water and the Fe-Mn crust and the uptake of Mn (4%), leading to an estimate for the Fe uptake, $U_{\rm Fe} = 0.6\%$. However, recent studies have suggested that $U_{\rm Fe} = 0.5 - 1$ (Bishop & Egli, 2011; Feige et al., 2012). Using the smaller estimate of $U_{\rm Fe}$, Knie et al. (2004) calculated a SN distance of $D \approx 40$ pc; a reasonable distance considering the Local Bubble is ~ 200 pc in diameter in the Galactic plane extending 600 pc perpendicular to the plane (Fuchs et al., 2006) and superbubbles in the Large Magellanic Cloud (LMC) are typically $\sim 100 - 200$ pc in diameter (for a single round of star formation, Chu, 2008). Changing the uptake factor has the immediate effect of changing the implied distance to the explosion. This can be roughly understood if we ignore the effect of the debris decays in transit, in which case the signal follows the inverse square law and we have $D \propto \sqrt{U_i / \mathcal{F}_{{\rm obs},i}}$. The effect of decays en route softens this dependence somewhat.

If $U_{\rm Fe}$ is an order of magnitude larger, the implied distance increases by a factor $\gtrsim 2$. With a Fe-Mn crust uptake factor of $U_{\rm Fe} = 0.5 - 1$, the implied distances are around $D \sim 200$ pc. This seems an unlikely distance, given that the Solar System is roughly in the center of the Local Bubble (see Berghöfer & Breitschwerdt, 2002, Figure 2), and a SN would have had to occur outside the Local Bubble in order to produce the signal (assuming the progenitor is in the Galactic plane).

However, implicit in the Knie et al. (2004) calculation is the assumption that the dust fraction, $f_{\rm Fe} = 1$. As we will show in §2.4.2, this is most likely not the case, and the combination of a higher uptake value (we chose $U_{\rm Fe} = U_{\rm Al} = 0.5$) with a smaller dust fraction ($f_i \ll 1$) can still yield reasonable progenitor distances.

2.4.2 Dust Condensation

It was shown in Fields et al. (2008), that for a SN further than $D \sim 10$ pc, the solar wind would keep the SN blast plasma outside of 1 AU, and thus the Earth will not find itself inside gas-phase SN debris. However, refractory SN ejecta will be condensed into dust grains. As discussed in Athanassiadou & Fields (2011), we expect these grains to be entrained in the SN blast as it reaches the heliosphere, but then decouple at the SN-solar wind shock and move essentially ballistically through the inner solar system. Once the dust decouples from the gas in the shock, it can travel great distances. At this point, both SNe and SAGBs behave the same, as they are subject to the same drag stopping distance, $R_{\rm drag}$ discussed in §2.3.2. This is more than sufficient to reach the Earth in spite of the solar wind, and indeed should carry dust grains beyond the SN remnant when it finally comes to rest. Thus, for the $D > 10$ pc events of interest, the amount of any radioisotope i that comes to Earth will be proportional to the fraction, f_i, of the isotope that reaches Earth via dust, as seen in Equations (2.1) and (2.14).

Determining f_i requires examining a number of factors (the results are summarized in Table 2.2):

1) How much of the isotope condenses into dust at departure from source?

2) How much of that dust survives the interstellar journey from the source to the Solar System?

3) How much of the remaining dust can filter through the heliopause and enter the Solar System?

4) How much of the filtered dust can overcome the solar wind/radiation pressure and reach the Earth's orbit?

In order to determine the isotope fraction that condenses into dust, we use recent observations of SN 1987A. *Herschel* observations in the far infrared and submillimeter wavelengths were modeled in Matsuura et al. (2011) with different elemental abundances and dust compositions. In both models studied, the synthesized Fe mass was nearly identical to the Fe condensed into dust. This suggests that after less than 30 yrs (much less time than required to travel to a nearby solar system), practically all of the iron from the SN is in the form of dust. Furthermore, when comparing condensation temperatures (Spitzer & Jenkins, 1975), one finds that $T_{C,\mathrm{Al}} = 1800$ K $> T_{C,\mathrm{Fe}} = 1500$ K, suggesting Al would condense into dust at the same time as Fe, if not sooner. Based on this reasoning, we assume 100% of Al and Fe condenses into dust for both SNe and SAGBs.

While refractory elements seem to condense rapidly after ejection, only the dust that survives transport to the Solar System will reach the Earth. Dust leaving from SAGBs will be subject to shocks from neighboring star systems as well as sputtering from radiation and collisions with other dust grains. However, for the purposes of this paper, we will assume these affects are negligible compared to other filtering effects examined. Therefore, we will assume all of the dust from SAGBs are able to pass from the SAGB to the Solar System (a more in-depth discussion of interstellar effects on dust grains is discussed in Murray et al., 2004).

Conversely, SN remnants are likely to be much harsher environments for dust, leading to predictions of very small survival probabilities for some dust species and thus for some radioisotopes. Dust formed from ejecta in a newborn SN remnant will encounter a reverse shock as the remnant transitions from the free expansion to the Sedov/adiabatic phase. The reverse shock propagates from the outer edge of the remnant back to the source and is generally stronger than the interface between the outer edge of the remnant and general ISM. The reverse shock causes large-scale sputtering/destruction of grains resulting in gas phase emission from previously refractory

elements (e.g., see emission from Cassiopeia A, Rho et al., 2008). Silvia et al. (2010, 2012) studied this interaction and found grains $\lesssim 0.1$ μm to be most affected; $\sim 1\%$ of Al_2O_3 (corundum), $\sim$ 50% of FeS (troilite), and $\sim$ 100% of Fe (metallic iron) previously condensed into dust survives.

Once the dust reaches the Solar System, it must pass through the heliosphere to reach the Earth. Linde & Gombosi (2000) suggested a cut-off grain size of $0.1-0.2$ μm for filtering by the heliosphere for grains with speeds of 26 km s^{-1} corresponding to the Sun's motion through the local ISM. This filtering is less severe for faster dust grains (Athanassiadou & Fields, 2011), but for our larger SN distances we find slower speeds in Table 2.3. Since magnetohydrodynamic simulations by Slavin et al. (2010) showed penetration but strong deflection of 0.1 μm grains, we chose a minimum grain size of 0.2 μm for entering the Solar System. For SN dust, this cut-off means that negligible amounts of Al_2O_3 and FeS grains will enter the Solar System, while $\sim$ 10% of Fe grains will be large enough to pass through. For SAGB dust, we assume the Fe is in elemental Fe and silicate grains (distributed according to Pollack et al. (1994) with FeS assumed to be Fe); Al will be in Al_2O_3, but with a larger grain size (Hoppe & Zinner, 2000). The Fe size distribution is assumed to be the same as for SN (Sterken et al., 2013), and silicate grains are assumed to follow the Mathis et al. (1977) distribution ($dN/da \propto a^{-3.5}$) ranging from 0.5-350 nm (Weingartner & Draine, 2001). This means $\sim$ 10% of Fe, $\sim$ 25% of silicates, and $\sim$ 100% of Al from SAGBs will enter the Solar System.

Lastly, the dust grain must overcome the Sun's radiation pressure once it is in the Solar System. For this, we consider the parameter β (Burns et al., 1979) that characterizes the ratio of the Sun's radiation force, F_r, to the gravitational force, F_g:

$$\beta \equiv \frac{F_r}{F_g} = C_{\rm r} Q_{\rm pr} \frac{3}{4 a \rho_{\rm grain}} \tag{2.17}$$

where C_r is 7.6×10^{-5} g cm^{-2} and Q_{pr} is the efficiency of the radiation on the grain (we will assume $Q_{pr} \sim 1$ for the size of grains we are interested in, Gustafson, 1994). From Sterken et al. (2013), only dust grains with $\beta \lesssim 1.3$ will reach Earth's orbit; based on the densities of the minerals considered, if the grain can enter the Solar System, it will be able to reach Earth's orbit.

Combining each of these factors, we find for SNe: $f_{\mathrm{Fe,SN}} \approx 0.01$ and $f_{\mathrm{Al,SN}}$ is negligible. For SAGBs: $f_{\mathrm{Fe,SAGB}} \approx 0.2$ and $f_{\mathrm{Al,SAGB}} \approx 1$. In spite of the number of considerations in determining these quantities, there are still others that could be included, namely a velocity dependence on the filtering by the heliopause. We would expect dust grains with a sufficiently high velocity (i.e., $v_{\mathrm{grain}} > v_{\mathrm{esc},\odot}$) to ignore size filtering limitations, but including these effects will be left for a future work.

2.5 Live Radioisotope Data

2.5.1 Terrestrial Measurements of ^{60}Fe

The primary data value for our analysis is the decay-corrected ^{60}Fe fluence measured by Knie et al. (2004) in a deep-ocean Fe-Mn crust. They found an isotopic ratio of $^{60}\mathrm{Fe/Fe} = 1.9 \times 10^{-15}$ within the crust; this corresponds to a decay-corrected fluence of $\mathcal{F}_{\mathrm{arr},60} = (2.9 \pm 1.0) \times 10^6$ atoms cm^{-2}. This may be used to determine the distance from the progenitor. At the time of the original measurements, the half-life of ^{60}Fe was estimated to be 1.49 Myr and that of ^{10}Be was estimated to be 1.51 Myr, resulting in an arrival time, $t_{\mathrm{arr}} = 2.8$ Myr ago. Since then, the half-lives have been refined: current best estimates being $\tau_{1/2,\,^{60}\mathrm{Fe}} = 2.62$ Myr and $\tau_{1/2,\,^{10}\mathrm{Be}} = 1.387$ Myr, and this places the signal arrival at 2.2 Myr ago. To update the Knie ^{60}Fe fluence, we use ratios to convert the previous results to the updated values that are similar in method to those employed by Bishop & Egli (2011) and Feige et al. (2012): $\mathcal{F}_{60,\mathrm{update}}/\mathcal{F}_{60,\mathrm{previous}} = e^{-t_{60,\mathrm{update}}/\tau_{60,\mathrm{update}}}/e^{-t_{60,\mathrm{previous}}/\tau_{60,\mathrm{previous}}}$, which gives the

following updated, decay-corrected fluence in the crust:

$$\mathcal{F}_{\mathrm{arr},60(\mathrm{updated})} = (1.41 \pm 0.49) \times 10^6 \text{ atoms cm}^{-2} \tag{2.18}$$

The ^{60}Fe measurement in the crust has been verified by Fitoussi et al. (2008), but within this same work, no comparable ^{60}Fe signal was detected in a sea sediment sample. Fitoussi et al. (2008) suggested several reasons for the non-detection in the sediment, including differences in uptake and divergences in the sediment from the global background. In addition, we note that the fluence calculation assumes an even distribution of dust over the Earth's surface. However, the Earth's wind patterns are not uniform, nor is Earth's precessional axis necessarily orthogonal to the progenitor's position. Consider, for example, a spherical dust grain of radius 0.2 μm falling at terminal velocity (~ 0.1 m s^{-1}) through a 1500 m-thick jet stream flowing horizontally at 100 km hr^{-1} with a density of 4×10^{-4} g cm^{-3} (the assumption of falling at terminal velocity should be valid as the Earth's atmosphere will have dissipated most of the dust grain's remaining interstellar kinetic energy). As the dust grain falls, the pressure from the jet stream will quickly accelerate the grain horizontally to the same velocity and push the grain ~ 300 km before it falls out of the jet stream. In view of the non-uniformity of the jet stream's flow as well as other terrestrial winds, anisotropies in the observed fluences are expected. Furthermore, one should also consider the source's orientation to the Earth's precessional axis; the Fe-Mn crust used by Knie et al. (2004) is from 9°18' N, 146°03' W ($\sim 1,000$ mi/1,600 km SE of Hawaii), and the sediment used by Fitoussi et al. (2008) is from 66°56.5' N, 6°27.0' W (~ 250 mi/400 km NW of Iceland). The crust sample's location relative to the equator would make it more likely to receive a signal over a range of arrival angles while the northern hemisphere could be partially shielded from a more southerly progenitor. Rather than the Fe-Mn crust signal being due to a misinterpretation of the global background, the absence of

a sediment signal could be due to the geometry of the source's position. If this is the case, a sediment sample from the southern hemisphere (e.g., ELT49-53, 38°58.7' S, 103°43.1' E and ELT45-21, 37°51.6' S, 100°01.7' E used by Feige et al. (2013)) should have an ^{60}Fe signal.

2.5.2 Lunar Measurements of ^{60}Fe

In addition to sea sediment and Fe-Mn crusts, lunar surface (regolith) samples can also be used to search for a nearby progenitor signal. The lunar surface is not affected by wind or water erosion, but, as pointed out by Feige et al. (2013), the sedimentation rate is low (precluding the possibility of time-resolved measurements) and regular impacts by a range of impactors (Langevin & Arnold, 1977), continually churn up the regolith, mixing different levels. Lunar samples would be better suited to providing a "first hint" of a signature (Feige et al., 2013). Apollo core samples were analyzed by Cook et al. (2009), Fimiani et al. (2012), and Fimiani et al. (2014); in particular, these authors found both the Apollo 12 sample 12025 and Apollo 15 sample 15008 to have an ^{60}Fe signal above the background. Nishiizumi et al. (1979) and Nishiizumi et al. (1990) found that the Apollo 12 and 15 cores, respectively, showed little to no large-scale mixing just prior to, during, and/or since the potential arrival of the signal, meaning no large impactor could have ejected part of the regolith thus diluting the signal. However, as we show in the next section, another issue arises with the dust's arrival at the Moon's surface that can dilute the signature.

2.5.3 Lunar Regolith and Dust Grains: Vaporization

As noted above, there are putative detections of a non-meteoric ^{60}Fe lunar anomaly, which seem to verify the presence of the deep-ocean signal; an amazing confirmation. However, having argued that the ^{60}Fe will arrive in the form of high-velocity dust

grains, we now consider the implications for the deposition onto the lunar surface.

Cintala (1992) made a detailed study of impacts on the lunar regolith and found semi-empirical fits to the volume of vapor produced as a function of impactor size and velocity and of the target composition. It was found that impactor velocity is the dominant factor and that, for $v_{\rm grain} > 100$ km s^{-1}, the volume of target material that is vaporized is $\sim 10 - 100$ times the volume of the impactor itself. More recently, Cremonese et al. (2013) showed that micrometeor impacts can be a non-negligible source of the lunar vapor atmosphere. They use the Cintala (1992) model and find that the contribution may be 8% of the photo-stimulated desorption at the subsolar point, becoming similar in the dawn and dusk regions and dominant on the night side. Moreover, Collette et al. (2014) did laboratory experiments to simulate micrometeorite impacts, studying the neutral gas created as a result. They find that the number of neutrals produced per unit impactor mass scales as $\sim v_{\rm grain}^{2.4}$, and they conclude that complete vaporization is expected for speeds exceeding 20 km s^{-1}.

With these results in mind, we now consider the conditions surrounding the arrival of the dust signal in question at the lunar surface. After entering the Solar System, the dust grains continue to the Earth/Moon at essentially the same speed. However, whereas the Earth's atmosphere slows the arriving dust grains prior to reaching the surface, the Moon's tenuous atmosphere has practically no influence, and the dust grains' velocities are unchanged before arrival at the lunar surface. The dust grains are estimated to be ~ 0.2 μm in size, and moving at $\sim 20 - 100$ km s^{-1} depending on the progenitor's distance. Thus the grains behave as "micrometeorites" moving at very high speeds similar to those examined above.

Consider a silicate dust grain ($\rho_{\rm grain} \sim 3.5$ g cm^{-3}) impacting the lunar surface ($\rho_{\rm regolith} \sim 1.6$ g cm^{-3}) at $v_{\rm grain} \sim 20$ km s^{-1}. The grain arrives with kinetic energy $E_{\rm grain} = m_{\rm grain} v_{\rm grain}^2/2 \sim 0.23$ erg, where $m = 4\pi\rho_{\rm grain} a^3/3$ is the mass of a spherical grain of radius a. The dust grain will penetrate the regolith to a depth comparable

to its diameter and will vaporize some of the surrounding material; we will assume $V_{\rm vapor} = 10V_{\rm grain} \Rightarrow m_{\rm vapor} \approx 4.6m_{\rm grain}$. Given the grain's high speed and shallow penetration, the vaporization will happen quickly (i.e., very little expansion occurs before the entire mass is vaporized). Moreover, since the initial density of the vaporized regolith is much greater than the density of the Moon's atmosphere, the gas will behave as if it is expanding isentropically into a vacuum. The grain's kinetic energy will go into vaporizing the grain and regolith and into the thermal and kinetic energy of the resulting gas. To determine the vaporization energy, the standard enthalpy of formation for the lunar regolith is $\sim 1.5 \times 10^{11}$ erg/g $= (3.9 \text{ km s}^{-1})^2$. This is an approximate value for both of the lunar regolith's main constituents, silica, SiO_2, and aluminum oxide, Al_2O_3, (Nava & Philpotts, 1973), and includes both the vaporization and dissociation energies for the molecules. Therefore, the total energy consumed in vaporization is 0.1 erg, leaving 0.13 erg for the thermal and kinetic energy, $E_{\rm vapor}$, of the gas.

As the gas expands, the thermal portion vanishes asymptotically, with all the energy becoming kinetic. Thus, after this cooling, the asymptotic expansion speed of the vaporized material is:

$$v_\infty = \sqrt{\frac{2E_{\rm vapor}}{m_{\rm vapor} + m_{\rm grain}}} \approx 6 \text{ km s}^{-1} \tag{2.19}$$

[For further discussion, see Zel'dovich & Raizer (1967, p. 101-104, 844-846)].

The vapor speed is much larger than the lunar escape velocity, $v_{\rm esc,Moon} = 2.4$ km s^{-1}. This suggests that much of the vaporized material, including the dust impactor with its ^{60}Fe material, would escape from the Moon. This would imply that the Moon has an uptake factor $U_{\rm Moon} \ll 1$. Thus, we should not be surprised that the lunar results for ^{60}Fe are lower than expected naively from the terrestrial Fe-Mn crust results. While lunar samples confirm the signal found in the Fe-Mn crust, they are

less suitable for determining the fluence given the difficulties in determining $U_{\rm Moon}$.

2.5.4 ^{244}Pu Measurements

Several searches for live ^{244}Pu have been performed, beginning with Wallner et al. (2000) looking at Fe-Mn nodules. Studies of top layer sea sediment by Paul et al. (2001), Paul et al. (2003), and Paul et al. (2007) have shown there is a very low background in ^{244}Pu, making ^{244}Pu an excellent candidate to confirm an ^{60}Fe signal from an extra-solar source (presumably from a CCSN). Wallner et al. (2000, 2004) reported the detection of a single ^{244}Pu atom in the same Fe-Mn crust sample used by Knie et al. (1999) and Knie et al. (2004) covering the entire time interval of $1 - 14$ Myr. Separately, Raisbeck et al. (2007) looked in sea sediment for a ^{244}Pu signal, but did not find any evidence for a signal. It should be noted, however, that the Raisbeck study was using the previous arrival time (2.8 Myr ago) for his search. The samples were dated using magnetic polarization analysis and did not cover a large enough time interval to include the appropriate dating interval using the new value for the ^{10}Be lifetime (Meynadier et al., 1994).

2.5.5 ^{26}Al Measurements

Feige et al. (2013) reported on searches for ^{10}Be and ^{26}Al using ~ 3 kyr time intervals in samples from sea sediments ELT 49-53 and ELT 45-21. In the case of ^{26}Al, the measurements showed only variations consistent with fluctuations around the background level, and found no evidence for an extra-solar signal. The paper also reported that ^{53}Mn measurements are planned.

2.6 Results

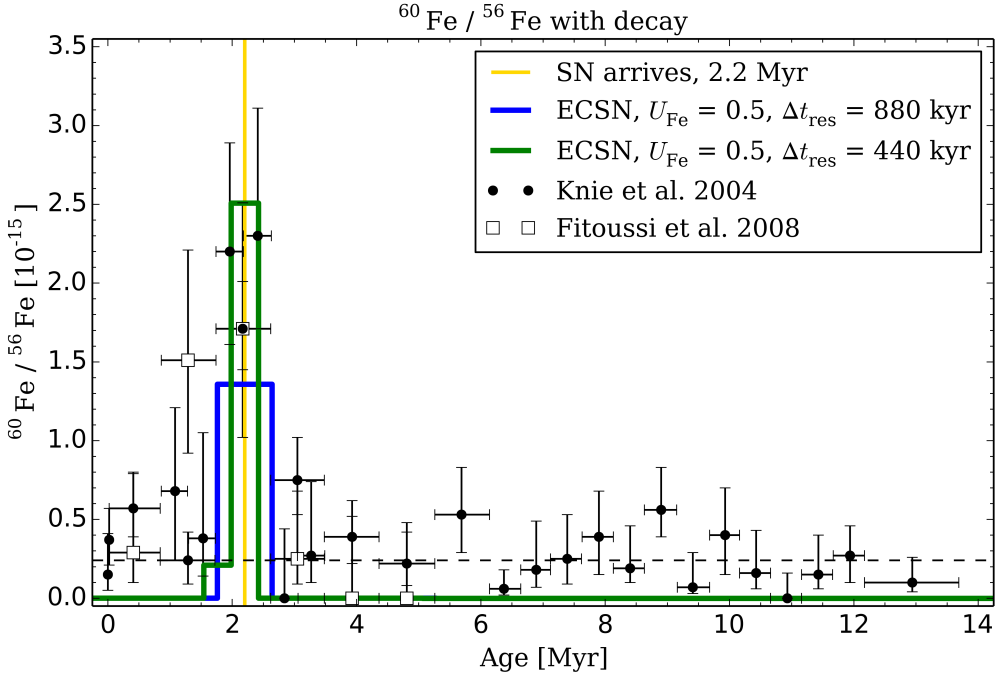

Figure 2.2: *Comparison of Knie et al. (2004) and Fitoussi et al. (2008) data with simulation for a SN explosion with an anomalous peak in the* ^{60}Fe *isotope fraction* ~ 2.2 *Myr ago. We plot the results using ECSN yields; other progenitors yield similar results.*

In Figure 2.2 we compare our model predictions with the ^{60}Fe data of Knie et al. (2004) and Fitoussi et al. (2008), showing that the model matches the results within the uncertainties for a SN or SAGB occurring 2.2 Myr ago. We note that the sampling was continuous through the entire data range, and straddled the signal arrival. In addition, the value for the 880-kyr time resolution was less than the 440-kyr sample, as expected due to the additional stable Fe in the wider sample.

Using the decay-corrected Knie et al. (2004) fluence of ^{60}Fe (§2.5.1), and ^{60}Fe yields from various source candidates (§2.2), we have solved Equation (2.1) for the distance to the source. Distances and other parameters for some of the possible sources appear in Table 2.3 and Figure 2.3. We see that, for sources at distances $\sim$ 100 pc that are typical of our subsequent estimated distances, the en route time and the signal

width are $\mathcal{O}$(Myr), so it is possible that the signal could be time-resolved in future measurements, and thus it is of interest to model the signal shape.

2.6.1 Core-Collapse and Electron-Capture Supernovae

Figure 2.3 shows the calculated distances for our examined CCSNe and ECSN; they range from $\sim 60 - 130$ pc. All CCSNe from our set lie outside of the kill distance and within the fadeaway distance for both their average fluence values and errors. Similarly, the ECSN lies outside the kill distance and within the fadeaway distance (the ECSN kill and fadeaway distances are shorter due to its lower explosive energy). The ECSN upper error is outside the fadeaway distance, but because SN dust can still travel great distances after decoupling, this is not an absolute limitation. Based on these distances, either a CCSN or an ECSN could have produced the measured ^{60}Fe signal.

2.6.2 Thermonuclear Supernovae

TNSN produce so little ^{60}Fe that it would require a TNSN to have been at a distance of ~ 0.6 pc in order to produce the signal measured by Knie et al. (2004). This is an implausibly short distance, and any uncertainty in the fluence measurement would not change this determination. At that range, the TNSN would have killed nearly all life on Earth, so we can exclude a TNSN as the source of the ^{60}Fe signal (in this case, the descreening kill distance for a TNSN is $\sim$10 pc and the ionizing radiation kill distance from 10^{48} erg of γ-rays is $\sim$20 pc, Smith et al., 2004). Adopting the largest yield ($M_{\mathrm{ej},^{60}\mathrm{Fe}} \sim 10^{-7}\ M_{\odot}$) from Seitenzahl et al. (2013) extends the distance to ~ 6 pc, which is still inside the kill radius and does not change this conclusion.

2.6.3 Kilonovae

Our calculations give a possible KN distance of ~ 5 pc. Of the little that is known observationally or even theoretically about KNe, we are unaware of any estimates of their ionizing radiation output. In addition, the strength and shape of the shock from ejected material is highly dependent on the orientation of the merger. Thus, we are unable to estimate the corresponding kill distance either by direct exposure or descreening. The ejecta from KNe are certainly energetic (explosive velocities $\sim 0.3c$, Goriely et al., 2011), and one might imagine decompressing neutron star matter initially emitting in the UV or at shorter wavelengths. However, the observed radiation for the KN candidate associated with GRB 130603B is very red at times $\gtrsim 8$ hours (Berger et al., 2013). Moreover, while the KN shock and radiation is expected to be much more isotropic than the GRB, more study of the geometry of the resulting blast is needed to determine a definitive kill distance like that used for TNSN. Consequently, a biohazard argument cannot rule out a KN explosion as the source of the ^{60}Fe anomaly.

However, a much better discriminator for a KN source would be the ^{244}Pu/^{60}Fe ratio. The single ^{244}Pu atom detected by Wallner et al. (2000, 2004) yields a surface fluence of 3×10^4 atoms cm^{-2} for the period $1-14$ Myr ago. Looking at the yields from Goriely et al. (2011) again, we can infer the yield for $A = 244$ should be at least on the order of the yield for $A = 60$ (i.e., $(^{244}\mathrm{Pu}/^{60}\mathrm{Fe})_{\mathrm{KN}} \geq 1$).[7] Based on this assumption and the surface fluence for ^{60}Fe during the signal passing (1.41×10^6 atoms cm$^{-2}/0.5 = 3\times10^6$ atoms cm^{-2}), then:

$$(^{244}\mathrm{Pu}/^{60}\mathrm{Fe})_{\mathrm{measured}} \approx 10^{-2} \ll 1 \lesssim (^{244}\mathrm{Pu}/^{60}\mathrm{Fe})_{\mathrm{KN\ predicted}}$$

even though ^{244}Pu was measured over 10 times the time period as ^{60}Fe (Note: this

[7] More likely, $A = 244$ yields are 10-100 times larger than $A = 60$ yields given the $A \sim 240$ yields and the fact that the fission recycling sources are centered around $A \simeq 280 - 290$ region, Goriely et al. (2011).

assumes the dust fraction for Pu is the same as Fe, $f_{\rm Pu} \sim f_{\rm Fe}$).

Additionally, KN occur infrequently (~ 10 Myr^{-1} galaxy^{-1}, Goriely et al., 2011) compared to CCSN & ECSN (~ 30 kyr^{-1} galaxy^{-1}).[8] If we approximate the Milky Way as a thin cylinder of radius 10 kpc and thickness 200 pc, the rates (Γ) of a KN occurring within ~ 5 pc or a CCSN/ECSN occurring within ~ 75 pc of the Earth are:

$$\Gamma_{\text{nearby source}} = \Gamma_{\text{galaxy}} \frac{V_{\text{nearby source}}}{V_{\text{galaxy}}}$$

$$\Gamma_{\text{nearby KN}} = \left(\frac{1}{10^7 \text{ Myr}}\right)\left(\frac{D}{5 \text{ pc}}\right)^3$$

$$\Gamma_{\text{nearby SN}} = \left(\frac{1}{1 \text{ Myr}}\right)\left(\frac{D}{75 \text{ pc}}\right)^3$$

After inverting these quantities, we can expect a nearby SN every ~ 1 Myr compared to a nearby KN every $\sim 10^7$ Myr $\gg 1/H_0$ (the Hubble time). This makes a KN an unlikely source for the ^{60}Fe signal. However, this result should be revisited as specific yields for ^{60}Fe become available and especially if a signal from strong r-process isotopes is detected (e.g., ^{146}Sm, ^{182}Hf, and ^{244}Pu).

2.6.4 Super-AGB Stars

Figure 2.3 plots three of our six examined SAGBs (all are listed in Table 2.3). Their distances range $\sim 60 - 110$ pc; similar to those of CCSNe. With errors, all SAGBs lie well within the distance for dust stopping due to drag (~ 90 kpc) but well outside the magnetic deflection distance (~ 1 pc). While it is tempting to rule out SAGBs as a source under the assumption that any dust would be quickly deflected, we have decided to not rule out SAGBs (see, e.g., Frisch, 1995; Cox & Helenius, 2003; Florinski et al., 2004; Frisch et al., 2012) since there is uncertainty in the strength, direction, and uniformity of the Local Bubble's magnetic field. Depending on the nature of

[8] We would like to thank the reviewer for suggesting this addition to the KNe discussion.

the Local Bubble's magnetic field, charged dust particles could travel with very little deflection. Instead, we will be examining an alternate search in a future work.

2.6.5 ^{26}Al Results

In Figure 2.4, we plot ^{26}Al predictions for various progenitors, and the expected background in the Accelerator Mass Spectrometry (AMS) data from Feige et al. (2013) using the same 3-kyr sampling intervals used in this experiment. Because $f_{\mathrm{Al,SN}} \approx 0$, we do not expect any signal to be present if the source were a SN. The calculated signal from a 15-$M_{\odot}$ CCSN with $f_{\mathrm{Al,SN}} = 1$ is plotted simply as an example if the dust fraction was significantly higher. Additionally, while we would expect some Al from SAGBs to reach Earth, it would not be visible above the variations in the ^{26}Al background.

2.6.6 ^{53}Mn Results

In anticipation of AMS ^{53}Mn measurements mentioned by Feige et al. (2013), in Figure 2.5 we plot predictions for ^{53}Mn based on the distance determined by the ^{60}Fe fluence. Since the survival and grain size for Mn from a SN has not been described to our knowledge, we plotted a range of SN progenitors (since SAGBs are not expected to produce ^{53}Mn) and dust fractions, using the largest possible signal source (21-$M_{\odot}$ CCSN), a mid-range source (15-$M_{\odot}$ CCSN), and the lowest source (ECSN). We varied the dust fraction from an order of magnitude above to an order of magnitude below $f_{\mathrm{SN,Fe}}$. As can be seen for the 15- and 21-$M_{\odot}$ CCSN with $f_{\mathrm{SN,Mn}} \gtrsim f_{\mathrm{SN,Fe}}$, a signal should be readily detectable the given the AMS detection threshold of $\sim 10^{-15}$ ^{53}Mn/^{55}Mn (Poutivtsev et al., 2010). However, for the ECSN and most CCSNe with $f_{\mathrm{SN,Mn}} < f_{\mathrm{SN,Fe}}$ (even a 21-$M_{\odot}$ case could be difficult to detect depending on the fluctuations in the ^{53}Mn/^{55}Mn background), it should be improbable for a SN

progenitor to be detected with ^{53}Mn.

2.7 Discussion and Conclusions

Since the discovery and confirmation of the terrestrial ^{60}Fe signal by Knie et al. (1999) and Knie et al. (2004), several experiments have tried to find a corroborating signal either in lunar samples or with other isotopes. To date, none of these experiments provided a definitive signal on the order of that originally reported. This paper attempts to provide a context for these observations and seek other possible progenitors besides a CCSN whose properties could be consistent with the observations. We also anticipate future observations with a hope for time-resolved signals.

From our list of candidates, we can rule out a TNSN as it would be too close (~ 0.6 pc) to both create the ^{60}Fe signal and to not kill most life on Earth. We also rule out a KN as a potential source. The KN would have been ~ 5 pc away from the Earth, and while more study of the geometry of a KN is required to determine a definitive kill distance, the low amount of ^{244}Pu (a strong r-process element) detected to date contrasted with the high number of r-process elements per merger makes a KN a low probability. Additionally, KNe/Neutron Star Mergers are very rare, making it unlikely for the Solar System to have passed within 5 pc of one.

Although SAGB stars are outside the magnetic field deflection distance, we have decided to not rule out SAGB stars based solely on this stipulation. Depending on the strength, direction, and uniformity of the Local Bubble's magnetic field and the charge on the dust grains, it may be possible for a SAGB to have produced the measured ^{60}Fe signal. Since a SAGB would likely have evolved to the white dwarf stage by now, we plan to investigate this possibility in a future work.

All variations of CCSNe and ECSN remain possible sources. Of these, ECSN would be the most likely, firstly, because they arise from the lowest-mass and thus most

common core-collapse progenitors. Additionally, Fuchs et al. (2006) listed members of the Sco-Cen association and their masses (using their listed magnitudes and mass-to-magnitude relation) which included the range: $M_{\rm Sco-Cen} = 2.5 - 8.2\ M_{\odot}$, compared to $M_{\rm ECSN} = 8 - 10\ M_{\odot}$. Since more massive stars evolve faster than lower-mass stars, it is reasonable to expect the signal progenitor to be near the upper end of the mass range. Lastly, the continued lack of a definitive ^{244}Pu signal, in spite of multiple attempts, is also consistent with the possibility of an ECSN as the progenitor due to its lack of strong r-process products.

Several caveats are important to bear in mind. Probably most importantly, our ability to test different explosion candidates is only as good as the radioactive yield predictions. These challenging calculations are continually improving, but are subject to significant uncertainties, including stellar evolution, hydrodynamics, and nuclear physics. Indeed, two key nuclear cross sections alone can lead to ^{60}Fe and ^{26}Al yield variations by factors up to ~ 10 (Tur et al., 2010). This alone suggests that all of the CCSN candidates should be revisited as yields improve. Seitenzahl et al. (2013) showed that TNSN yields are sensitive to the number of initiation sites and the transition from deflagration to detonation. Clearly, improved radioisotope yield calculations for any of our explosive sources could dramatically change the landscape of possible scenarios. Thus, we implore future nucleosynthesis studies to include (at least) ^{60}Fe and the other radioisotopes we have discussed here.

Other important uncertainties similarly invite future work. As we have seen, Fe uptake in Fe-Mn crusts represent another topic that invites future study. Uptake has a dramatic impact on our results: the inferred distance to the explosion scales as $D \propto U_i^{1/2}$. Additionally, the local interstellar density and magnetic field plays a key role in the propagation of the signal (whether from a SN or SAGB) and in the duration of the time profile of the radioisotope flux. Finally, as we have seen, the observability of different radioisotopes is highly sensitive on the formation and survival of supernova

dust of different compositions and sizes. We have relied on theoretical calculations (Silvia et al., 2010, 2012) which imply, among other things, that ^{26}Al is unlikely to be observable terrestrially despite its SN abundance comparable to ^{60}Fe. Further such theoretical studies relevant to other radiosotopes, and observational corroboration, are critically needed.

To confirm the origin of the ^{60}Fe signal and pin down its source will require measurements of ^{60}Fe at other sites, other sources (e.g., magnetosomes in addition to crust and sediment), and other radioisotopes. Lunar regolith measurements provide unique confirmation of the terrestrial ^{60}Fe signal. However, we find absolute measurements will be difficult because high-velocity dust vaporizes on the lunar surface and much of the incident material will then escape the Moon. This said, we eagerly await detailed presentation of lunar measurements hinted at by Fimiani et al. (2014). We are also looking forward to ^{53}Mn measurements as mentioned by Feige et al. (2013) and ^{244}Pu measurements by Piran et al. (2014, see Wallner, et al. 2014, citation therein) that will be helpful in discriminating between the remaining possible progenitors.

Looking ahead to further measurements, the behavior of dust condensation, survival, and filtering will be a key factor in narrowing the remaining pool of possible progenitors. The dust fraction includes several filtering processes that can all affect the resulting distance calculation ($D \propto f_i^{1/2}$). Studies of dust formation have focused on silicates, iron, and corundum, but formation processes with other elements (especially Mn, Ca, Ti, Zr, Tc, and Pu) could be used to differentiate the remaining possibilities given the varying yield ratios between these elements for each progenitor. The search for other isotopes is not simply a matter of choosing those with high lifetimes ($\tau_i \sim \mathcal{O}(\mathrm{Myr})$), but also those with low backgrounds, high condensation temperatures (in order to form dust grains), and large grain sizes ($a \gtrsim 0.2$ μm). Of particular interest would be ^{41}Ca and ^{53}Mn. While perhaps not ideal candidates with regards to background levels, they have long lifetimes and can be condensed at high tempera-

tures ($\gtrsim$ 1100 K) into Perovskite ($CaTiO_3$), Melilite ($Ca_2Al_2SiO_7$, $Ca_2MgSi_2O_7$), and Alabandite (MnS) (see Field, 1975). Other possible isotopes with long lifetimes such as ^{93}Zr, ^{97}Tc, ^{99}Tc, and ^{107}Pd, as well as strong r-process elements such as ^{146}Sm, ^{182}Hf and ^{244}Pu could be used to constrain CCSNe if more details of their dust condensation are determined, but, regardless, any other candidate isotope would need to form grains large enough to survive escape from its progenitor and enter the Solar System. It would be a remarkable coincidence if the only isotope that is capable of carrying an extra-solar signal (i.e., ^{60}Fe) is the first one examined.

With observations of additional isotopes, it is possible not only to identify a specific event or progenitor, but also to: (1) provide a better measure of the distance to the source, (2) directly probe individual radioisotope nucleosynthesis, (3) constrain the nearby SN rate, (4) guide astrophysical searches for the SN remains (i.e., pulsars), and (5) model the explosion light curve and to assess the possible damage to the terrestrial biosphere. Finally, we have seen that the measurement of time-resolved radioisotope profiles provides direct information of the blast passage through the Solar System and an independent measurement of the distance to the progenitor. The authors are optimistic that new data will make such questions tractable in the near future.

2.8 List of Variables

Variable - Description [common value or unit of measure]

a - radius of dust grain [μm]

A - atomic number [dimensionless]

α - signal width parameter [≈ 0.577]

β - ratio of Sun's radiation force to gravitational force on a particle [dimensionless]

c - speed of light [$\sim 3 \times 10^5$ km s^{-1}]

c_s - speed of sound in ISM [km s^{-1}]

$C_{\rm r}$ - constant from combination of solar flux, gravitational constant, among others [7.6×10^{-5} g cm^{-2}]

D - distance from progenitor to Earth [pc]

δ - shell thickness of uniform shell for a SN remnant [dimensionless]

$E_{\rm CCSN}$ - energy deposited into ejecta by a CCSN [$\sim 10^{51}$ erg]

$E_{\rm ECSN}$ - energy deposited into ejecta by an ECSN [$\sim 10^{50}$ erg]

$E_{\rm KN}$ - energy deposited into ejecta by a KN [$\sim 10^{49}$ erg]

$E_{\rm TNSN}$ - energy deposited into ejecta by a TNSN [$\sim 10^{51}$ erg]

$E_{\rm grain}$ - kinetic energy of dust grain [ergs]

$E_{\rm vapor}$ - thermal and kinetic energy in vapor [ergs]

ϵ - shell thickness of saw-tooth shell [dimensionless]

f - dust fraction, fraction of isotope that passes from progenitor to Earth [dimensionless]

$F_{\rm drag}$ - drag force on dust grain [dyne]

$F_{\rm g}$ - force of gravity on dust grain [dyne]

$F_{\rm mag}$ - force of magnetic field on dust grain [dyne]

$F_{\rm r}$ - force from solar radiation pressure on dust grain [dyne]

$\mathcal{F}_{{\rm arr},i}$ - decay-corrected (or arrival) fluence of an isotope [atoms cm^{-2}]

$\mathcal{F}_{{\rm interstellar},i}$ - total fluence of an isotope across spherical signal front [atoms cm^{-2}]

$\mathcal{F}_{{\rm obs},i}$ - observed fluence of an isotope [atoms cm^{-2}]

$\mathcal{F}_{{\rm surface},i}$ - total fluence of an isotope regardless of uptake [atoms cm^{-2}]

$\mathbb{F}$ - material flux, fluence per time [atoms cm^{-2} kyr^{-1}]

$G(x)$ - density profile function [dimensionless]

$G_0(s)$ - collisional drag function [dimensionless]

γ - ratio of specific heats [dimensionless]

Γ - progenitor rate [Myr^{-1}]

H_0 - Hubble Constant [~ 70 km s^{-1} Mpc^{-1}]

i - (as subscript) 'for a given isotope' (e.g., ^{60}Fe, ^{26}Al, etc.)

k - Boltzmann constant [1.38×10^{-16} erg K^{-1}]

m - mass [g]

M - mass of progenitor [$M_{\odot}$]

$M_{\mathrm{ej},i}$ - total mass of an isotope in the ejecta [$M_{\odot}$]

m_u - atomic mass unit [$\sim 1.66 \times 10^{-24}$ g]

n - number density (e.g., of ISM, dust grain, etc.) [cm^{-3}]

N - number of dust grains [dimensionless]

$\mathcal{N}_i$ - number of atoms of an isotope [dimensionless]

P_{SW} - pressure of solar wind [dyne cm^{-2}]

Q_{pr} - efficiency of solar radiation on dust grain [dimensionless]

R_{drag} - distance at which drag effects are significant on a dust grain [pc]

R_{fade} - distance at which a SN shock transitions into a sound wave [pc]

R_{kill} - distance from the Sun a SN progenitor can produce a shock that penetrates to Earth's orbit [pc]

R_{mag} - distance at which magnetic deflection effects are significant on a dust grain [pc]

R_{SAGB} - radius of leading edge of SAGB dust shell [pc]

R_{SN} - radius of leading edge of SN remnant [pc]

ρ - mass density (e.g., of ISM, dust grain, etc.) [g cm^{-3}]

ρ_0 - density in front of shock [g cm^{-3}]

ρ_1 - density behind shock [g cm^{-3}]

s - velocity parameter [dimensionless]

t - elapsed time [Myr]

t_{arr} - time from today in the past that the leading edge of the signal arrived [Myr]

t_{dep} - time from today in the past that the trailing edge of the signal departed [Myr]

t_{travel} - time for isotope to transit from progenitor to Earth [Myr]

T - temperature of ISM [K]

T_C - condensation temperature [K]

$\Delta t_{\rm inter}$ - delay between envelope pulses of SAGB [$\sim$ 100 yr]

$\Delta t_{\rm pulse}$ - duration of envelope pulse of SAGB [$\sim$ 1 yr]

$\Delta t_{\rm res}$ - time resolution of samples [kyr]

$\Delta t_{\rm SAGB}$ - duration of SAGB phase [$\sim$ 100 kyr]

$\Delta t_{\rm signal}$ - signal width, time for signal to pass Earth and duration of ejecta deposition on Earth [kyr]

τ_i - mean lifetime of an isotope, $\tau_i = \tau_{1/2,i}/\ln 2$ [Myr]

$\tau_{1/2,i}$ - half-life of an isotope [Myr]

U_i - uptake, fraction of deposited isotope that is incorporated into sampled material [dimensionless]

v - speed [km s^{-1}]

$v_{\rm arr}$ - velocity of a dust grain upon arrival at Earth [km s^{-1}]

$v_{\rm esc}$ - escape velocity [km s^{-1}]

$v_{\rm grain}$ - speed of dust grain/impactor [km s^{-1}]

$v_{\rm grain,0}$ - initial speed of dust grain [km s^{-1}]

v_∞ - speed at infinity [km s^{-1}]

$v_{\rm SN}$ - speed of leading edge of the SN remnant [km s^{-1}]

V - volume [cm^3]

$\mathcal{V}$ - voltage of dust grain [V]

X - mass fraction [dimensionless]

ξ_0 - SN proportionality constant [dimensionless] (Zel'dovich & Raizer, 1967)

$$\xi_0 = \left[\frac{75}{16\pi}\frac{(\gamma-1)(\gamma+1)^2}{(3\gamma-1)}\right]^{1/5} \overset{\gamma=5/3}{\approx} 1.1$$

ζ_0 - SAGB proportionality constant [dimensionless]

$$\zeta_0 = \frac{\sqrt{2\pi\gamma}}{4} \overset{\gamma=5/3}{\approx} 0.81$$

2.9 Blast Expansion and Radioisotope Flux Profile

We model astrophysical explosions as spherically symmetric, and we are interested in distances sufficiently large that the swept up interstellar mass is much larger than the ejecta mass. We treat a blast wave as adiabatic (energy-conserving) and thus adopt the Sedov-Taylor solution. The Sedov blast wave evolves in a self-similar manner. This means in particular that gas properties as a function of radius r maintain the same shape when plotted in terms of the similarity variable:

$$x = \frac{r}{R_{\rm SN}(t)}$$

where the shock radius at t is given by Equation (2.2). In particular, the density profile is:

$$\rho(r,t) = \rho_1 \; G(r/R_{\rm SN})$$

where the density immediately behind the shock is:

$$\rho_1 = \frac{\gamma+1}{\gamma-1}\rho_0$$

and the dimensionless density profile function is thus normalized to $G(1) = 1$. Note that mass conservation implies that the total mass $M_{swept} = 4\pi\rho_0 R_{\rm SN}^3/3$ swept up in

the blast is equal to the total mass in the blast profile:

$$M_{total} = 4\pi \int_0^{R_{\rm SN}} r^2 \ \rho(r,t) \ dr = 4\pi\rho_1 R_{\rm SN}^3 \int_0^1 x^2 \ G(x) \ dx$$

and so setting $M_{total} = M_{swept}$ implies that:

$$\int_0^1 x^2 \ G(x) \ dx = \frac{\rho_0}{3\rho_1} = \frac{1}{3}\frac{\gamma-1}{\gamma+1} \stackrel{\gamma=5/3}{\longrightarrow} \frac{1}{12} \tag{2.20}$$

We consider two approximations to the full Sedov profile. For a uniform shell approximation, we have $G(x) = 1$ for $x \in [1-\delta, 1]$ and zero otherwise, which gives the location of the inner shell radius via:

$$\frac{1-(1-\delta)^3}{3} = \frac{1}{3}\frac{\gamma-1}{\gamma+1}$$

and thus:

$$\delta = 1 - \left(\frac{2}{\gamma+1}\right)^{1/3} \stackrel{\gamma=5/3}{\longrightarrow} 0.0914$$

whereas going to first order in δ we would find $\delta = 1/12$. For a "saw-tooth" approximation, the blast material is in a thin shell with a profile that linearly decreases from a maximum behind the shock to zero at coordinate $x_0 \equiv 1-\epsilon$. Thus we have $G(x) = Ax + B$, with the constraints that $G(1) = 1$ and $G(x_0) = 0$ at the inner radius, which gives:

$$G(x) = \frac{x - x_0}{1 - x_0} \tag{2.21}$$

Choosing $\gamma = 5/3$, to first order we find $\int_0^1 x^2 G(x) \ dx = \int_{1-\epsilon}^1 x^2 G(x) \ dx \approx \epsilon/2$. From Equation (2.20) we find the dimensionless shell thickness $\epsilon \approx 1/6$, twice the value in the uniform shell. As seen in Figure 2.6, the saw-tooth density profile more closely matches the exact Sedov density profile compared to the uniform shell profile, making the saw-tooth profile more appropriate for modeling the signal spreading for our SN

distances.

The (radial) velocity profile is:

$$v(r,t) = \dot{R}_{\rm s}\ U\left(\frac{r}{R_{\rm SN}}\right)$$

with $\dot{R}_{\rm s}$ the shock speed, and the dimensionless velocity profile function normalized to $U(1) = 1$. To a good approximation, the velocity is linear, and we will adopt the approximation $U(x) \approx x$. This leads to a "Hubble law" relation:

$$v(r,t) \approx \dot{R}_{\rm s}\ \frac{r}{R_{\rm SN}}$$

Figure 2.6 compares this linear velocity profile with the exact Sedov solution. Our approximation is necessary to maintain the self-similarity of the saw-tooth profile, and, while different than the exact solution, should be sufficient for the region we are most interested in ($0.8 \leq r/R \leq 1$). For a more detailed description of the analytical Sedov solution, see Book (1994).

Turning to the explosive ejecta, we note that if a number $\mathcal{N}_i$ of atoms of species i were distributed with *uniform* density at time t, then the mean number density in i would be:

$$n_{i,0} = \frac{3}{4\pi}\frac{\mathcal{N}_i}{R_{\rm SN}^3}$$

We will assume that, at times of interest, the ejecta is well-mixed into the blast wave, with a constant mass fraction at all radii. That is, we assume that the ejecta density profile follows that of the blast itself. This means that the highest ejecta density is just behind the shock, with a value:

$$n_{i,1} = n_i(R_{\rm SN}) = \frac{\gamma+1}{\gamma-1} n_{i,0}$$

and the ejecta density profile is:

$$n_i(r,t) = n_{i,1} G(r/R_{\rm SN})$$

Combining the ejecta density profile with the "Hubble law" velocity approximation gives the global-averaged ejecta flux onto the surface of the Earth (i.e., 1/4 the interstellar flux, not including radioactive decay), evaluated at distance $r = D$:

$$\mathbb{F}_i(D,t) = \frac{1}{4} n_i(D,t)\ v(D,t) = \mathcal{F}_1 \left(\frac{D}{R_{\rm SN}}\right)^3 G(D/R_{\rm SN})\ \frac{\dot{R}_{\rm s}}{R_{\rm SN}} \tag{2.22}$$

with the time-independent prefactor:

$$\mathcal{F}_1 = \frac{3}{16\pi} \frac{\gamma+1}{\gamma-1} \frac{M_{{\rm ej},i}/m_i}{D^2} \tag{2.23}$$

We see here explicitly that a time-resolved flux directly encodes the blast density profile and thus probes the propagation of the radioisotope ejecta from explosion to Earth.

Using our saw-tooth approximation for the blast density profile G (Equation 2.21), and using the Sedov result $\dot{R}_{\rm s}/R_{\rm SN} = 2/5t$, we find a flux profile in time of:

$$\mathbb{F}_i(D,t) = \frac{2\mathcal{F}_1}{5t} \left(\frac{D}{R_{\rm SN}}\right)^3 \frac{D/R_{\rm SN}(t) - 1 + \epsilon}{\epsilon} \tag{2.24}$$

We note that the leading edge of the blast from an event at distance D arrives at a time t_i given by $D = R_{\rm SN}(t_{\rm arr})$. Thus we can recast $D/R_{\rm SN}(t) = (t/t_{\rm arr})^{-2/5}$ in terms of the initial arrival time. The trailing edge of the shell arrives at time $t_{\rm dep}$ given by $D = (1-\epsilon) R_{\rm SN}(t_{\rm dep})$. Thus we have $t_{\rm dep} = t_{\rm arr}/(1-\epsilon)^{5/2}$. This means that we can write $\epsilon = 1 - (t_{\rm arr}/t_{\rm dep})^{2/5}$, and we can express the global-averaged flux time profile

as:

$$\mathbb{F}_i(D,t) = \left(\frac{t}{t_{\rm arr}}\right)^{-11/5} \left[\frac{(t/t_{\rm arr})^{-2/5} - (t_{\rm dep}/t_{\rm arr})^{-2/5}}{1-(t_{\rm dep}/t_{\rm arr})^{-2/5}}\right] \mathbb{F}_i(D,t_{\rm arr}) \tag{2.25}$$

This is the sum of two power laws in t, leading to a steep cusp at early times $t \to t_{\rm arr}$ that flattens at late times $t \to t_{\rm dep}$.

Table 2.1: Ejected Masses for Various Radioactive Isotopes, in $M_\odot$

Source	15-$M_\odot$ CCSN[a]	19-$M_\odot$ CCSN[a]	20-$M_\odot$ CCSN[a]	21-$M_\odot$ CCSN[a]	25-$M_\odot$ CCSN[a]	8-10-$M_\odot$ ECSN[b]
^{26}Al	2.6×10^{-5}	3.2×10^{-5}	3.0×10^{-5}	4.6×10^{-5}	7.0×10^{-5}	4.4×10^{-8}
^{53}Mn	1.8×10^{-4}	2.1×10^{-4}	1.3×10^{-4}	2.3×10^{-4}	3.6×10^{-4}	1.1×10^{-6}
^{60}Fe	6.6×10^{-5}	1.1×10^{-4}	3.6×10^{-5}	2.5×10^{-5}	1.5×10^{-4}	3.6×10^{-5}
^{41}Ca	4.3×10^{-6}	2.7×10^{-5}	4.3×10^{-4}	6.9×10^{-6}	3.2×10^{-5}	2.0×10^{-7}
^{93}Zr	1.3×10^{-8}	4.7×10^{-8}	9.8×10^{-9}	5.9×10^{-8}	1.5×10^{-7}	N/A[d]
^{97}Tc	4.8×10^{-11}	4.2×10^{-11}	1.9×10^{-10}	1.3×10^{-10}	8.3×10^{-11}	N/A[d]
^{107}Pd	4.1×10^{-10}	8.4×10^{-10}	4.6×10^{-10}	1.4×10^{-9}	1.4×10^{-9}	N/A[d]
^{146}Sm	3.9×10^{-10}	6.3×10^{-12}	3.4×10^{-10}	8.5×10^{-10}	1.2×10^{-9}	N/A[d]
^{182}Hf	1.4×10^{-10}	1.5×10^{-9}	2.5×10^{-10}	5.5×10^{-10}	4.3×10^{-10}	N/A[d]
^{244}Pu[c]	2.0×10^{-11}	2.2×10^{-10}	3.7×10^{-11}	8.1×10^{-11}	6.3×10^{-11}	N/A[d]

Source	6.5-$M_\odot$ SAGB[e]	7.0-$M_\odot$ SAGB[e]	7.5-$M_\odot$ SAGB[e]	8.0-$M_\odot$ SAGB[e]	8.5-$M_\odot$ SAGB[e]	9.0-$M_\odot$ SAGB[e]
^{26}Al	5.0×10^{-6}	5.0×10^{-6}	5.0×10^{-6}	8.0×10^{-6}	1.0×10^{-5}	1.1×10^{-5}
^{53}Mn	0	0	0	0	0	0
^{60}Fe	5.0×10^{-6}	3.0×10^{-6}	4.0×10^{-6}	9.0×10^{-6}	1.4×10^{-5}	1.4×10^{-5}

Note: In addition to the cited CCSN yields from Rauscher et al. (2002), ^{26}Al *and* ^{60}Fe *yields from Limongi & Chieffi (2006) (11-120* $M_\odot$*) were investigated as well. These did not show any additional features beyond those shown with the Rauscher et al. (2002) yields.*

[a] *- S15, S19, S20, S21, and S25 Models respectively, Rauscher et al. (2002)*

[b] *- "unchanged" configuration, Wanajo et al. (2013)*

[c] *-* ^{244}Pu *yields calculated as outlined in Fields et al. (2005) but using Rauscher et al. (2002)* ^{182}Hf *yields*

[d] *- r-process yields for ECSN are not available at present although Wanajo et al. (2013) stated that ECSN may produce some weak r-process elements*

[e] *- Doherty et al. (2013)*

Table 2.2: Summary of Relevant Dust Filtering Processes

Resulting Dust Fraction	Repository Material	Density	Elemental fraction in material	Fraction condensed into dust	Fraction surviving interstellar passage	Fraction passing into helio-sphere	Fraction reaching Earth's orbit
$f_{\mathrm{Fe,SN}} \approx 0.01$	Fe	7.9	0.1^{a}	1^{c}	1^{a}	$0.1^{a,d}$	1^{g}
	FeS	4.8	0.9^{a}	1^{c}	0.5^{a}	$0^{a,d}$	1^{g}
$f_{\mathrm{Fe,SAGB}} \approx 0.2$	Fe	7.9	0.48^{b}	1^{c}	1	$0.1^{a,d}$	1^{g}
	$[\mathrm{Fe, Mg}]_2\mathrm{SiO}_4$	3.5	0.43^{b}	1^{c}	1	$0.25^{d,e}$	1^{g}
	$[\mathrm{Fe, Mg}]\mathrm{SiO}_3$	3.5	0.09^{b}	1^{c}	1	$0.25^{d,e}$	1^{g}
$f_{\mathrm{Al,SN}} \approx 0$	$\mathrm{Al}_2\mathrm{O}_3$	4	1^{a}	1^{c}	0.01^{a}	$0^{a,d}$	1^{g}
$f_{\mathrm{Al,SAGB}} \approx 1$	$\mathrm{Al}_2\mathrm{O}_3$	4	1^{a}	1^{c}	1	$1^{d,f}$	1^{g}

Density is given in g cm^{-3}.

Mass fractions from each filter process are determined using the relative size number distributions, $N(a)$, given in Silvia et al. (2010) and Mathis et al. (1977), multiplying by volume, $V(a)$, and density, ρ, and integrating over the relevant radii [a_{max}, a_{min}]. This method is described in Mathis et al. (1977): $m = \int_{a_{min}}^{a_{max}} \rho\ N(a)\ V(a)\ da$.

[a] *- Silvia et al. (2010)*

[b] *- Pollack et al. (1994), Table 1B. Given the temperature of the Local Bubble ($T > 1000$ K), it is assumed all FeS has been converted to Fe.*

[c] *- Matsuura et al. (2011) and Spitzer & Jenkins (1975)*

[d] *- Slavin et al. (2010)*

[e] *- Mathis et al. (1977)*

[f] *- Hoppe & Zinner (2000)*

[g] *- Burns et al. (1979) and Gustafson (1994)*

Table 2.3: Predicted Parameters for Possible ^{60}Fe Signal Sources

Progenitor	Distance to Source, D, pc	Time en route, $t_{\rm travel}$, Myr	Signal width, $\Delta t_{\rm signal}$, kyr	Arrival speed, $v_{\rm arr}$, km s^{-1}
6.5-$M_\odot$ SAGB	79^{+13}_{-8}	2.8	100	25
7.0-$M_\odot$ SAGB	66^{+11}_{-7}	2.3	100	26
7.5-$M_\odot$ SAGB	73^{+12}_{-8}	2.6	100	25
8.0-$M_\odot$ SAGB	97^{+14}_{-9}	3.5	100	24
8.5-$M_\odot$ SAGB	110^{+15}_{-10}	4.2	100	23
9.0-$M_\odot$ SAGB	110^{+15}_{-10}	4.1	100	23
15-$M_\odot$ CCSN	94^{+19}_{-12}	0.44	250	84
19-$M_\odot$ CCSN	120^{+18}_{-13}	0.74	430	61
20-$M_\odot$ CCSN	71^{+15}_{-9}	0.22	130	130
21-$M_\odot$ CCSN	59^{+13}_{-8}	0.14	80	170
25-$M_\odot$ CCSN	130^{+17}_{-13}	0.98	570	52
8-10-$M_\odot$ ECSN	67^{+12}_{-8}	0.61	351	43

Errors are only for variances in the Knie et al. (2004) decay-corrected fluence value and do not include variations in nuclear reaction rates (SNe) or delayed super-wind phase (SAGBs). These parameters are calculated with the Fe uptake factor, $U_{\rm Fe} = 0.5$.

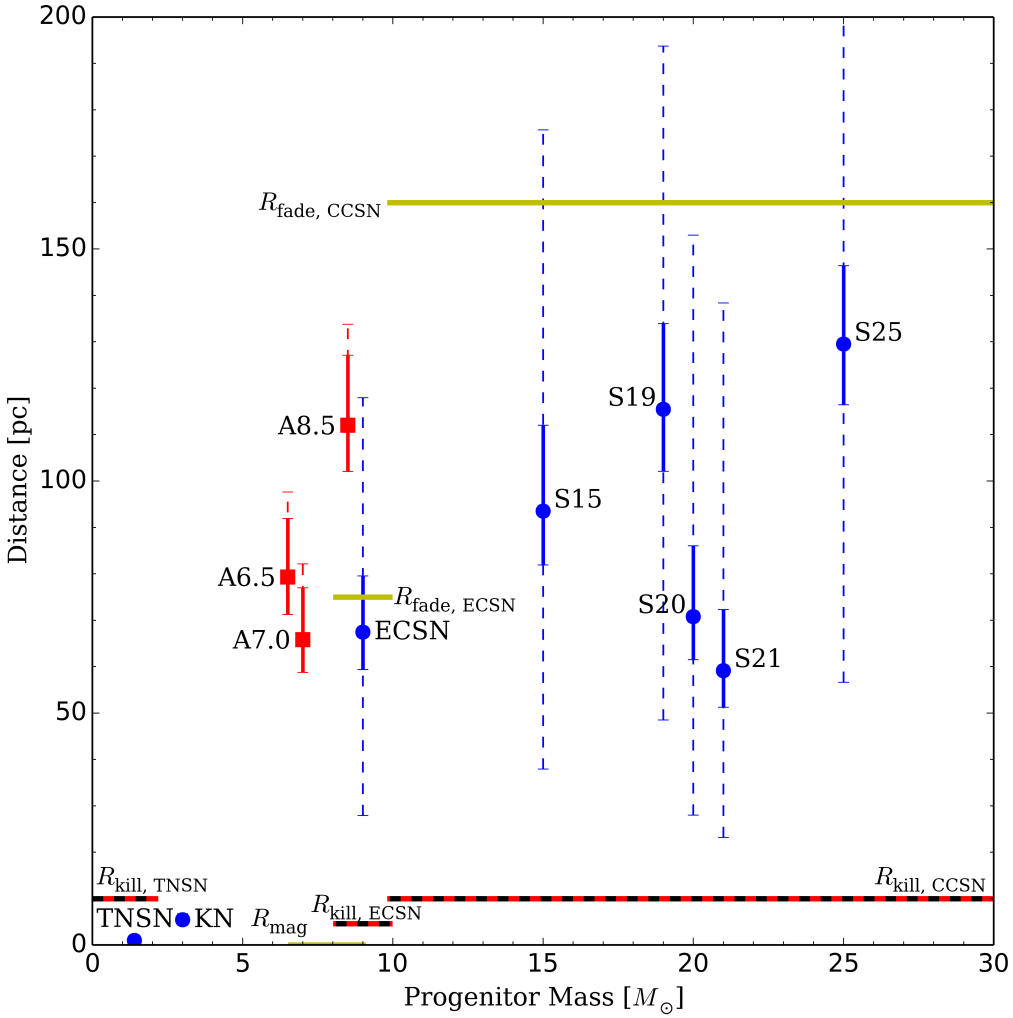

Figure 2.3: *Estimated distances for possible progenitors, for* $U_{\text{Fe}} = 0.5$. *SN candidates are circles and SAGB candidates are squares. The solid error bars represent uncertainty in the fluence measurement (Knie et al., 2004). The dashed error bars represent additional uncertainty in* ^{60}Fe *yields due to nuclear reaction rates in SNe (Tur et al., 2010) and a delayed super-wind phase in SAGBs (Doherty et al., 2013). Of particular note are the TNSN/Type Ia SN and the KN/NS-NS merger models, which are too close to have produced the detected* ^{60}Fe *signal.*

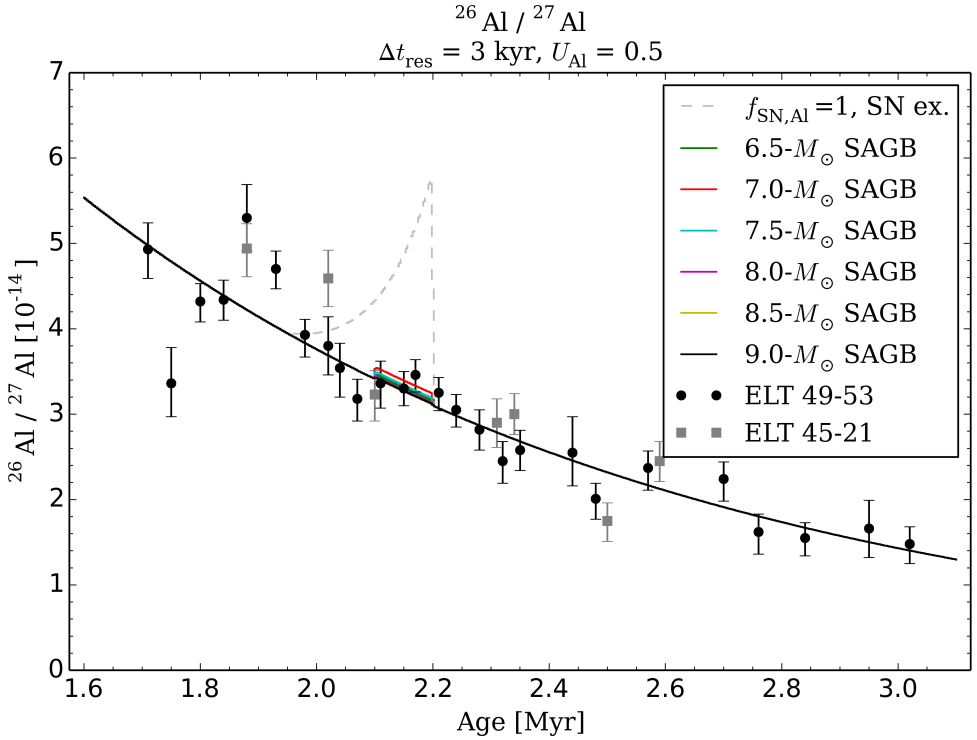

Figure 2.4: *Model predictions compared with the* ^{26}Al *AMS data from Feige et al. (2013). Note that the 15-*$M_\odot$ *SN is an example only and included to demonstrate the consequence if* $f_{\rm SN,Al} = 1$ *instead of the* $f_{\rm SN,Al} \sim 0$ *we expect.*

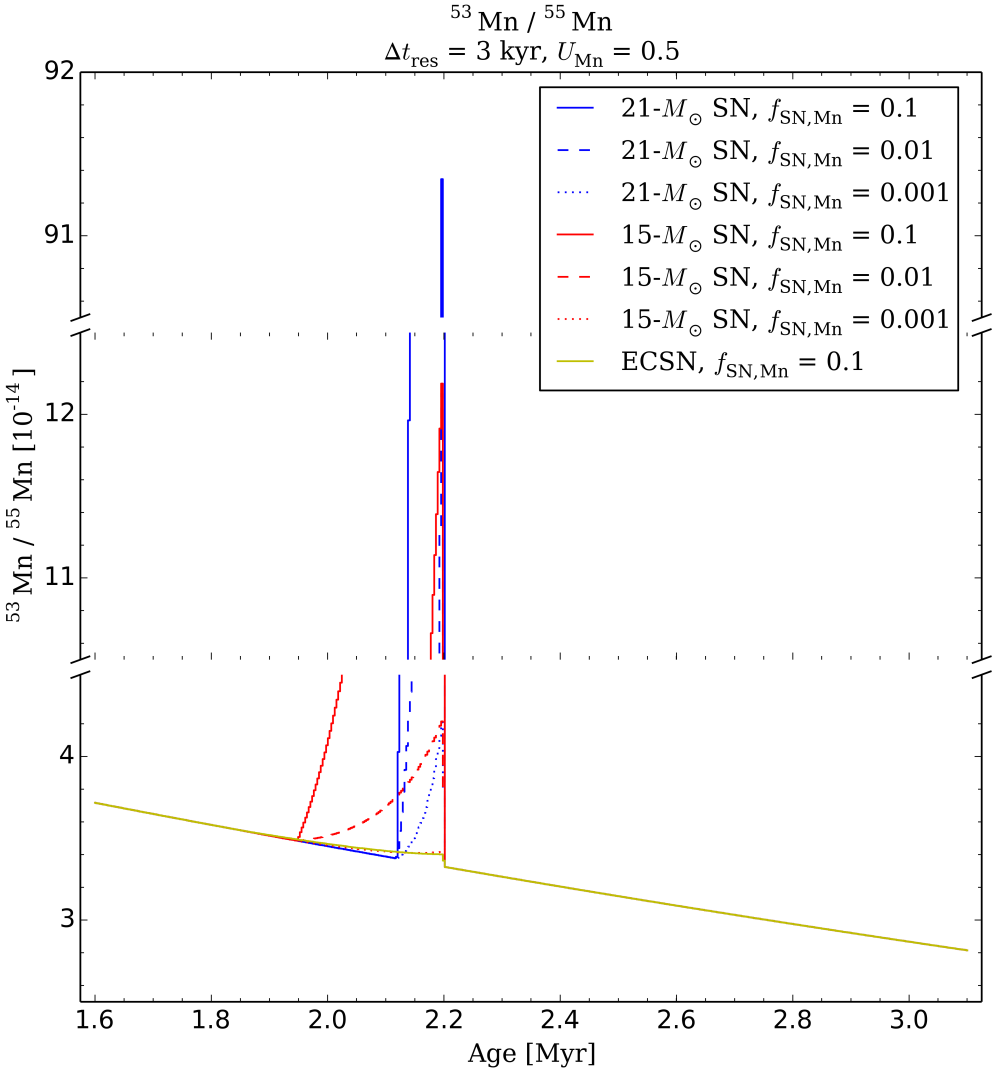

Figure 2.5: *Model predictions for upcoming* ^{53}Mn *AMS measurements. The vertical axis has been broken into three parts in order to show the peak values of each configuration. Note that the average background* ^{53}Mn/^{55}Mn *level (Feige et al., 2013) is shown ahead of the SN's arrival. With an AMS sensitivity of* $\sim 10^{-15}$ ^{53}Mn/^{55}Mn *(Poutivtsev et al., 2010), progenitors such as a 21-*$M_\odot$ *SN should be detectable across a range of* $f_{SN,Mn}$ *values, whereas an ECSN progenitor should not be detectable.*

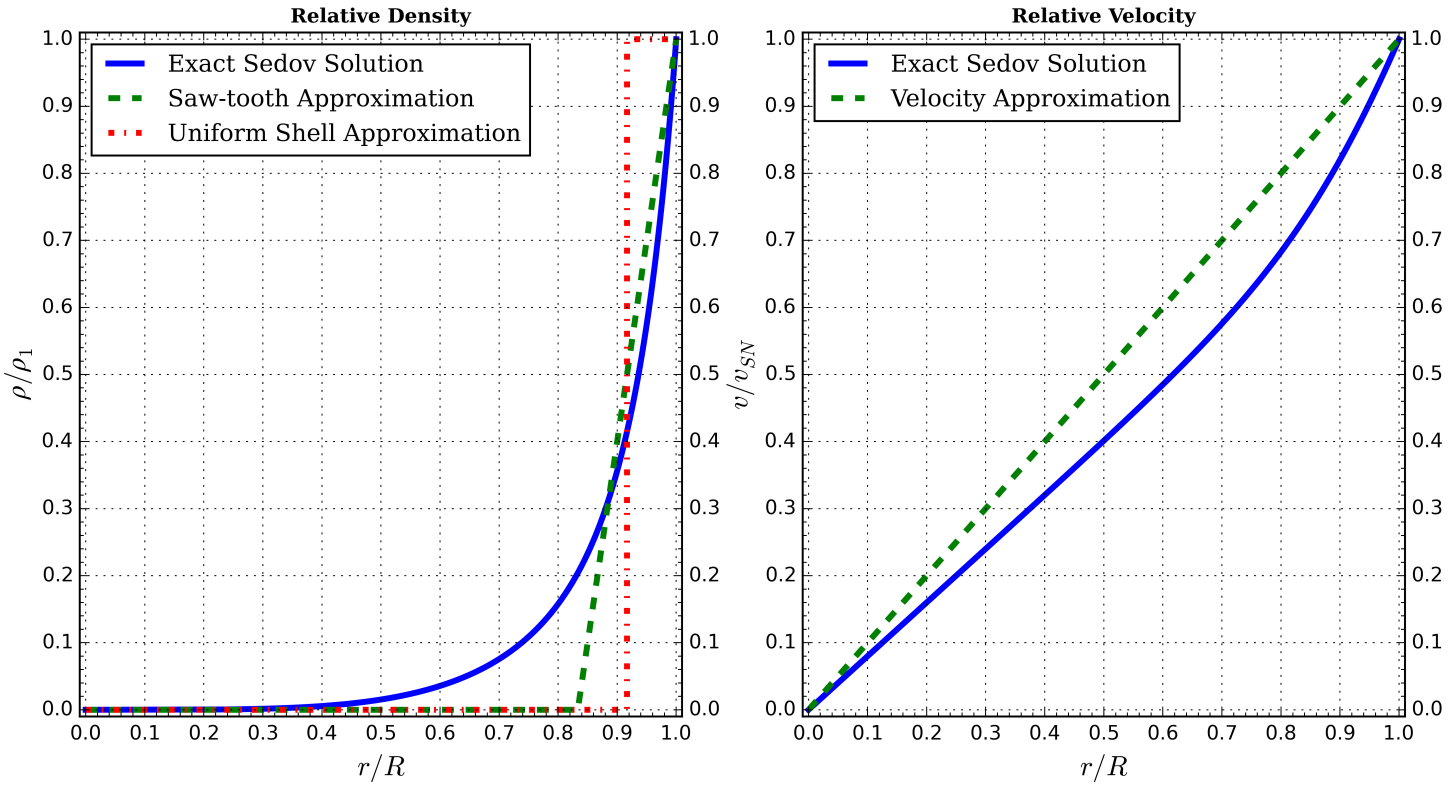

Figure 2.6: *Comparison of the uniform shell and saw-tooth profiles to Sedov-Taylor profile, for* $\gamma = 5/3 \Rightarrow \delta \approx 0.083$ *(uniform shell),* $\epsilon \approx 0.17$ *(saw-tooth). In addition, the paper used a ratio to approximate the observed SN crossing velocity. The right chart compares this approximation to the exact solution profile.*

Chapter 3

Radioactive Iron Rain: Transporting ^{60}Fe in Supernova Dust to the Ocean Floor

This chapter was published in the The Astrophysical Journal under the authorship Fry, B., Fields, B., & Ellis, J.

3.1 Introduction

Supernovae (SNe) are some of the most spectacular explosions in our Galaxy. Occurring at a rate of $\sim 1-3$ per century in the Milky Way (e.g., Adams et al., 2013, and references therein), it is likely that one (if not more) has exploded close enough to have produced detectable effects on the Earth. Speculation on biological effects of a near-Earth SN has a long history in the literature (e.g., Shklovskij, 1969; Alvarez et al., 1980; Ellis & Schramm, 1995), and Ellis et al. (1996) and Korschinek et al. (1996) proposed using radioactive isotopes such as ^{60}Fe and ^{244}Pu to find direct evidence of such an event. Although several studies have searched for ^{244}Pu, this paper will focus exclusively on ^{60}Fe. For more recent examinations of ^{244}Pu, see Wallner et al. (2000, 2004) and Wallner et al. (2015a).

With this motivation, Knie et al. (1999) examined a sample of ferro-manganese (Fe-Mn) crust from Mona Pihoa in the South Pacific and found an anomaly in ^{60}Fe concentration that suggested a SN occurred near Earth sometime within the last 5 Myr (a specific time could not be determined). The study was later expanded in Knie et al. (2004) using a different Fe-Mn crust sample from the equatorial Pacific Ocean floor, and found a distinct signal in ^{60}Fe abundance ~ 2.2 Myr ago, with a ^{60}Fe fluence, $\mathcal{F}$, at the time of arrival calculated to have been $\mathcal{F}_{\rm Knie} = 1.41 \times 10^6$ atoms cm^{-2}. Fitoussi et al. (2008) subsequently confirmed the detection by Knie in the Fe-Mn crust, but did not find a corroborating signal in sea sediment samples from the northern Atlantic Ocean. Fitoussi et al. noted several reasons for the discrepancy, including variations in the background and differences in the uptake efficiencies between the Fe-Mn crust and sediment. An excess of ^{60}Fe has also been found in lunar regolith samples (Cook et al., 2009; Fimiani et al., 2012, 2014, 2016) but, due to the nature of the regolith, only the presence of a signal is detectable, not the precise arrival time or fluence (Feige et al., 2013). Subsequently, results from Eltanin sediment samples from the southern Indian

Ocean were reported in Feige (2014), confirming the Knie et al. (2004) Fe-Mn crust detection in these sea sediment samples and leading to an estimated arrival fluence of $\mathcal{F}_{\rm Feige} = 1.42 \times 10^7$ atoms cm^{-2}. [1] This fluence is an order of magnitude higher than found by Knie et al. (2004), and the difference in fluence values was attributed to differences in uptake efficiencies for sea sediment versus Fe-Mn crust. Feige (2014) and Feige et al. (2013) noted that, whilst the sea sediment uptake efficiency is most likely $U_{\rm sediment} \approx 100\%$, other observations (including the recent, extensive study of ^{60}Fe measurements by Wallner et al., 2016) suggest the Fe-Mn crust has an uptake efficiency of $U_{\rm crust} \in [0.1, 1]$.

Complementing the multiple searches for ^{60}Fe and other isotopes, several papers have discussed the interpretations and implications of the ^{60}Fe signal. The hydrodynamic models used by Fields et al. (2008) discussed the interaction of a SN blast with the solar wind, and highlighted the necessity (see also Athanassiadou & Fields, 2011) of ejecta condensation into dust grains capable of reaching Earth. Fry et al. (2015) examined the possible sources of the Knie ^{60}Fe signal, finding an Electron-Capture SN (ECSN), with Zero-Age Main Sequence (ZAMS) mass $\approx 8 - 10\ M_\odot$ ("$\odot$" refers to the Sun), to be the most likely progenitor, while not completely ruling out a Super Asymptotic Giant Branch (SAGB) star with ZAMS mass $\approx 6.5 - 9\ M_\odot$.

With regards to a possible location of the progenitor, Benítez et al. (2002) suggested that the source event for the ^{60}Fe occurred in the Sco-Cen OB association. This association was ∼130 pc away at the time of the ^{60}Fe-producing event, and its members were described in detail by Fuchs et al. (2006). Breitschwerdt et al. (2012) modeled the formation of the Local Bubble with a moving group of stars (approximating the Sco-Cen association) and plotted their motion in the Milky Way at 5-Myr intervals for the

[1] It should be noted this is the fluence for the period that overlaps the Knie et al. (2004) detection. Feige (2014) found the signal to extend in time beyond the Knie et al. (2004) time interval with a total time-integrated fluence of $\mathcal{F}_{\rm Feige} = (2.32 \pm 0.60) \times 10^7$ atoms cm^{-2}. In addition, Wallner et al. (2016) found a larger total time-integrated value of $\mathcal{F}_{\rm Wallner} = (3.5 \pm 0.2) \times 10^7$ atoms cm^{-2}. For the purposes of this paper we will focus solely on the fluences that overlap with the Knie et al. fluence.

past 20 Myr (see Figure 9 of Breitschwerdt et al., 2012). More recently, Breitschwerdt et al. (2016) have expanded this examination using hydrodynamic simulations to model SNe occurring within the Sco-Cen association and track the ^{60}Fe dust entrained within the blast. Additionally, Kachelrieß et al. (2015) and Savchenko et al. (2015) found a signature in the proton cosmic ray spectrum suggesting an injection of cosmic rays associated with a SN occurring ∼2 Myr ago, and Binns et al. (2016) found ^{60}Fe cosmic rays, suggesting a SN origin within the last $\sim$ 2.6 Myr located $\lesssim$ 1 kpc of Earth, based on the ^{60}Fe lifetime and cosmic ray diffusion. With particular relevance for our discussion, Mamajek (2016) suggested the Tuc-Hor group could have provided an ECSN to produce the ^{60}Fe. The group was within ∼60 pc of Earth ∼2.2 Myr ago and, given the masses of the current group members, could well have hosted a star with a ZAMS mass $\geq 8M_{\odot}$.

Fry et al. (2015) noted that these and other studies assumed a uniform deposition of ^{60}Fe material over Earth's entire surface, and proposed that the direction of arriving material and the Earth's rotation could shield portions of Earth's surface from SN material. Since ^{60}Fe dust from a SN would be arriving along one direction instead of isotropically, the suggestion was that certain portions of Earth's surface would face the SN longer than others and collect more arriving material. This could explain why the northern Fitoussi et al. (2008) sediment samples showed no obvious signal, whereas the southern Feige et al. (2013), Feige (2014) sediment samples showed a stronger signal than the equatorial Knie et al. (2004) crust sample.

This paper re-examines that possibility, and studies how the angle of arrival of dust from a SN effects the deposition on the Earth's surface. We show that the dust propagation in the inner Solar System introduces deflections of order a few degrees. Thus, the angle of arrival drastically changes the received fluence at the top of the Earth's atmosphere. However, any such variations are lost as the SN material descends through our atmosphere, and the final global distribution is due primarily to

atmospheric influences with slight alterations due to ocean cycling. This confirms an isotropic deposition on the Earth's surface as a reasonable assumption when making order of magnitude calculations. This in turn removes an uncertainty in estimates of the distance to the ^{60}Fe progenitor, which may have been within the Sco-Cen or Tuc-Hor stellar groups.

In contrast, the memory of the angle of arrival would be retained in deposits on airless Solar System bodies such as the Moon. We find that lunar samples should show significant variation in SN ^{60}Fe abundance if the source was in the Tuc-Hor or the Sco-Cen groups. Thus the ^{60}Fe pattern on the Moon in principle can give directional information, serving as a low-resolution "antenna" that could potentially test proposed source directions.

Lastly, our examination assumes the passage of a single SN. In studying Solar System/terrestrial influences on SN ^{60}Fe, we find that none are capable of extending the signal postulated by Fry et al. (2015) to the wider signal detected by Feige (2014) and Wallner et al. (2016). This supports the assertion by Breitschwerdt et al. (2016) and Wallner et al. (2016) of multiple SNe producing the ^{60}Fe signal.

3.2 Motivation

Fry et al. (2015) defined the decay-corrected fluence as that measured at the time the signal arrived.[2] However, inherent in the formula used in Fry et al. (2015) (and in all other studies known to us) was the assumption that the material was distributed uniformly, that is, *isotropically*, over Earth's entire surface. Here we examine this assumption in detail. In fact, the arriving SN blast will be highly directional, roughly a plane wave on Solar System scales (Fields et al., 2008).

In this paper, we will assume that all SN dust will be entrained in the blast plasma

[2]Other descriptions of fluence have been used in the literature, but here we deal exclusively with the arrival/decay-corrected fluence. For a full description see Fry et al. (2015).

as it arrives in the Solar System. That is, we ignore any relative motion of the dust in the blast. [3] Thus the dust will arrive with the same velocity vector as the blast. The SN dust particles will then encounter the blast/solar wind interface, decouple, and be injected into the Solar System with a plane-wave geometry.

As SN dust traverses the Solar System, it passes through magnetic fields, multiple layers of the Earth's atmosphere and water currents until finally being deposited on the ocean floor. In addition, because we would expect dust from a SN to arrive as a plane wave as the Earth rotates, different regions would have become exposed to the wave for different durations. Relaxing the assumption of uniformly distributed debris deposition gives:[4]

$$\mathcal{F}(lat, lon) = \psi(lat, lon) \left(\frac{1}{4}\right) \left(\frac{M_{\rm ej}}{4\pi D^2 A m_u}\right) U f e^{-t_{\rm travel}/\tau}\,, \tag{3.1}$$

where $\mathcal{F}(lat, lon)$ is the fluence of the isotope at the time the signal arrives at a location with latitude and longitude (lat, lon) on Earth's surface. Here $M_{\rm ej}$ is the mass of the ejected isotope, D is the distance the isotope travels from the SN to Earth, A is the atomic mass of the isotope, m_u is the atomic mass unit, U is the uptake efficiency of the material the isotope is sampled from, f is the fraction of the isotope in the form of dust that reaches Earth, $t_{\rm travel}$ is the time taken by the isotope to travel from the SN to Earth, and τ is the mean lifetime of the isotope. The factor of $1/4$ comes from the ratio of Earth's cross-section to its surface area, and the factor 4π assumes spherical symmetry in the SN's expansion. The uptake efficiency is a measure of how readily a material incorporates the elements deposited on it. Sediment accepts nearly all deposited elements, so we assume $U_{\rm sediment} = 1$. However, the Fe-Mn crust

[3] More precisely, we assume that any velocity dispersion among dust particles and relative to the plasma will be small compared to the bulk plasma velocity. We will relax this assumption in a forthcoming paper.

[4] The subscript i sometimes appears in the literature (see e.g., Fry et al., 2015). This refers to the specific isotope/element being examined, but for this paper, we will be examining ^{60}Fe only, so the subscript is not used here.

incorporates iron through a chemical leaching process, so the uptake for iron into the crust is thought to lie in the range $U_{\rm crust} \approx 0.1 - 1$ (for more discussion, see Feige et al., 2012; Feige, 2014; Fry et al., 2015; Wallner et al., 2016). In order to account for concentrations and dilutions in the deposition of SN material, we include a factor ψ to represent the deviation from a uniform distribution ($\psi = 1$), where $\psi \in [0,\ 1)$ implies a diluted deposition and $\psi > 1$ implies a concentrated deposition.

When we compare samples from different terrestrial locations, most of the quantities in Equation (3.1) disappear, so that the fluence ratios depend only on the uptake and distribution factors:

$$\begin{aligned}\frac{\mathcal{F}_{\rm Fitoussi}}{\mathcal{F}_{\rm Knie}} &= \frac{\left(\frac{\psi_{\rm Fitoussi}}{4}\right)\left(\frac{M_{\rm ej}}{4\pi D^2 A m_u}\right) U_{\rm Fitoussi} f e^{-t_{\rm travel}/\tau}}{\left(\frac{\psi_{\rm Knie}}{4}\right)\left(\frac{M_{\rm ej}}{4\pi D^2 A m_u}\right) U_{\rm Knie} f e^{-t_{\rm travel}/\tau}} \\ &= \frac{U_{\rm Fitoussi}\psi_{\rm Fitoussi}}{U_{\rm Knie}\psi_{\rm Knie}}\,. \end{aligned} \tag{3.2}$$

Similarly:

$$\frac{\mathcal{F}_{\rm Fitoussi}}{\mathcal{F}_{\rm Feige}} = \frac{U_{\rm Fitoussi}\psi_{\rm Fitoussi}}{U_{\rm Feige}\psi_{\rm Feige}}\,, \tag{3.3}$$

$$\frac{\mathcal{F}_{\rm Feige}}{\mathcal{F}_{\rm Knie}} = \frac{U_{\rm Feige}\psi_{\rm Feige}}{U_{\rm Knie}\psi_{\rm Knie}}\,. \tag{3.4}$$

Using these relations, we can test a distribution model against observations.

3.3 ^{60}Fe Fluence Observations

We examine three studies of ^{60}Fe measurements: Knie et al. (2004), Fitoussi et al. (2008), and Feige (2014). These studies have considerable overlap in their time periods and greatly varying locations on the Earth. We do not examine the Wallner et al. (2016) measurements in detail, first, because the bulk of the analysis for this paper was completed and submitted for review prior to the publication of Wallner et al.

(2016), and second, because many of the samples included in Wallner et al. (2016) are either already included in the other studies, do not cover the period around the 2.2-Myr signal, or were drawn from similar latitudes as the other samples.

3.3.1 Knie et al. (2004) Sample

The Knie et al. (2004) study used the hydrogenous deep-ocean Fe-Mn crust 237KD from 9°18' N, 146°03' W (∼1,600 km/1,000 mi SE of Hawaii). The crust growth rate is estimated at 2.37 mm Myr^{-1} (Fitoussi et al., 2008), and samples were taken at separations corresponding to 440- and 880-kyr time intervals. Knie et al. originally estimated that the ^{60}Fe signal occurred 2.8 Myr ago with a decay-corrected fluence of $(2.9 \pm 1.0) \times 10^6$ atoms cm^{-2}. However, at the time of their analysis, the half-life of ^{60}Fe was estimated to be 1.49 Myr, and the half-life of ^{10}Be (which was used to date individual layers) was estimated to be 1.51 Myr. Current best estimates for these values are $\tau_{1/2,\,^{60}\mathrm{Fe}} = 2.60$ Myr (Rugel et al., 2009; Wallner et al., 2015b) and $\tau_{1/2,\,^{10}\mathrm{Be}} = 1.387$ Myr (Chmeleff et al., 2010; Korschinek et al., 2010). This changes the estimated signal arrival time to 2.2 Myr ago, and gives a decay-corrected fluence of $\mathcal{F}_{\mathrm{Knie}} = (1.41 \pm 0.49) \times 10^6$ atoms cm^{-2}. Additionally, Knie et al. used an iron uptake efficiency of $U_{\mathrm{crust}} = 0.006$, whereas more recent studies suggest that the uptake for the crust is much higher, $U_{\mathrm{crust}} \approx 0.1 - 1$ (Bishop & Egli, 2011; Feige, 2014; Wallner et al., 2016). In this paper, we consider a "Medium" case that uses the Knie fluence of $\mathcal{F}_{\mathrm{Knie}} = (1.41 \pm 0.49) \times 10^6$ atoms cm^{-2} and an uptake of $U_{\mathrm{crust}} = 0.5$, but we also examine the possibilities that the uptake is higher ($U_{\mathrm{crust}} = 1$) and lower ($U_{\mathrm{crust}} = 0.1$). Of special note, Feige (2014) and Wallner et al. (2016) found $U_{\mathrm{crust}} \in [0.07, 0.17]$; both studies assumed an isotropic terrestrial distribution and found $U_{\mathrm{crust}} \approx 0.1$ by comparing crust and sediment fluences. Because the sediment samples came from the Indian Ocean, and the crust samples came from the Pacific and Atlantic Oceans, the distribution factor could potentially be pertinent, so we consider a range of U_{crust}

values.

3.3.2 Fitoussi et al. (2008) Samples

Fitoussi et al. (2008) performed measurements on both Fe-Mn crust and sea sediment. The Fitoussi crust sample came from the same Fe-Mn crust used by Knie et al. (2004), but from a different section of it. The Fitoussi sea sediment samples are from 66°56.5' N, 6°27.0' W in the North Atlantic (∼400 km/250 mi NE of Iceland). The average sedimentation rate for the samples is 3 cm kyr^{-1}, and slices were made corresponding to time intervals of $10 - 15$ kyr. The sediment samples had a density 1.6 g cm^{-3} and an average iron weight fraction 0.5 wt%. Fitoussi et al. (2008) examined the period $1.68 - 3.2$ Myr ago, but found no significant ^{60}Fe signal above the background level like that found in the Knie crust sample (Figure 3, Fitoussi et al., 2008). In an effort to further analyze their results, they calculated the running means for the samples using data intervals of ∼400 and 800 kyr (Figure 4, Fitoussi et al., 2008). This allowed the narrower sediment time intervals to be compared to the longer crust time intervals. They also considered the lowest observed sample measurement as the background level, rather than the total mean value used initially. In this instance, they found a signal of marginal significance in the 400-kyr running mean centered at ∼2.4 Myr of ^{60}Fe/Fe$= (2.6 \pm 0.8) \times 10^{-16}$.

For this paper, we consider as part of our "Medium" scenario a non-detection by Fitoussi et al. (2008) (in other words, $\mathcal{F}_{\text{Fitoussi}} = 0$ atoms cm^{-2}). In addition, we assume an upper limit set by non-detection of a signal in the Fitoussi et al. (2008) sediments because of a high sedimentation rate. This is motivated by initial Fitoussi et al. (2008) measurements that found a slightly elevated ^{60}Fe abundance at ∼2.25 Myr ago, but were not significant because they were not sufficiently above the background (Fitoussi et al., 2008). To determine this upper limit, we first calculate the number

density of iron in the sediment (Feige et al., 2012):

$$n_{\rm Fe} = \frac{wN_A\rho}{A}\,, \tag{3.5}$$

where $w = 0.005$ is the weight fraction of iron in the samples, N_A is Avogadro's number, $\rho = 1.6$ g cm^{-3} is the mass density of the sample, and $A = 55.845$ g mol^{-1} is the molar mass for iron. This yields a number density of $n_{\rm Fe} = 8.6 \times 10^{19}$ atoms cm^{-3}. Using the marginally significant signal to calculate the ^{60}Fe number density, we find $n_{^{60}{\rm Fe}} = 8.6 \times 10^{19}$ atoms cm$^{-3} \cdot 2.6 \times 10^{-16} = 2.2 \times 10^{4}$ atoms cm^{-3}. An 870-kyr time interval (in order to compare to the fluence quoted by Knie et al. (2004) corresponds to a length of 2610 cm, and gives an upper limit on the fluence of 5.9×10^{7} atoms cm^{-2}. Correcting for radioactive decay gives the following upper limit on the fluence at the time the signal arrived:

$$\mathcal{F}_{\rm Fitoussi} \leq \frac{5.9 \times 10^{7}\ \text{atoms cm}^{-2}}{2^{-2.2\ \text{Myr}/2.60\ \text{Myr}}} \Rightarrow \mathcal{F}_{\rm Fitoussi} \leq 1.1 \times 10^{8}\ \text{atoms cm}^{-2}\,. \tag{3.6}$$

3.3.3 Feige (2014) Samples

Feige (2014) studied four sea sediment samples from the South Australian Basin in the Indian Ocean (1,000 km/620 mi SW of Australia). Three of the sediment cores cover the time period examined by Knie et al. (2004) and Fitoussi et al. (2008): ELT45-21 (39°00.00' S, 103°33.00' E), ELT49-53 (37°51.57' S, 100°01.73' E) and ELT50-02 (39°57.47' S, 104°55.69' E). They have an average density of 1.35 g cm^{-3}, an average iron weight fraction of 0.2 wt%, and sedimentation rates of 4 mm kyr^{-1} for ELT45-21 and ELT50-02 and 3 mm kyr^{-1} for ELT49-53. Feige (2014) studied samples from $0-4.5$ Myr ago, primarily in the time period of the Knie signal and was able to corroborate it, finding a decay-corrected fluence $\mathcal{F}_{\rm Feige} = (1.42 \pm 0.37) \times 10^{7}$ atoms cm^{-2}. For our "Medium" scenario, we adopt the Feige (2014) fluence and assume that the uptake for

sediment (for both the Fitoussi et al. (2008) and Feige (2014) samples) is $U_{\text{sediment}} = 1$. In our model comparisons, we use the location of the ELT49-53 sample. Table 3.1 summarizes the assumptions we use in our modeling.

Table 3.1: Model Cases, Uptakes, and Fluences

Case	U_{crust}	U_{sediment}
High Uptake	1	1
Medium Uptake	0.5	1
Low Uptake	0.1	1
$\mathcal{F}_{\text{Knie}}$	$\mathcal{F}_{\text{Fitoussi}}$	$\mathcal{F}_{\text{Feige}}$
$(1.41 \pm 0.49) \times 10^6$	$\leq 1.0 \times 10^8$	$(1.42 \pm 0.37) \times 10^7$

Fluences are given in atoms cm^{-2}

3.4 Deposit Considerations

As noted above, in this paper we assume that the dust grains are entrained within the SN shock until it reaches the Heliosphere, at which time the dust grains decouple from the shock and enter the Solar System, where they are affected by the magnetic fields present. Apart from the Sun's magnetic, gravitational, and radiative influences, we consider only Earth's magnetic and gravitational influences and ignore those of other objects in the Solar System (e.g., the Moon, Jupiter, etc.). We describe the dust with fiducial values of grain radius $a \geq 0.2$ μm, charge corresponding to a voltage $\mathcal{V} = 5$ V, and initial velocity $v_{\text{grain},0} \geq 40$ km s^{-1}.[5]

[5]These values are based on the findings in Fry et al. (2015). Dust grains are expected to be larger than 0.2 μm in order to reach Earth, 5 V is a typical voltage for interstellar grains, and 40 km s^{-1} is a typical arrival velocity for the SN shock (Table 3, Fry et al., 2015)

3.4.1 Magnetic Deflection

The grains will experience a number of forces upon entering the Solar System: drag from collisions with the solar wind, radiation pressure from sunlight, gravity from the Sun and Earth, and a Lorentz force from magnetic fields since the grains will most likely be charged. Athanassiadou & Fields (2011) studied these effects in detail for SN grains, though with somewhat different SN parameters than are now favored, primarily due to the possible large revisions in crust uptake values. Nevertheless, following Athanassiadou & Fields (2011), we expect the influence of magnetic fields to be the dominant force for most of the grains traveling through interplanetary space. With our fiducial SN dust properties, we would not expect drag from the solar wind to affect the dust grains significantly, given that the drag stopping distance $R_{\rm drag}$ is much larger than the size of the Solar System (Murray et al., 2004):[6]

$$R_{\rm drag} = 1.7 \text{ pc} \left(\frac{\rho_{\rm grain}}{3.5 \text{ g cm}^{-3}} \right) \left(\frac{a}{0.2 \ \mu\text{m}} \right) \left(\frac{7.5 \text{ cm}^{-3}}{n_{\rm H}} \right) . \tag{3.7}$$

The remaining forces (gravitational, radiation, and magnetic) have comparable values.

As noted in Fry et al. (2015), for a ratio of the Sun's radiation force ($F_{\rm rad}$) to its gravitational force ($F_{\rm grav}$), $\beta \lesssim 1.3$, the dust grains will reach Earth's orbit:

$$\beta \equiv \frac{F_{\rm rad}}{F_{\rm grav}} = 0.8 \left(\frac{C_{\rm r}}{7.6 \times 10^{-5} \text{ g cm}^{-2}} \right) \left(\frac{Q_{\rm pr}}{1} \right) \left(\frac{3.5 \text{ g cm}^{-3}}{\rho_{\rm grain}} \right) \left(\frac{0.2 \ \mu\text{m}}{a} \right) , \tag{3.8}$$

where $C_{\rm r}$ is a constant and $Q_{\rm pr}$ is the efficiency of the radiation pressure on the grain (for more detail see Gustafson, 1994).

The field strength of the interplanetary magnetic field (IMF, generated by the Sun) varies from a value of $B \sim 0.1$ μG at 100 AU to $B \sim 50$ μG at 1 AU. This implies

[6]This is the stopping distance for a supersonic dust grain. Although the grains are moving subsonically relative to the Sun, they are supersonic relative to the outward-flowing solar wind ($v_{\rm SW} \approx$ 400 km s^{-1}).

the ratio of the magnetic to gravitational force varies over a range that is at least $F_{\rm mag}/F_{\rm grav} \approx 0.03 - 2$:

$$\frac{F_{\rm mag}}{F_{\rm grav}} = 2 \left(\frac{\mathcal{V}}{5\ {\rm V}}\right) \left(\frac{B}{0.3\ \mu{\rm G}}\right) \left(\frac{v}{40\ {\rm km\ s^{-1}}}\right) \left(\frac{r}{100\ {\rm AU}}\right)^2 \left(\frac{3.5\ {\rm g\ cm^{-3}}}{\rho_{\rm grain}}\right) \left(\frac{0.2\ \mu{\rm m}}{a}\right)^2 . \tag{3.9}$$

Both the IMF and the Magnetosphere (generated by the Earth) have similar strengths at the surfaces of their respective sources ($B \sim 1$ G), that weaken rapidly further away. Beyond 1 AU, the IMF is less than 100 μG, likewise the tail portion of the Magnetosphere asymptotically approaches 100 μG. Because the Sun's radiation and gravitational forces are of similar magnitude, but opposite directions, we can estimate the influence of magnetic fields on the incoming SN dust grains before the in-depth numerical discussion below. If we calculate the gyroradius for our fiducial grain values, we get (Murray et al., 2004):

$$R_{\rm mag} = 28\ {\rm AU} \left(\frac{\rho_{\rm grain}}{3.5\ {\rm g\ cm^{-3}}}\right) \left(\frac{5\ {\rm V}}{\mathcal{V}}\right) \left(\frac{100\ \mu{\rm G}}{B}\right) \left(\frac{v_{\rm grain,0}}{40\ {\rm km\ s^{-1}}}\right) \left(\frac{a}{0.2\ \mu{\rm m}}\right)^2 . \tag{3.10}$$

Given the sizes of the Solar System (∼100 AU) and the Magnetosphere (∼1000 $R_\oplus$, "$\oplus$" refers to the Earth), we would expect some deflection by the IMF, though not a complete disruption since the IMF weakens by several orders of magnitude beyond 1 AU, whereas the Magnetosphere should cause very little deflection of the dust grains. The numerical results below confirm this expectation, as summarized in Table 3.2.

Heliosphere Transit

The IMF has a shape resembling an Archimedean spiral due to a combination of a frozen-in magnetic field, the Sun's rotation, and an outward flowing solar wind (Parker, 1963). At Earth's orbit, the IMF has a value of $\vec{B}_{r,\theta,\phi} = \langle 30, 0, 30 \rangle\ \mu$G (Gustafson, 1994), with the azimuthal component dominating at larger radii (Parker,

1958). Athanassiadou & Fields (2011) studied the passage of SN dust grains through the IMF, and calculated their deflection, but for velocities $\geq$ 100 km s^{-1}. In this section we expand on Athanassiadou & Fields's treatment by looking at slower initial grain velocities and solving numerically the equations of motion for the dust grain.

$$m_{\rm grain}\frac{d\vec{v}_{\rm grain}}{dt} = \vec{F}_{\rm grav,\odot} + \vec{F}_{\rm rad,\odot} + \vec{F}_{\rm mag,\odot} \tag{3.11}$$

We include the Lorentz force, $\vec{F}_{\rm mag,\odot}$, due to the IMF as well as the Sun's gravity, $\vec{F}_{\rm grav,\odot}$, and radiation, $\vec{F}_{\rm rad,\odot}$, forces. Grain erosion is not included since the erosion timescale is much longer than the crossing time for the grains; neither are changes in grain charge since we expect the charge remains fairly constant once it enters the Solar System (Kimura & Mann, 1998). Our results are in good agreement with the broader and more detailed examination completed by Sterken et al. (2012, 2013)

The grains begin 110 AU from the Sun and have initial velocities directed at a location 1 AU away from the Sun representing Earth. We vary the initial grain directions, speeds, charges, and sizes, and solve for the angle between the grain's initial direction and the line between the grain's starting location and closest approach to Earth's location. For our fiducial grain values, they experienced $\lesssim 1^\circ$ of deflection, and, since their velocities were greater than the solar escape velocity, they continued out of the Solar System after passing Earth's orbit. Additionally, when examined as a plane wave, the grains showed a fairly uniform deflection amongst neighboring grains until closest approach, meaning that, even though a grain that was initially aimed at Earth would miss by $\sim 1^\circ$, another neighboring grain would be deflected into the Earth. These results suggest that direction information of the grains' source would be retained to within 1°, and that spatial and temporal dilutions/concentrations of the ^{60}Fe signal can be ignored, see Figure 3.1.

Earth's Magnetosphere Transit

The Earth's Magnetosphere has a teardrop shape, with field lines on the day-side being compressed by solar wind pressure on the plasma frozen in the Magnetosphere, and being stretched on the night-side nearly parallel to one another. The day-side edge is located $\sim$10 $R_\oplus$ with a field strength about twice that of the dipole value (§6.3.2, Kivelson & Russell, 1995). The night-side tail extends out to $\sim$1000 $R_\oplus$ with a radius of $\sim$30 $R_\oplus$ (§9.3, Kivelson & Russell, 1995). It reaches asymptotically a field strength $B_{X0} \approx 100$ μG (Slavin et al., 1985) and has a current sheet half-height of $H = R_\oplus/2$ (Tsyganenko, 1989). We use the Magnetosphere approximation from Katsiaris & Psillakis (1987); this model is a superposition of a dipole field ($\vec{B}_{\rm dipole}$) near Earth (Dragt, 1965) and an asymptotic sheet ($\vec{B}_{\rm tail}$) for the magnetotail region (Wagner et al., 1979). This approximation does not include the inclination of the dipole field to the orbital plane but, given the motion and flipping of the magnetic poles, this approximation should suffice for examining general properties. We assume a magnetic dipole strength based on the equatorial surface value of $M \approx 1$ G $R_\oplus^3$, and assume that the tail magnetic field normal component $B_{Z0} \approx 0.06 B_{X0}$ (Slavin et al., 1985). When we solve the equations of motion (Equation (3.11) adding the Lorentz force due to the Magnetosphere, $\vec{F}_{\rm mag,\oplus}$, and Earth's gravity, $\vec{F}_{\rm grav,\oplus}$) for a charged particle in a magnetic field starting at various locations at the edge of the Magnetosphere moving towards the Earth, we find deflections are $\lesssim 3$ arcmin when using our fiducial grain values. Like the IMF, the grains show uniform deflections passing through the Magnetosphere, suggesting that direction information of the grains' source would be retained to within 10 arcmin, and that spatial and temporal dilutions/concentrations of the ^{60}Fe signal can be ignored, see Figure 3.2.

3.4.2 Upper Atmosphere Distribution

Once the SN dust has passed through the IMF and Magnetosphere, it impacts the upper atmosphere (generally at ∼100 km in altitude, see §3.4.3). Because the IMF and Magnetosphere show little deflection, we expect a relatively coherent, nearly plane-wave flow of incident dust onto Earth's upper atmosphere. Once the grains reach Earth, they will impinge onto Earth's cross-section facing the dust wave. The upper atmosphere distribution will depend on Earth's rotation and precession and the angle of arrival of the dust (see Figure 3.3). To find the dust distribution in the upper atmosphere where the SN material impacts and before it begins to pass through the rest of the atmosphere, we approximate the Earth as a perfect sphere that rotates about the z-axis. We divide the surface of the Earth into sectors of angular size $\Delta\theta \times \Delta\phi$, with θ and ϕ analogous to latitude and longitude, respectively. Because the duration of the SN dust storm is likely to be long ($\Delta t_{\text{signal}} \sim 100$ kyr), we include Earth's axial precession ($\Delta t_{\text{precessional}} = 26$ kyr). We ignore nutation of Earth's axis, since it is small (∼arcseconds) compared to the Earth's inclination ($\alpha \approx 23.3°$). Because the SN progenitor is far away ($D > 10$ pc), we assume the direction of the particle flux does not change with time and its intensity is uniform, so we ignore Earth's change in position through its orbit. We also assume that the SN dust intensity varies with time according to the saw-tooth pattern used in Fry et al. (2015): the initial flux ($\mathbb{F}_0$) starts at a maximum and decreases linearly to 0 at $t = \Delta t_{\text{signal}}$.

In order to determine the fluence received at a given location on Earth, we use a series of coordinate transformations from the Earth's surface/terrestrial (unprimed) frame to the propagating shock wave/interstellar ($''''$) frame. For a detailed description of our transformations, see Appendix 3.7.

Our simulations were run assuming a SN signal duration of $\Delta t_{\text{signal}} = 351$ kyr (the approximate expected duration for an ECSN, Fry et al., 2015). Because $\Delta t_{\text{signal}} >$

$\Delta t_{\text{precession}}$, the model showed little dependence on the signal duration after the first precession cycle (terrestrial models were run for the entire SN signal width: 351 kyr; lunar models were run for four precession cycles: 74 yr). The same is true for a constant flux profile versus a saw-tooth profile. Because the model includes two vastly different time scales (precessional and daily), we used two different time steps. The precessional time steps were made when the precession progressed by an angle $\Delta\phi/2$. In other words:

$$\Delta t_{\text{precessional step}} = \left(\frac{26 \text{ kyr}}{360^\circ}\right)\left(\frac{\Delta\phi}{2}\right) . \tag{3.12}$$

At each precessional time step, the model is run for one daily rotation, with the daily time steps made when the daily rotation progresses by an angle $\Delta\phi/2$, or:

$$\Delta t_{\text{daily step}} = \left(\frac{86400 \text{ s}}{360^\circ}\right)\left(\frac{\Delta\phi}{2}\right) . \tag{3.13}$$

Precession still occurs during the daily time steps, but the effects of the daily rotation dominate. As we ran our model, the various angles η represent different arrival directions from the source of the ^{60}Fe signal as measured from the Ecliptic North Pole. Because of Earth's precession and rotation, these possible directions form a ring of constant Ecliptic latitude.

Figure 3.3 shows sample results for our upper atmosphere distribution model, and we can see for the $\eta = 90^\circ$ case, there is a nearly isotropic distribution of particles onto the entire atmosphere; $\psi_{\text{Upper Atmo, }\eta=90^\circ} \in [0.5,\ 1.2]$. As η increases to 180°, the North Pole becomes increasingly depleted ($\psi \to 0$), and the South Pole becomes increasingly saturated (the $\eta \in [0,\ 90^\circ)$ case mirrors this result). At $\eta = 180^\circ$, the saturation reaches a maximum; $\psi_{\text{Upper Atmo, }\eta=180^\circ} \in [0,\ 3.7]$.

We see in Figure 3.3 that the arrival distribution of SN material is uniform across longitudes (i.e., constant at a fixed latitude). This arises primarily due to the daily rotation, with some additional smearing due to precessional rotation. Conversely,

the distribution of SN dust on the upper atmosphere is strongly nonuniform across latitudes. The latitude gradient largely reflects the direction of the SN itself, with some smearing due to precession. As we will see, the fate of this SN signature is very different for the Earth and Moon.

3.4.3 Wind Deflection

Interstellar dust containing ^{60}Fe could be subject to two types of wind effects: initial deflection through the atmosphere and subsequent transplantation from a landmass into the ocean. Since the solar wind has little influence on the SN dust grains, they would enter Earth's atmosphere at approximately the same speed they entered the Solar System: $v_{\text{SN grains}} \approx 40 - 100$ km s^{-1}. Although this is faster than typical meteoritic dust infall velocities, we would expect SN dust to be ablated at similar altitudes to meteoritic dust because both are traveling supersonically relative to the surrounding air and the stopping distance is independent of the initial velocity: in the supersonic limit, the e-folding stopping distance for dust grains is independent of their initial velocity (Murray et al., 2004). This implies that the SN dust grains would come to rest relative to the atmosphere in the upper mesosphere/lower thermosphere (MLT, $\sim$90 $-$ 115 km above sea level, Feng et al., 2013). However, because of their high velocities, we would expect the SN grains to be completely ablated upon impact with the atmosphere, and thus vaporized. At this point, the SN ^{60}Fe vapor would descend through the atmosphere (see Figure 3.4).

We expect that the SN dust grains and meteoritic dust grains would be similar in size ($a \sim 0.1 - 1$ μm), so their ablation and fragmentation properties would also be similar. The SN grains would be ablated at altitudes similar to where meteoric grains are ablated, and both would descend through the atmosphere in a similar manner. Their compositions (iron oxides and silicates) are identical, so both SN and meteoritic materials would experience similar chemical reactions in the atmosphere. Because of

these similarities, we use the extensive work already accomplished on meteoric smoke particles (e.g., Plane et al., 2015, and references therein).

Once delivered to the MLT, the SN material would sediment out to the surface over the course of $4 - 6$ years (Dhomse et al., 2013). As noted in §3.4.2, because of Earth's rotation and precession, the upper atmosphere distribution forms bands of uniform fluences across lines of latitude. Since zonal (east-west) deflection would not affect that pattern, we focus on deflections due to meridional (north-south) winds. In the MLT, meridional winds are of the order $v_{\text{MLT winds}} \sim 10$ m s^{-1} and can be several orders of magnitude greater than the vertical component (Figure 1, Plane et al., 2015). These winds could drive the SN material from one pole to the other within a few days while descending only a few kilometers. An example of this movement was the plume from the launch of STS-107 on January 16, 2003: within ∼80 hr the plume had traveled from the eastern coast of Florida to the Antarctic (Niciejewski et al., 2011). Downward transport through the mesosphere-stratosphere-troposphere occurs mainly in the polar regions: this leads to a semi-annual oscillation of meteoritic smoke particles from pole to pole that would effectively isotropize (or at least randomize) the distribution of incoming SN material in the mesosphere.

In addition, the vaporized SN ^{60}Fe would be highly soluble and would combine with sulphates as it descended through the stratosphere (Dhomse et al., 2013). This means the SN material would be readily incorporated into clouds when it finally reaches the troposphere (Saunders et al., 2012). Because the SN ^{60}Fe would behave similarly to meteoritic iron, we can use simulations of the meteoritic smoke particles to find the final distribution of SN ^{60}Fe at the surface. Dhomse et al. (2013) studied the transport of ^{238}Pu through the atmosphere and later applied their model to iron deposition, finding the distribution over the entire Earth, with asymmetries in the mid-latitudes due to the stratosphere-troposphere exchange (see Figure 3b, Dhomse et al., 2013).

After descending through the atmosphere, it is possible for interstellar dust grains

that have fallen through the atmosphere and been deposited on land to later be picked up by wind again, carried to the ocean, and be deposited there. This process of dust transplantation (also called aeolian dust), could lead to an enhancement of ^{60}Fe levels in ocean samples. In the case of our studied samples, however, this should not be an issue. Based on a study by Jickells et al. (2005), aeolian iron dust deposits are low in the area of the Knie et al. (2004) and Feige (2014) samples. While slightly higher than the other locations, the Fitoussi et al. (2008) sample should not be affected because of where the dust was transplanted from. In the case of the Fitoussi sediment samples, the material will be transplanted from equatorial regions (e.g., to the Sahara, Arabian, and Gobi deserts), but as described in (see Figure 3b, Dhomse et al., 2013), these areas will receive very little SN material so we would expect the transplanted dust to contain a negligible amount of SN ^{60}Fe.[7] Therefore, for the purposes of this paper we ignore dust transplantation, but future studies should consult Jickells et al. (2005) to check if transplantation is an issue.

3.4.4 Water Deflection

As mentioned in §3.4.3, the SN material would be highly soluble due to its complete ablation in the MLT. This means that when it reached the ocean it would be incorporated readily into organisms, particularly phytoplankton (Boyd & Ellwood, 2010). In many locations, the availability of iron is the limiting factor for phytoplankton growth (Figure 7, Moore et al., 2004). In locations where there is an abundance of iron (i.e., high concentrations of soluble iron, most likely due to meteoric or aeolian sources, and iron is not the limiting element), the residence time for iron is very short ($\sim$days and months), but in locations of lower abundance of Fe, the residence time is longer ($\sim 100 - 200$ years) (Bruland et al., 1994; Croot et al., 2004). In either case, these

[7]Moreover, our use of an upper limit for the Fitoussi sample should allow for any transplantation enhancement.

residence times are much less than the ocean circulation time (∼1000 years).

When quantifying the distribution of iron as it descends in the ocean, a number of considerations need to be included, not only the initial location of iron, the water velocity and its depth, but also the complexation of iron with organic ligands, the availability of other nutrients such as phosphates and nitrates, seasonal patterns, ocean floor topography, and the amount of light exposure. Several studies have examined iron cycling in the ocean (see e.g., LefèVre & Watson, 1999; Archer & Johnson, 2000; Parekh et al., 2004; Dutkiewicz et al., 2005, 2012). However, all of these studies examine the total iron input into oceans, the dominant source being aeolian dust which is highly insoluble, rather than meteoritic sources that are highly soluble but account for only 10^{-4} of the total iron input mass (Jickells et al., 2005; Plane, 2012).

A more recent study by Moore & Braucher (2008) examined the global cycling of iron and updated the Biogeochemical Elemental Cycling (BEC) ocean model, resulting in an improved model that showed better agreement with observations. As part of this study, Moore & Braucher simulated the concentrations of dissolved iron at varying ocean depths; of particular interest are the simulations of "Only Dust" inputs (see Figures 11d, 12d, 13d, and 14d, Moore & Braucher, 2008). While the dust used in the simulation is primarily from an aeolian source, it acts similarly to meteoric dust (or interstellar SN dust) upon reaching the ocean. Since the residence time of iron is much less than the ocean circulation time, we can approximate the ocean currents as "conveyor belts", moving different concentrations of iron to different areas of the ocean, but not significantly altering the concentration of a fluid element as it descends. With this assumption, we can find a first-order, initial location of the dust input by looking at the iron concentration over each ^{60}Fe sampling location in the lowest depths (Figure 14d, Moore & Braucher, 2008) and following it back to its source on the surface (Figure 11d, Moore & Braucher, 2008). With this initial location, we can use the meteoric dust distribution from Figure 3b, Dhomse et al. (2013) at that location to find

the relative fractions of SN ^{60}Fe that would eventually reach the sampling locations (see Figure 3.4). Using this method, we would expect the material deposited in the Knie crust sample to have originated from the Sea of Okhotsk off the northern coast of Japan, the Fitoussi sediment sample to have originated from the northwestern coast of Africa near the Strait of Gibraltar, and the Feige sediment sample to have originated between the southern tip of Africa and Antarctica.

3.5 Results

We present results of the surface distribution patterns for both the Earth and Moon.

3.5.1 Terrestrial ^{60}Fe Distribution

Comparing the various influences on the SN material, we find that the influence of the atmosphere (in particular, the MLT) would have been the greatest determining influence on the distribution of SN material at the sampling sites. The IMF, Magnetosphere, and water currents can deflect SN material, but these effects are small in scale and/or systematic in nature. Moreover, while the arrival angle, η, certainly causes global variations in received fluence, these variations would have been completely lost as the SN material descended through the MLT. A summary of a SN dust grain's transit is given Table 3.3.

Therefore, because motions in the MLT remove information of the original SN dust's direction, the terrestrial ^{60}Fe distribution provides no useful clues as to the SN origin on the sky. This is not to say, however, that the terrestrial ^{60}Fe distribution should be uniform. Rather, the surface pattern reflects terrestrial transport properties.

To find the distribution factors, ψ, we use the annual mean iron deposition rates from Dhomse et al. (2013) corresponding to the initial locations identified using Moore & Braucher (2008) and the model's total global input of 27 t day^{-1} $\Rightarrow$ $\mathbb{F}_{\text{global}}$ =

0.35 μmol m^{-2} yr^{-1}. This yields distribution factors at the sampling locations of: $\psi_{\text{Knie}} = 0.15/0.35 = 0.43$, $\psi_{\text{Fitoussi}} = 0.05/0.35 = 0.14$ and $\psi_{\text{Feige}} = 0.5/0.35 = 1.4$. These results are notable, first because they are not equal to unity, and secondly because they are still within an order of magnitude of unity. This means that if we compare the isotropic and anisotropic distributions in Equation (3.1), we find that $D_{\text{anisotropic}}/D_{\text{isotropic}} \approx \sqrt{\psi}$. Therefore, based on our estimated distribution factors, a SN distance calculated assuming an isotropic distribution would still be within of an order of magnitude of a full calculation including distribution effects. Using these distribution values and the uptake values for each case, we can compare the fluence ratio predictions with the observed values, as shown in Table 3.4.

3.5.2 Lunar ^{60}Fe Distribution

In contrast to the Earth, the airless and dessicated Moon will introduce none of the atmospheric and oceanic transport effects that influence the terrestrial ^{60}Fe deposition on the ocean floor. In particular, lunar deposition of SN debris will not suffer the large smearing over latitudes that plague material passing through the Earth's MLT. Consequently, the lunar distribution of SN debris holds to hope of retaining information about the SN direction.

Like Earth's upper atmosphere, dust grains impacting the lunar surface would be deflected $\lesssim 1^\circ$ from their passage through the Solar System, but the lunar deposits would not be further shifted by wind/water. Because atmospheric and ocean effects can be ignored, the SN directionality will be preserved. We can adapt the method for finding upper atmosphere deposition (§3.4.2 and Appendix 3.7) by using lunar parameters (daily period: 27 days, precessional period: 19 years, inclination angle: 6.7°). The deposition forms a banded pattern like that shown in Figure 3.5. We again see that the distribution is uniform across longitudes due to lunar rotation, but a latitude gradient persists and reflects the SN's direction, smeared somewhat by

precession. The upper left panel (Figure 3.5(a)) assumes $\eta = 110°$, corresponding to a SN in the Sco-Cen region, and the upper right panel (Figure 3.5(b)) is based on a source with $\eta = 155°$, corresponding to a SN in the Tuc-Hor region.

Fimiani et al. (2016) recently published measurements of lunar ^{60}Fe collected during the Apollo Moon landings. The measurements cover a range of depths, but an impactor will only penetrate to a depth on order with its diameter ($\sim \mu$m for our SN grains), so we compare only the fluences of the shallowest samples (this will allow for some minor gardening as noted by Fimiani et al., 2016, and references therein). We calculated fluences as outlined in §3.3.2, adjusted for 10% cosmogenic (i.e., cosmic ray-produced) ^{60}Fe, and plotted the results against the expected Sco-Cen and Tuc-Hor relative fluences in Figure 3.5(c). Since we do not know the actual fluence for an isotropic distribution on the Moon, we scaled the fluences to the 12025,14 sample fluence. We see that it is not yet possible to differentiate between a Sco-Cen or Tuc-Hor source because the samples were drawn near the lunar equator and the large uncertainties in the measurements (we also note that a future, more detailed examination should address the effects of regolith composition, gardening, and impactor penetration depth). The uncertainties are the result of low-number statistics (the two plotted 15008 values are from a total of four events, see Fimiani et al., 2016, Supplemental Information), but continued study will further refine these values.

3.6 Conclusions

After examining the major influences on SN material as it passes through the Solar System to the bottom of the ocean, we find that previous works' assumption of an isotropic terrestrial distribution of SN material was rather naïve but, based on our results, this assumption nevertheless yields calculated distances within an order of magnitude of a full calculation incorporating a distribution factor. The dominant

influence on the final distribution of SN material deposited on the Earth is the atmosphere, specifically the MLT region, due to strong zonal and meridional winds. This means that the suggestion by Fry et al. (2015) that the direction of arrival is the dominant cause of differing fluence measurements is incorrect. Whilst the angle of arrival of SN material can have drastic effects on the SN material's initial distribution in the upper atmosphere, these variations are completely masked as the material descends to the surface.

However, although the method outlined in §3.4.2 may not be applicable to finding the final distribution on Earth, ^{60}Fe measurements using lunar regolith could apply the method. We indeed find that the lunar distribution of ^{60}Fe retains information about the SN direction. Namely, lunar rotation and precession average over longitudes but preserve a latitude gradient that peaks near the SN latitude. The recent exciting detections of ^{60}Fe from Apollo soil core samples show a proof of principle that the Moon can act as a telescope pointing to the SN. As yet the data, clustered at the lunar equator, are too uncertain to cleanly discriminate the two putative star cluster origins (Sco-Cen versus Tuc-Hor), but future measurements – or ideally, a sample return mission from high and low lunar latitudes – could identify one possibility.

Clearly there are a number of uncertainties and assumptions included in our examination. The fluence ratios have large error uncertainties ($\sim$50%) or are simply upper limits. This is a by-product of the counting statistics in making the ^{60}Fe/Fe measurements, and future ^{60}Fe measurements will better constrain these values. The uncertainty in the value of $U_{\rm crust}$ further complicates the fluence ratios and, whilst most likely $U_{\rm crust} \in [0.1,\ 1]$, the use of sediment samples would be preferable since $U_{\rm sediment} \approx 1$ is much more certain. Lastly, the application of Moore & Braucher's updated BEC model to our SN ^{60}Fe ocean transport has some limitations. Although it includes many of the relevant considerations outlined in §3.4.4, it focuses on aeolian dust sources of iron rather than meteoric sources, which have a different starting

distribution. Additionally, the updated BEC simulations match observations better than the previous model, but still rely on observations primarily from the northern Pacific Ocean (Moore & Braucher, 2008) and underestimate the deep ocean iron concentrations. Also, we used a general conveyor belt assumption of the movement of iron in Moore & Braucher's results, rather than following tracer particles to understand better any possible dilutions or concentrations. Because generating an ocean model to track our SN ^{60}Fe material as it descends in the oceans with all the relevant factors described above is beyond the scope of this paper, we attribute any deviations from our observed fluence ratios and our predictions to errors in modeling iron transport within the oceans.

Based on our results, we can duplicate the observed fluence ratios. The predictions for the Medium case show good agreement with observations of all ratios. In the case of the $\mathcal{F}_{\rm Feige}/\mathcal{F}_{\rm Knie}$ ratio, the High and Low uptake values give ratios outside the error ranges and a factor $\sim$3 from the mean value. In addition, comparing the Feige (2014) and Wallner et al. (2016) calculation of $U_{\rm crust} \in [0.7, 0.17]$ assuming $\psi = 1$, we find good agreement with our Medium case and our calculated distribution factors. Revisiting Equation (3.4), for Feige (2014)/Wallner et al. (2016):

$$\frac{\mathcal{F}_{\rm Knie}}{\mathcal{F}_{\rm Feige}} = \frac{U_{\rm Knie}\psi_{\rm Knie}}{U_{\rm Feige}\psi_{\rm Feige}} = \frac{0.1 \cdot 1}{1 \cdot 1} = 0.1\,, \tag{3.14}$$

and for this work:

$$\frac{\mathcal{F}_{\rm Knie}}{\mathcal{F}_{\rm Feige}} = \frac{0.5 \cdot 0.43}{1 \cdot 1.4} = 0.15 \in [0.7, 0.17]\,. \tag{3.15}$$

Although it would be preferable to compare a sediment and crust sample drawn from the same place in the ocean to directly measure the crust uptake, this suggests that the Feige (2014); Wallner et al. (2016) $U_{\rm crust}$ values inherently include the distribution factors between sampling locations.

Moreover, using Equation (3.1), we see that changing the uptake also changes the

calculated distance to the source for a given observed fluence; increasing the uptake U increases the estimated distance, D, and conversely decreasing U decreases D. If we assume that the SN that produced the measured ^{60}Fe occurred in a stellar group (as opposed to being the explosion of an isolated star), we can compare the distances implied by each of our cases and the locations of the two candidate groups Sco-Cen and Tuc-Hor. Adapting the conditions outlined in Fry et al. (2015) to include the distribution factor, ψ, we find for an ECSN, in the Medium Uptake case, the implied distance is: $D = 46^{+10}_{-6}$ pc, which is consistent with the distance to Tuc-Hor ($\lesssim 60$ pc) but not with Sco-Cen ($\sim$130 pc). Table 3.5 summarizes the implied distances for our uptake cases.

Finally, with regards to the number of SNe producing the ^{60}Fe signal, we find no process within the Solar System that could spread the deposition of a single SN signal to appear like that found by Wallner et al. (2016). Such a process would need to allow concentrated ^{60}Fe to pass fairly undisturbed, but delay diluted ^{60}Fe. The only process to make such a distinction is ocean cycling, where the residence time for iron decreases when there is an overabundance of iron (§3.4.4), however, the delay is only $\sim$ 100 years not the $\gtrsim$ 100 kyr required to reproduce the Wallner et al. (2016) measurements. In addition, ^{60}Fe/Fe $\lesssim 10^{-14}$ in the ocean, so any ^{60}Fe of SN origin would have no appreciable effect on ocean iron abundance. This suggests either there were multiple SNe as postulated by Breitschwerdt et al. (2016) and Wallner et al. (2016) or another process within the ISM or SN remnant is responsible for spreading the signal.

3.7 Coordinate Transformations for Calculating Fluence onto a Sector

We define the Earth's terrestrial frame with the $+x$-axis passing through the equator at the 90° W-meridian, the $+y$-axis passing through the equator at the 0° meridian, and the $+z$-axis passing through the North Pole, as shown in Figure 3.6). We define spherical coordinates with θ as the polar angle from the $+z$-axis, ϕ as the azimuthal angle from the $+x$-axis, and r as the radial distance from the center of the Earth:

$$\begin{pmatrix} x \\ y \\ z \end{pmatrix} = \begin{pmatrix} r\sin\theta\cos\phi \\ r\sin\theta\sin\phi \\ r\cos\theta \end{pmatrix} . \tag{3.16}$$

We transform the terrestrial frame to Earth's rotating frame ($'$) by rotating about the z-axis with an angular speed of $\omega = 7.3\times10^{-5}$ rad s^{-1} (360°/1 day), see Figure 3.7(a):

$$\begin{pmatrix} x' \\ y' \\ z' \end{pmatrix} = \begin{pmatrix} \cos\omega t & -\sin\omega t & 0 \\ \sin\omega t & \cos\omega t & 0 \\ 0 & 0 & 1 \end{pmatrix} \begin{pmatrix} x \\ y \\ z \end{pmatrix} . \tag{3.17}$$

Next we transform to the inclination frame ($''$) by rotating about the x'-axis by an angle $\alpha = 23.3°$, see Figure 3.7(b):

$$\begin{pmatrix} x'' \\ y'' \\ z'' \end{pmatrix} = \begin{pmatrix} 1 & 0 & 0 \\ 0 & \cos\alpha & \sin\alpha \\ 0 & -\sin\alpha & \cos\alpha \end{pmatrix} \begin{pmatrix} x' \\ y' \\ z' \end{pmatrix} . \tag{3.18}$$

The next transformation is to the precessing/Ecliptic frame ($'''$) by rotating about the z''-axis with an angular speed of $\chi = 7.7\times10^{-12}$ rad s^{-1} (360°/26 kyr), see Figure

3.7(c):

$$\begin{pmatrix} x''' \\ y''' \\ z''' \end{pmatrix} = \begin{pmatrix} \cos\chi t & \sin\chi t & 0 \\ -\sin\chi t & \cos\chi t & 0 \\ 0 & 0 & 1 \end{pmatrix} \begin{pmatrix} x'' \\ y'' \\ z'' \end{pmatrix} . \tag{3.19}$$

Finally, we transform to the shock wave/interstellar frame ($''''$) by rotating about the x'''-axis by an angle η to account for different directions of arrival, see Figure 3.7(d):

$$\begin{pmatrix} x'''' \\ y'''' \\ z'''' \end{pmatrix} = \begin{pmatrix} 1 & 0 & 0 \\ 0 & \cos\eta & -\sin\eta \\ 0 & \sin\eta & \cos\eta \end{pmatrix} \begin{pmatrix} x''' \\ y''' \\ z''' \end{pmatrix} . \tag{3.20}$$

The arrival angle, η, is defined as the angle from the Ecliptic North Pole to the SN source. In the interstellar frame, the particles travel along the $-\hat{z}''''$-direction, or: $\vec{\mathbb{F}}(t) = -\mathbb{F}(t)\hat{z}''''$. We also define spherical coordinates in the interstellar frame so that:

$$\begin{pmatrix} x'''' \\ y'''' \\ z'''' \end{pmatrix} = \begin{pmatrix} r'''' \sin\theta'''' \cos\phi'''' \\ r'''' \sin\theta'''' \sin\phi'''' \\ r'''' \cos\theta'''' \end{pmatrix} . \tag{3.21}$$

Combining the transformations we have:

$$\begin{aligned} \begin{pmatrix} x'''' \\ y'''' \\ z'''' \end{pmatrix} = & \begin{pmatrix} 1 & 0 & 0 \\ 0 & \cos\eta & -\sin\eta \\ 0 & \sin\eta & \cos\eta \end{pmatrix} \begin{pmatrix} \cos\chi t & \sin\chi t & 0 \\ -\sin\chi t & \cos\chi t & 0 \\ 0 & 0 & 1 \end{pmatrix} \begin{pmatrix} 1 & 0 & 0 \\ 0 & \cos\alpha & \sin\alpha \\ 0 & -\sin\alpha & \cos\alpha \end{pmatrix} \\ & \times \begin{pmatrix} \cos\omega t & -\sin\omega t & 0 \\ \sin\omega t & \cos\omega t & 0 \\ 0 & 0 & 1 \end{pmatrix} \begin{pmatrix} r\sin\theta\cos\phi \\ r\sin\theta\sin\phi \\ r\cos\theta \end{pmatrix} . \end{aligned} \tag{3.22}$$

With regards to the coordinate differentials, all of the coordinate transformations

are rotations, which means they are special affine transformations and therefore are area- and volume-preserving. More specifically, examining the terrestrial-to-rotating frame transformation, the differential volumes are:

$$dV = d\vec{z} \cdot (d\vec{x} \times d\vec{y}) = dx\ dy\ dz\,, \text{and } dV' = d\vec{z'} \cdot (d\vec{x'} \times d\vec{y'}) = dx'\ dy'\ dz'\,, \quad (3.23)$$

and the two sets of differentials are related according to Equation (3.17):

$$\begin{aligned} d\vec{x'} &= d\vec{x}\cos\omega t - d\vec{y}\sin\omega t \\ d\vec{y'} &= d\vec{x}\sin\omega t + d\vec{y}\cos\omega t \\ d\vec{z'} &= d\vec{z}\,. \end{aligned} \quad (3.24)$$

Combining Equations (3.23) and (3.24), we get:

$$\begin{aligned} dV' &= d\vec{z'} \cdot (d\vec{x'} \times d\vec{y'}) \\ &= d\vec{z} \cdot [(d\vec{x}\cos\omega t - d\vec{y}\sin\omega t) \times (d\vec{x}\sin\omega t + d\vec{y}\cos\omega t)] \\ &= d\vec{z} \cdot \left[\left(\cos^2\omega t + \sin^2\omega t\right) d\vec{x} \times d\vec{y}\right] \\ &= d\vec{z} \cdot [(1)\, d\vec{x} \times d\vec{y}] = d\vec{z} \cdot (d\vec{x} \times d\vec{y}) = dV \\ \Rightarrow dx'\ dy'\ dz' &= dx\ dy\ dz\,. \end{aligned} \quad (3.25)$$

Similar derivations can be done for the each of the other transformations, and we find:

$$\Rightarrow dx\ dy\ dz = dx''''\ dy''''\ dz'''' = r^2\sin\theta\ d\theta\ d\phi\ dr = (r'''')^2\sin\theta''''\ d\theta''''\ d\phi''''\ dr''''\,. \quad (3.26)$$

Because there is no variation in radius, $\sin\theta\ d\theta\ d\phi = \sin\theta''''\ d\theta''''\ d\phi'''' \Rightarrow d\Omega = d\Omega''''$, and $d\vec{\Omega}$ is directed away from Earth's center. To calculate the fluence, $\mathcal{F}$, received by

a sector of Earth, we integrate over the area of the sector:

$$dN = \vec{\mathbb{F}}(t) \cdot d\vec{A}\ dt \Rightarrow \frac{dN}{A} = \frac{\vec{\mathbb{F}}(t) \cdot d\vec{A}\ dt}{A}, d\vec{A} = r^2 d\vec{\Omega} \tag{3.27}$$

$$\Rightarrow d\mathcal{F} = \frac{\vec{\mathbb{F}}(t) \cdot r^2 d\vec{\Omega}\ dt}{r^2 \Omega} = \frac{\vec{\mathbb{F}}(t) \cdot d\vec{\Omega}\ dt}{\Omega} \tag{3.28}$$

$$\Rightarrow \mathcal{F} = \frac{\iiint \vec{\mathbb{F}}(t) \cdot d\vec{\Omega}\ dt}{\Omega}, \mathbb{F}(t) = \mathbb{F}_0 \left(1 - \frac{t}{\Delta t_{\text{signal}}}\right). \tag{3.29}$$

In the interstellar frame, θ'''' and ϕ'''' do not depend on time, t:

$$\mathcal{F} = \frac{\iiint \vec{\mathbb{F}}(t) \cdot d\vec{\Omega}'''' dt}{\Omega} = \frac{1}{\Omega} \iiint -\mathbb{F}(t) \cos(\pi - \theta'''')\, d\Omega'''' dt = \frac{1}{\Omega} \iiint \mathbb{F}(t) \cos\theta'''' d\Omega'''' dt \tag{3.30}$$

$$\Rightarrow \mathcal{F} = \frac{1}{\Omega} \int_{t_{\text{ini}}}^{t_{\text{fin}}} \mathbb{F}(t) dt \iint_S \cos\theta'''' \sin\theta'''' d\theta'''' d\phi'''' \tag{3.31}$$

The first integral is straightforward:

$$\int_{t_{\text{ini}}}^{t_{\text{fin}}} \mathbb{F}(t) dt = \mathbb{F}_0 \left[t - \frac{t^2}{2\Delta t_{\text{signal}}}\right]_{t_{\text{ini}}}^{t_{\text{fin}}} = \mathbb{F}_0 \left(\frac{t_{\text{ini}}^2 - t_{\text{fin}}^2}{2\Delta t_{\text{signal}}} + t_{\text{fin}} - t_{\text{ini}}\right), \tag{3.32}$$

and the second integral is the projected area of a spherical sector onto the $x'''' - y''''$-plane, see Figure 3.8.

Because the SN dust particles are traveling in the $-\hat{z}''''$-direction by construction, the surface integral in Equation (3.31) represents the area of the sector projected onto the $x'''' - y''''$-plane (see Figure 3.8). While it is fairly straightforward to transform the sector vertices from the terrestrial to the interstellar frame (e.g., $\theta_u \rightarrow \theta_u''''$, etc.) the path from each vertex is not, requiring a dependence on ϕ'''' in the limits of integration for θ'''' (or vice versa):

$$\iint_S \cos\theta'''' \sin\theta'''' d\theta'''' d\phi'''' = \int_{\phi_l''''}^{\phi_u''''} \int_{g(\phi'''')}^{f(\phi'''')} \cos\theta'''' \sin\theta'''' d\theta'''' d\phi'''', \tag{3.33}$$

where f and g are the transformed paths between vertices. In order to simplify our calculations, rather than derive the transformation functions, we approximate the area of the projection (and the integral) as a general quadrilateral (or triangle in the case where $\theta_l = 0°$ or $\theta_u = 180°$). In other words:

$$\iint_S \cos\theta'''' \sin\theta'''' d\theta'''' d\phi'''' \approx \begin{cases} \sqrt{s(s-a)(s-b)(s-c)} & \theta_l = 0 \text{ or } \theta_u = \pi\,, \\ \frac{1}{4}\sqrt{4\ p^2\ q^2 - \left(b^2+d^2-a^2-c^2\right)^2} & \text{otherwise}\,, \end{cases} \tag{3.34}$$

where a, b, c and d are the lengths of each side, p and q are the lengths of the diagonals of the quadrilateral, and s is the semi-perimeter of the triangle ($s \equiv (a+b+c)/2$).

For a given latitude and longitude (θ, ϕ) and gridsize $(\Delta\theta \times \Delta\phi)$, these correspond to grid boundaries at: $\theta_l = \theta - \Delta\theta/2$, $\theta_u = \theta + \Delta\theta/2$, $\phi_l = \phi - \Delta\phi/2$, and $\phi_u = \phi + \Delta\phi/2$. Using Equation (3.22) and setting $r = 1\ R_\oplus$, we transform the grid vertices to their associated (x'''', y'''', z'''') coordinates. The distances between the $(x'''', y'''', 0)$ coordinates are used to find the associated a, b, c, d, p, and q values. For our particular approach, the vertices correspond to:

$$\begin{aligned} a &\mathrel{\widehat{=}} \overline{(\phi_l, \theta_l)\,(\phi_u, \theta_l)} & b &\mathrel{\widehat{=}} \overline{(\phi_u, \theta_l)\,(\phi_u, \theta_u)} & c &\mathrel{\widehat{=}} \overline{(\phi_u, \theta_u)\,(\phi_l, \theta_u)} \\ d &\mathrel{\widehat{=}} \overline{(\phi_l, \theta_u)\,(\phi_l, \theta_l)} & p &\mathrel{\widehat{=}} \overline{(\phi_u, \theta_l)\,(\phi_l, \theta_u)} & q &\mathrel{\widehat{=}} \overline{(\phi_l, \theta_l)\,(\phi_u, \theta_u)}\,. \end{aligned} \tag{3.35}$$

If any of the z'''' values for the vertices are negative, corresponding to the sector being on the opposite side of the Earth from the arriving flux, the area of the sector is zero. This increases the error in our approximation along the edges, but our time intervals are such that the errors are consistent across the entire surface, and we are interested in the relative values across the globe.

Finally, to calculate the fluences for each of the sectors (for $\Delta\theta = \Delta\phi = 10°$ there are 648 sectors), we calculate the fluence received at each time step on each sector

then sum over all time steps for each sector (presumably the time steps cover the entire duration of the SN signal, although after one precessional cycle the final pattern changes very little). We use Equation (3.32) to find the fluence incident to the sector during that time step (given by Equations (3.12) and (3.13)), and we use Equation (3.34) to find the cross-sectional area facing the incident SN dust flux. The product of these two values gives the sector fluence at each time step. Once the sector fluence has been summed over all time steps (the result of Equation (3.31)), the value of ψ for each sector is found by scaling the total sector fluence by the total area-weighted average fluence of the entire sphere. For our chosen grid size of $\Delta\theta = \Delta\phi = 10°$, this approximation is accurate to $\lesssim 1\%$, and for our results in Figures 3.3 and 3.5, this approximation demonstrated convergence to the precision given.

3.8 Heliosphere IMF Model

We use the model outlined in Parker (1958) and Gustafson (1994). Using a right-handed, spherical coordinate system with the Sun at the origin, we define ϕ as the azimuthal angle along the Sun's equator and θ as the angle from the Sun's rotational axis. Because of the Sun's rotation and a magnetic field frozen-in the radially expanding solar wind, the components of the IMF take the form:

$$B_r = B_{r,0} \left(\frac{r_0}{r}\right)^2 \text{sgn}\left(\pi/2 - \theta\right) \,, \tag{3.36}$$

$$B_\theta = 0 \,, \tag{3.37}$$

$$B_\phi = B_{\phi,0} \left(\frac{r_0}{r}\right) \sin\theta \ \text{sgn}\left(\pi/2 - \theta\right) \,, \tag{3.38}$$

where $B_{r,0}$ and $B_{\phi,0}$ are the magnetic field components at r_0 and $\text{sgn}\left(\pi/2 - \theta\right)$ accounts for the different polarities in the northern and southern solar hemispheres. From Gustafson (1994), for $r_0 = 1$ AU, $B_{r,0} \approx B_{\phi,0} \approx 30$ μG.

3.9 Earth's Magnetosphere Model

The Katsiaris & Psillakis (1987) Magnetosphere model defines its right-handed axes with the origin at the Earth, the $\hat{X}$-axis towards the Sun, the $\hat{Z}$-axis through the geographic North, and takes the form:

$$\vec{B} = \vec{B}_{\text{dipole}} + \vec{B}_{\text{tail}}\,, \tag{3.39}$$

with:

$$\vec{B}_{\text{dipole}} = -\frac{3MZX}{R^5}\hat{X} - \frac{3MZY}{R^5}\hat{Y} + \left(\frac{M}{R_3} - \frac{3MZ^2}{R^5}\right)\hat{Z}\,, \tag{3.40}$$

$$\vec{B}_{\text{tail}} = \left(B_{X0}\tanh\left(Z/H\right)\right)\hat{X} - B_{Z0}\hat{Z}\,, \tag{3.41}$$

and

$$R^2 = X^2 + Y^2 + Z^2\,, \tag{3.42}$$

where M is the magnetic dipole strength based on the surface value, and B_{Z0} is a uniform magnetic field normal to the dipole's equatorial plane.

Table 3.2: Maximum Trajectory Deflection for Various Grain Parameters

Grain Charge (V)	Speed (km s^{-1})	Grain Radius (μm)	β	IMF Deflection (°)	Magnetosphere Deflection (°)	Reaches Earth
5	40	0.2	0.8	0.5	0.04	Yes
0.5	40	0.2	0.8	0.3	0.005	Yes
50	40	0.2	0.8	5	0.4	Yes
5	40	0.02	0.1	3	5	Yes
5	40	2	0.1	0.3	0.02	Yes
5	20	0.2	0.8	0.9	0.07	No
5	80	0.2	0.8	0.4	0.02	Yes

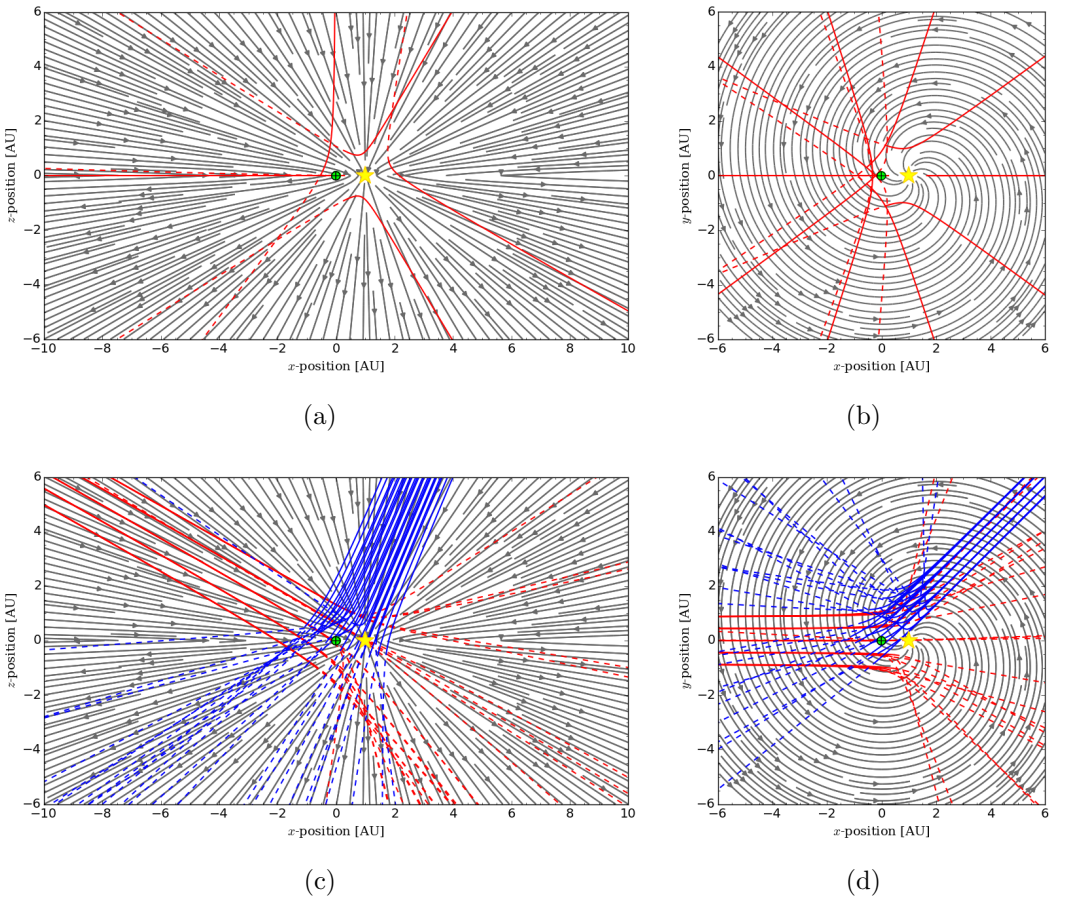

Figure 3.1: *Sample dust grain trajectories within the Heliosphere. The magnetic field lines are shown with grey arrows, the Sun is shown by a yellow star at* $(1, 0, 0)$ *AU, and the Earth is shown by a green* $\oplus$ *at the origin (NOTE: the Sun and Earth sizes are not to scale). Dust grain trajectories are shown in red or blue with the incoming trajectory indicated by solid lines, and, after closest approach to Earth, the outgoing trajectory is indicated by dashed lines. The initial dust grain parameters are:* $a = 0.2$ μm, $\mathcal{V} = 5$ V, *and* $v = 40$ $km\ s^{-1}$. *The upper panel shows individual dust grain trajectories initially aimed at Earth and how they behave in the inner Solar System. The lower panel shows a dust swarm with grains initially travelling parallel to each other, and grains not initially aimed at Earth can be deflected into it.*

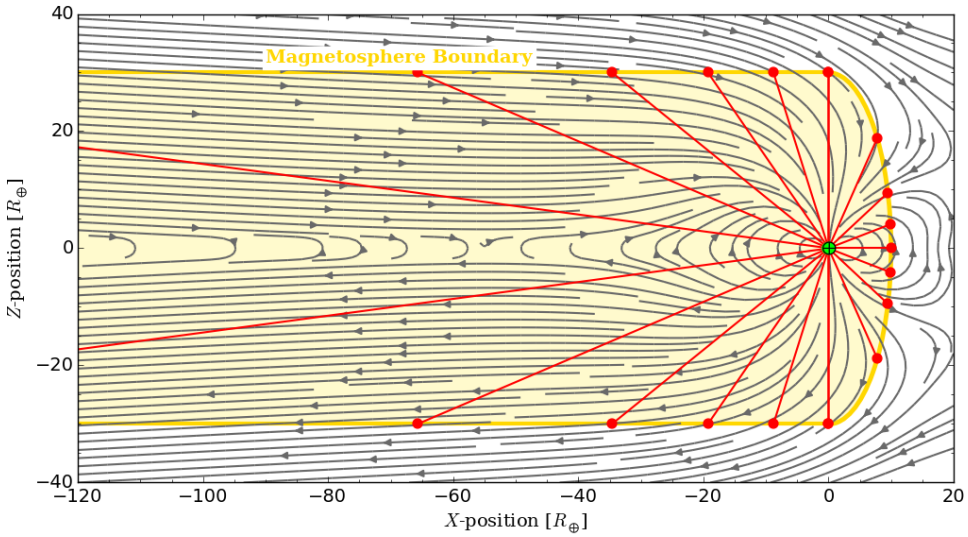

(a)

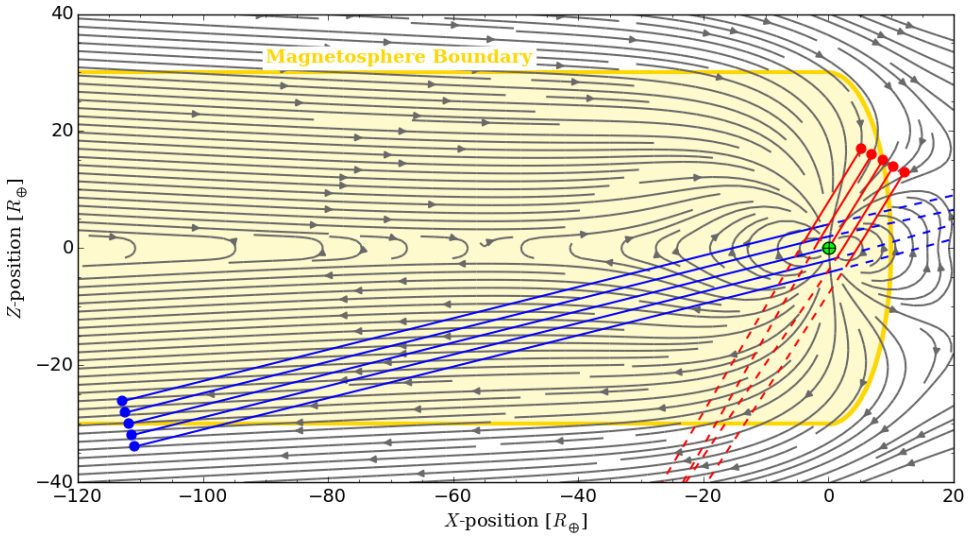

(b)

Figure 3.2: *Sample dust grain trajectories within the Magnetosphere. The magnetic field lines are shown with grey arrows, the Earth is shown (to scale) by a green* $\oplus$ *at the origin, and the boundary of the Magnetosphere is shown with a yellow line (NOTE: Magnetic field lines outside of the boundary were not used and can be ignored). Dust grain trajectories are shown in red or blue with the initial locations indicated by dots, the incoming trajectory indicated by solid lines, and, after closest approach to Earth, the outgoing trajectory is indicated by dashed lines. The initial dust grain parameters are:* $a = 0.2\ \mu m$, $\mathcal{V} = 5\ V$, *and* $v = 40\ km\ s^{-1}$. *The left panel shows that individual dust grain trajectories initially aimed at Earth experience little deflection and impact Earth. The right panel shows a dust swarm with grains initially traveling parallel to each other remain parallel until after passing Earth.*

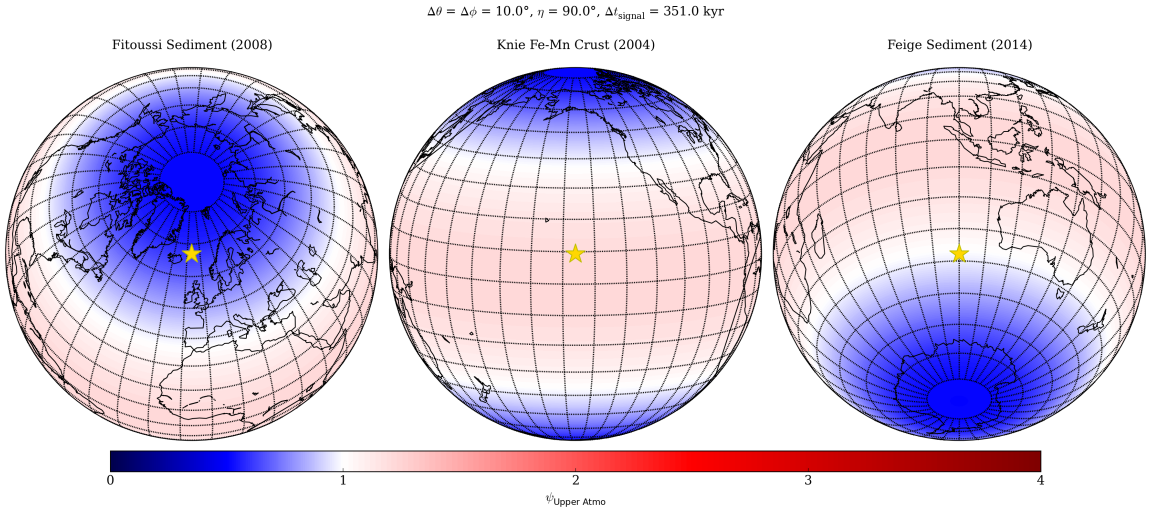

(a)

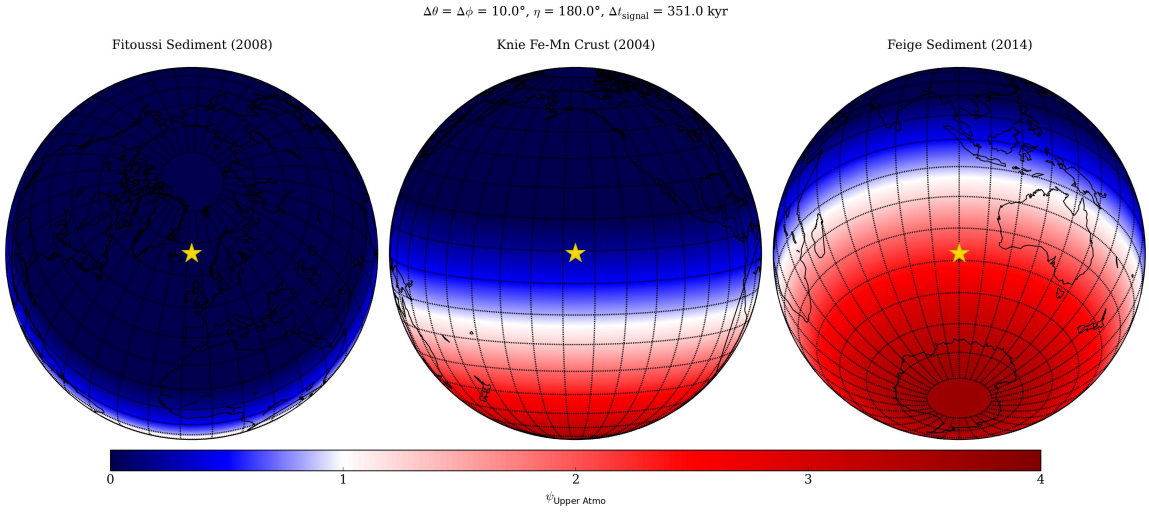

(b)

Figure 3.3: *Sample values of the distribution factor, ψ, as a function of the arrival angle, η at the top of the atmosphere. As η increases from $\eta = 0°$, the distribution changes from a northern concentration to an equatorial concentration at $\eta = 90°$. The sampling locations are shown as yellow stars in the centers of the figures. Note that, regardless of the value of η, the equator always receives some flux. It should be noted that the plotting program used to make these figures automatically smooths the transition from grid to grid, making the figures appear of higher resolution than actually calculated. However, based on the latitudinally-averaged values, the grid-to-grid transitions are, in fact, smooth, and the appearance shown in the figure is accurate.*

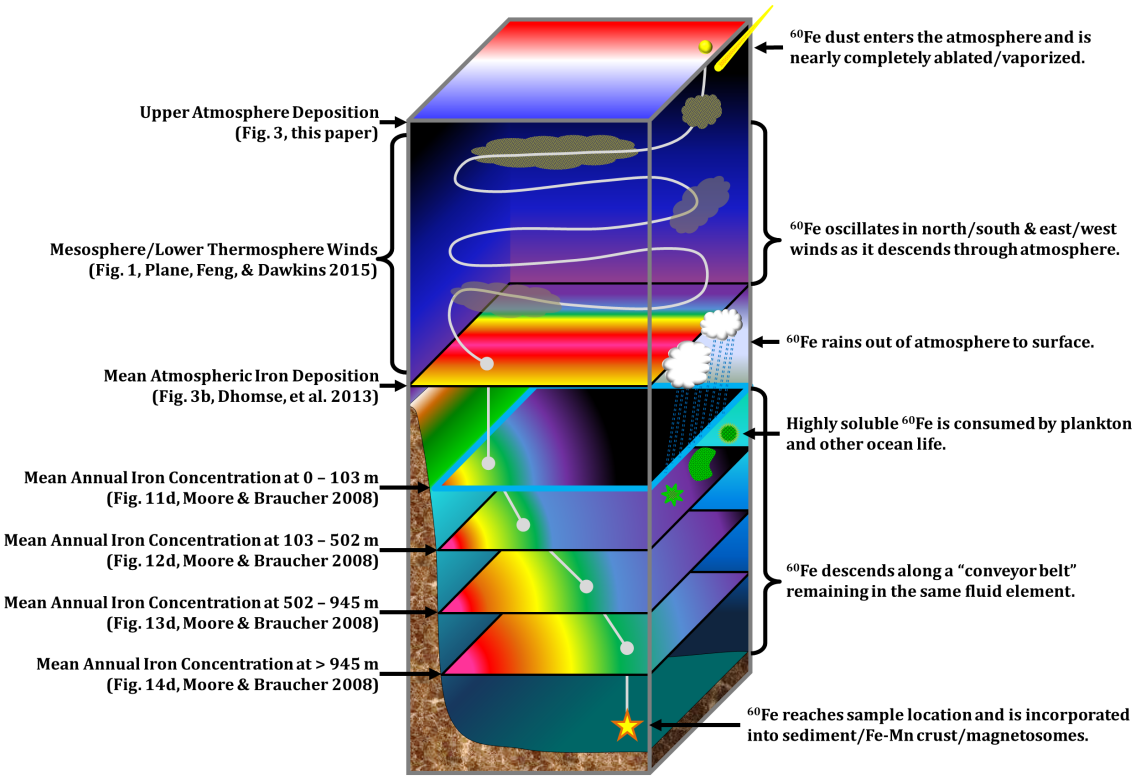

Figure 3.4: *Schematic of* ^{60}Fe *passage through the atmosphere to the ocean floor. This diagram summarizes the processes and assumptions outlined in §3.4.2-3.4.4. On the left side of the diagram, the relevant references used in tracking the* ^{60}Fe *material's passage are given, and on the right side, the main processes acting on the* ^{60}Fe *material are described. Color gradients indicate concentration gradients of iron and mimic those found in the source figures referenced at left. For this schematic, the colors of the gradients do not have specific values associated with them, but show how the referenced figures relate to one another. A SN dust grain containing* ^{60}Fe *enters at the top of the schematic, is vaporized, and the* ^{60}Fe *vapor descends through the atmosphere until it is rained out to the surface. This surface location is given in Fig. 3b, Dhomse et al. (2013), and the* ^{60}Fe *material will enter the ocean fluid element at the corresponding location in Fig. 11d, Moore & Braucher (2008); in this schematic, the fluid element has a "green" concentration. The* ^{60}Fe *remains in this "green" fluid element as it descends; the location of the "green" fluid element in Fig. 14d, Moore & Braucher (2008) will correspond to the sampling location on the ocean floor. To determine the amount of wind and water deflection, we follow the* ^{60}Fe *material's path backwards from the sampling location, along the fluid element with the associated iron concentration to the surface, and to the accompanying location on Fig. 3b, Dhomse et al. (2013).*

Table 3.3: Summary of Dust Grain Transit Through Solar System to Ocean Floor

Region	Primary Influences	Residence Time	Characteristic Region Boundary*
Interplanetary	IMF, Solar Radiation/Gravity	$\sim 10 - 12$ years	$100 - 150$ AU
Magnetosphere	Terrestrial Magnetic Field	$\lesssim 2$ days	$10 - 1000\ R_{\oplus}$
Upper Atmosphere (MLT)	Collisional Drag/Ablation & Strong Winds	$4 - 6$ years	$90 - 115$ km
Troposphere	Rain, Wind	$1 - 2$ weeks	~ 10 km
Surface:			
- Land	Transplantation by Surface Winds	indefinite	$\sim$ km
- Water	Biological Uptake, Ocean Currents	$100 - 200$ years	~ 4 km
Ocean Floor	Biological Transplantation/Disturbance	indefinite	$\sim$ m

* - *Boundary distances are measured from Earth's surface except for the Water and Ocean Floor regions which are measured from the ocean floor.*

Table 3.4: Predicted Fluence Ratios for Uptake Values

$\psi_{\rm Knie} = 0.43$, $\psi_{\rm Fitoussi} = 0.14$, $\psi_{\rm Feige} = 1.4$				
Fluence Ratios	Observed	High Uptake	Medium Uptake	Low Uptake
$\mathcal{F}_{\rm Fitoussi}/\mathcal{F}_{\rm Knie} =$	$0.\ (< 70.9)$	0.33	0.65	3.3
$\mathcal{F}_{\rm Fitoussi}/\mathcal{F}_{\rm Feige} =$	$0.\ (< 7.04)$	0.11	0.11	0.11
$\mathcal{F}_{\rm Feige}/\mathcal{F}_{\rm Knie} =$	$10. \pm 6$	3.3	6.5	33

Table 3.5: Implied Source Distances for Each Uptake Case

Case	High	Medium	Low
$\psi_{\rm Knie} = 0.43$	$U_{\rm crust} = 1.0$	$U_{\rm crust} = 0.5$	$U_{\rm crust} = 0.1$
$8 - 10$-$M_\odot$ ECSN	45^{+10}_{-6} pc	46^{+10}_{-6} pc	35^{+8}_{-5} pc
15-$M_\odot$ CCSN	61^{+14}_{-8} pc	64^{+14}_{-8} pc	47^{+11}_{-6} pc
9-$M_\odot$ SAGB	82^{+13}_{-8} pc	84^{+13}_{-8} pc	67^{+11}_{-7} pc

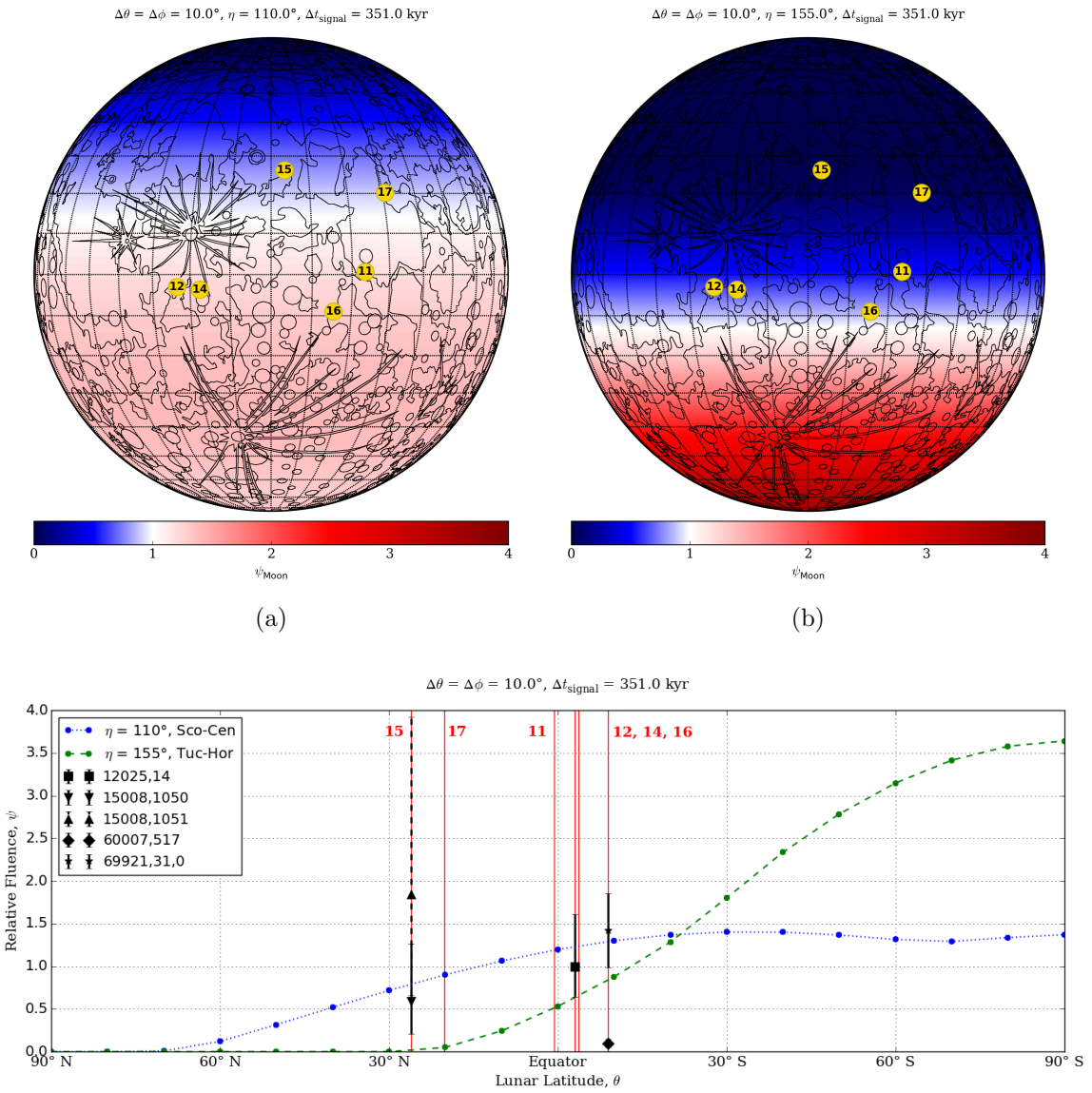

Figure 3.5: *Sample predicted values for the lunar distribution factor, ψ_{Moon}. For SN material arriving from $\eta = 110°$, corresponding to a SN in the Sco-Cen region (top, left panel), and $\eta = 155°$, corresponding to a SN in the Tuc-Hor region (top, right panel). Apollo landing sites are highlighted by the numbered, yellow circles in the upper panels and vertical, red lines in the lower panel (Davies et al., 1987; Davies & Colvin, 2000). The Fimiani et al. (2016) measurements are shown in black; of note are the large error ranges particularly for the 15008 samples. Like Figure 3.3, the plotting program smooths grid-to-grid, however, the lower panel shows the latitudinally-averaged relative fluences for the top panels. The actual model averages are shown with data points, and the connecting lines show a smooth, nearly sine-function profile. The lunar background diagram used with permission from Steven Dutch, University of Wisconsin at Green Bay.*

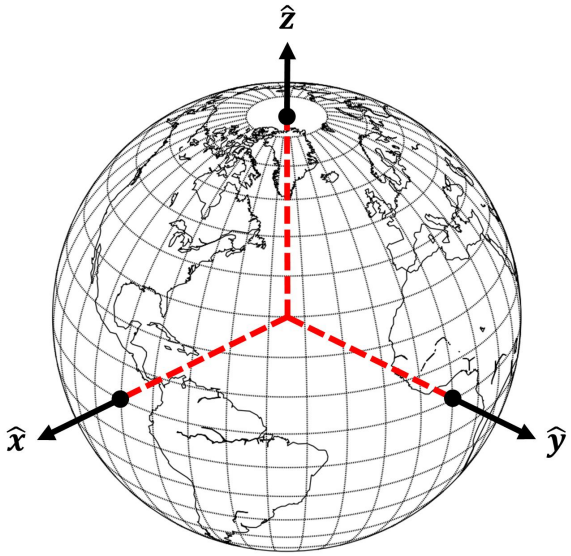

Figure 3.6: *Definition of terrestrial axes used in §3.4.2. The $+x$-axis passes through the equator at the 90° W-meridian, the $+y$-axis passes through the equator at the 0° meridian, and the $+z$-axis passes through the geographic North Pole.*

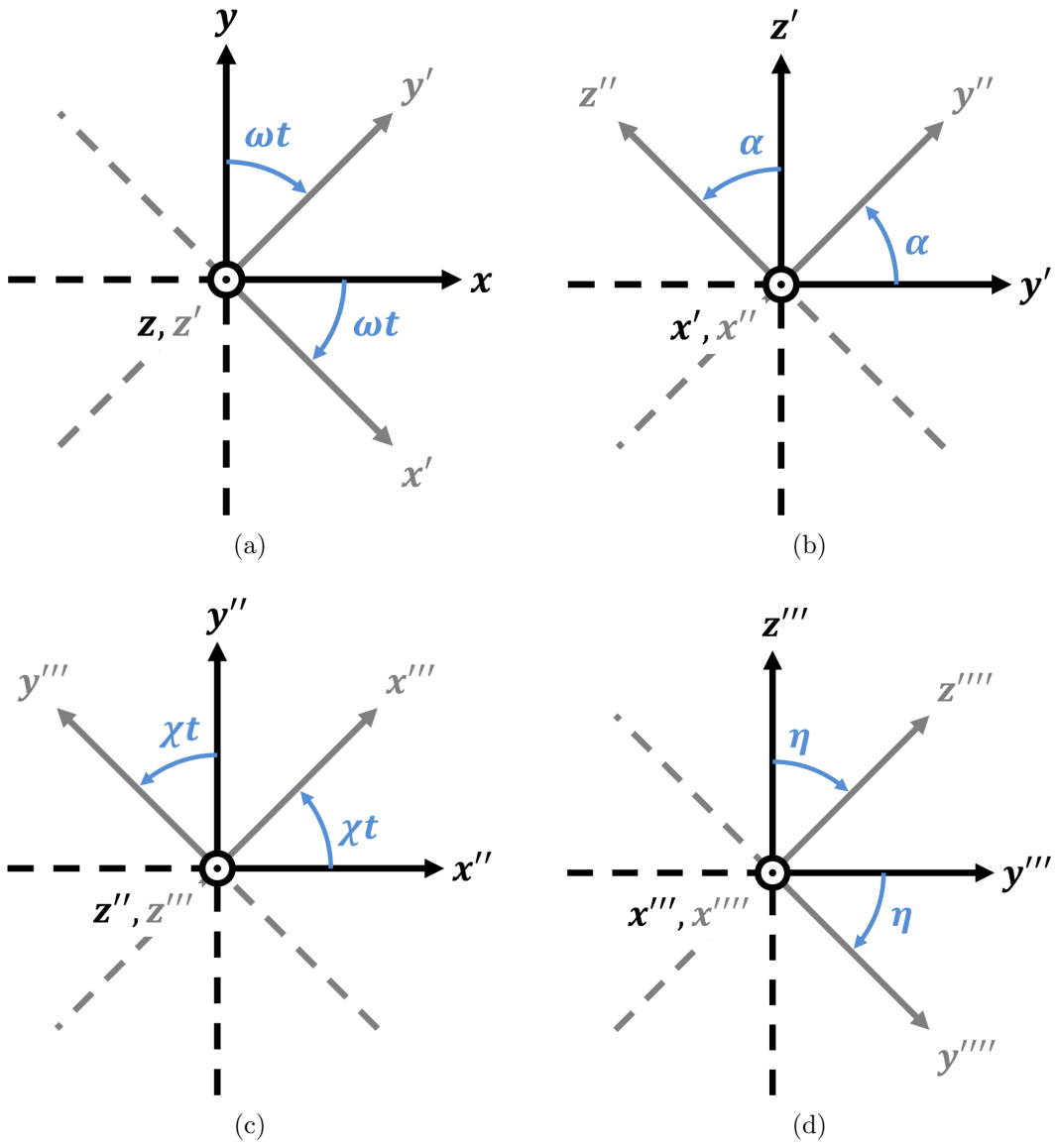

Figure 3.7: *Coordinate Transformations: (a) Terrestrial (unprimed) to Daily Rotation (′), (b) Daily Rotation (′) to Inclination (″), (c) Inclination (″) to Precessing/Ecliptic (‴), (d) Precessing/Ecliptic (‴) to Shock Wave/Interstellar (⁗).*

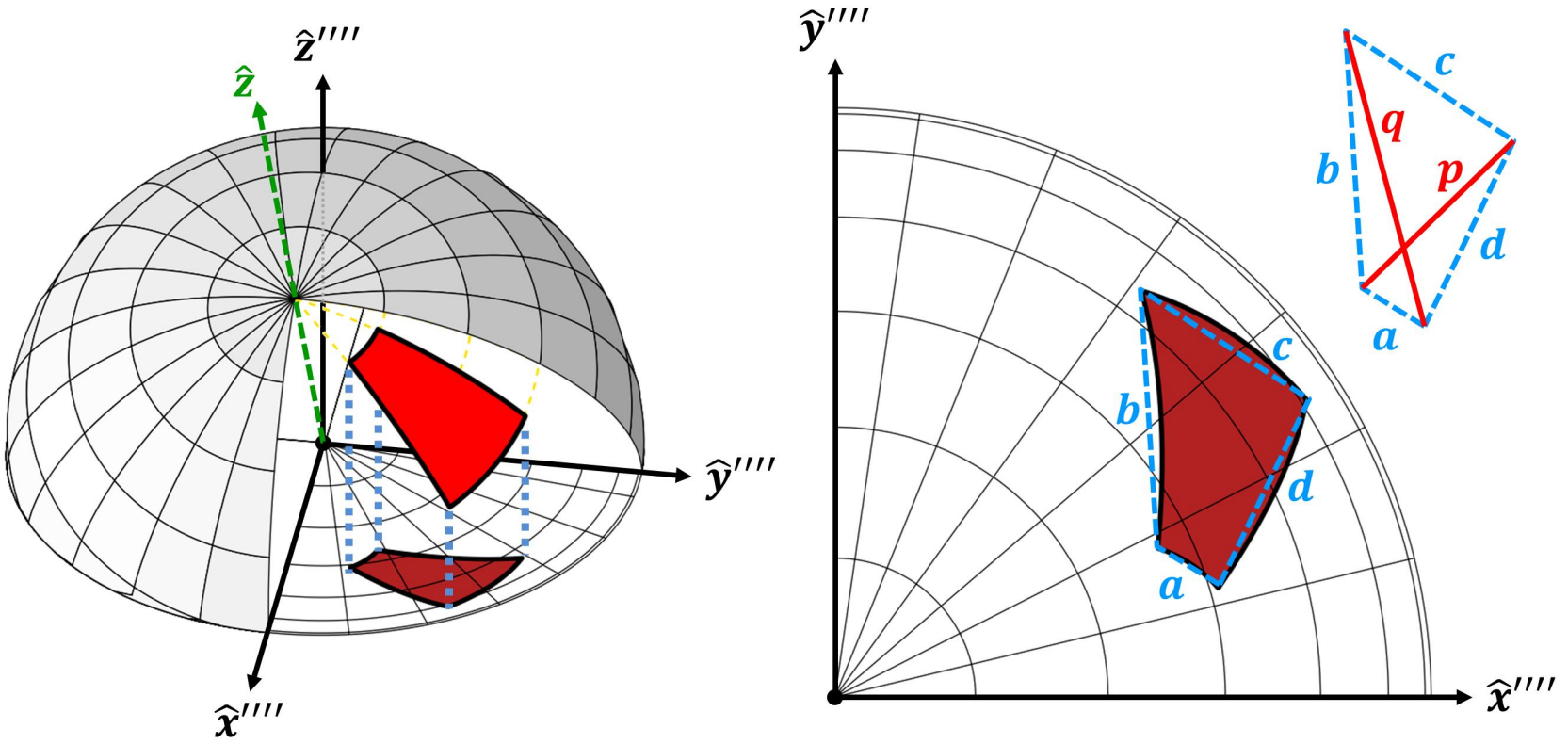

Figure 3.8: *Sector area approximation. The area of the projection of the sector onto the $x'''' - y''''$-plane is approximated using Bretschneider's Formula for 4-sided sectors and Heron's Formula for 3-sided sectors.*

Chapter 4

No Escape from the Supernova! Dust Transport Through a Supernova Remnant

This chapter is in preparation for submission to the The Astrophysical Journal under the authorship Fry, B., Fields, B., & Ellis, J. and contains preliminary results.

4.1 Introduction

Supernovae (SNe) are both some of the most destructive and creative events in the universe. The explosion blasts apart a massive star, and its outward propagating shock wave shatters dust grains floating in the interstellar medium (ISM). However, the explosion also leads to the formation of a new compact object, creates heavy elements beyond iron and nickel, and as the SN remnant (SNR) expands, new dust grains condense from within the ejecta. This clash of simultaneously destroying and creating dust begs the question of whether SN are net producers or demolishers of dust.

Looking at another facet of SNe: they occur at a rate of $1-3$ per century within the Milky Way (e.g., Adams et al., 2013, and references therein), and given the finite size of the Milky Way, this suggests that one (probably more) has occurred close enough to have produced detectable effects on Earth. These effects could range from delivery of SN material to Earth's surface to biological impacts. Studies of biological impacts of a near-Earth SN has a long history in the literature (e.g., Shklovskij, 1969; Alvarez et al., 1980; Ellis & Schramm, 1995), but the delivery of SN material to Earth has only more recently been examined, first by (Ellis et al., 1996; Korschinek et al., 1996), which suggested looking for using long-lived radioactive isotopes ($\tau_{1/2} \sim$ Myr) such as ^{60}Fe and ^{244}Pu to find direct evidence of such an event since both isotopes are not manufactured within the Solar System and any pre-solar isotopes will have decayed by today.

The first evidence for extra-solar radioisotopes was found by Knie et al. (1999) after examining a sample of ferro-manganese (Fe-Mn) crust from Mona Pihoa in the South Pacific. Knie et al. found an anomaly in ^{60}Fe concentration that suggested a SN occurred near Earth sometime within the last 5 Myr (a specific time could not be determined). This study was later expanded by Knie et al. (2004) using a

different Fe-Mn crust sample from the equatorial Pacific Ocean floor, and found a distinct signal in ^{60}Fe abundance $\sim$ 2.2 Myr ago, with a ^{60}Fe fluence, $\mathcal{F}$, at the time of arrival calculated to have been $\mathcal{F}_{\rm Knie} = 1.41 \times 10^6$ atoms cm^{-2}. This detection was later confirmed by Fitoussi et al. (2008) in the Fe-Mn crust, but a corroborating signal in sea sediment samples from the northern Atlantic Ocean was not detected. Fitoussi et al. noted several reasons for the discrepancy, including variations in the background and differences in the uptake efficiencies between the Fe-Mn crust and sediment. Additionally, lunar regolith samples (Cook et al., 2009; Fimiani et al., 2012, 2014, 2016) have shown an excess of ^{60}Fe as well, although only the presence of a signal is detectable, not the precise arrival time or fluence (Feige et al., 2013) because of the nature of the regolith. Subsequently, results from Eltanin sediment samples from the southern Indian Ocean were reported in Feige (2014), confirming the Knie et al. (2004) Fe-Mn crust detection in these sea sediment samples and leading to an estimated arrival fluence of $\mathcal{F}_{\rm Feige} = (2.32 \pm 0.60) \times 10^7$ atoms cm^{-2}. Lastly, Wallner et al. (2016) found a larger fluence value, $\mathcal{F}_{\rm Wallner} = (3.5 \pm 0.2) \times 10^7$ atoms cm^{-2}. The study by Fry et al. (2016) found that terrestrial atmospheric and oceanic processes are likely the cause for the slight differences in the fluence values between these studies, including the lack of a detection in the Fitoussi et al. sediment sample.

The source of the ^{60}Fe material has been examined in several papers; Benítez et al. (2002) suggested that the source event for the ^{60}Fe occurred in the Sco-Cen OB association. This association was $\sim$130 pc away at the time of the ^{60}Fe-producing event, and its members were described in detail by Fuchs et al. (2006). Breitschwerdt et al. (2012, 2016) modeled the formation of the Local Bubble and used hydrodynamic simulations to model SNe occurring within the Sco-Cen association and track the ^{60}Fe dust entrained within the blast. Fry et al. (2015) examined the possible progenitors of the ^{60}Fe (including neutron-star mergers, thermonuclear/Type IA SNe) and found an Electron-Capture SN (ECSN), with Zero-Age Main Sequence (ZAMS) mass $\approx$

$8-10\ M_{\odot}$ ("$\odot$" refers to the Sun), to be the most likely progenitor, but was not able to completely rule out a Super Asymptotic Giant Branch (SAGB) star with ZAMS mass $\approx 6.5-9\ M_{\odot}$ as a possible source. Subsequently, Mamajek (2016) suggested the Tuc-Hor group (which was within ∼60 pc of Earth at the time of the ^{60}Fe-producing event) could have provided an ECSN based on the masses of the current group members. Cosmic ray studies by Kachelrieß et al. (2015) and Savchenko et al. (2015) found a signature in the proton cosmic ray spectrum suggesting an injection of cosmic rays associated with a SN occurring ∼2 Myr ago, and the discovery of ^{60}Fe in cosmic rays by Binns et al. (2016), suggest a SN origin within the last ~ 2.6 Myr located $\lesssim 1$ kpc of Earth, based on the ^{60}Fe lifetime and cosmic ray diffusion. Lastly, Fry et al. (2016) postulated the use of lunar regolith samples as an "antenna" to find the direction to the source of the ^{60}Fe material.

With particular relevance to SN dust, Fields et al. (2008), using hydrodynamic models, showed that SN material would need to be in the form of dust in order to reach Earth's surface. The Solar Wind would push any gas phase SN elements away from Earth's orbit, and only SN dust material would have sufficient mass and velocity to reach Earth. Combining this to the broader nature of SN, how can a SN, that is quite proficient at destroying dust, effectively transport dust material across light-years of interstellar space to Solar System without destroying it?

A large number of studies have examined general dust processing (e.g., Dwek & Arendt, 1992; Draine, 2003, and references therein), and within a SNR in particular Nozawa et al. (2006, 2007); Kozasa et al. (2009). Several studies consider only one type of action such as formation (Cherchneff & Dwek, 2009, 2010; Cherchneff & Sarangi, 2011; Cherchneff, 2013; Dwek, 2016), or examine only one type of process such as charging (Lafon et al., 1981; Draine & Sutin, 1987; Barkan et al., 1994) or sputtering (Shull, 1977; Scalo et al., 1977; Tielens et al., 1987; Dwek et al., 1996; Jones et al., 1996; Janev et al., 2001). Other studies have focused on a specific event within the

grain's journey in the SNR like the passage of the reverse shock (Silvia et al., 2010, 2012; Biscaro & Cherchneff, 2016). More comprehensive studies such as Nozawa et al. (2006); Nath et al. (2008); Micelotta et al. (2016); Bocchio et al. (2016) follow the grains through the entire SNR, but do not include magnetic fields which could potentially trap the grains within the remnant. In relation to near-Earth SN, studies to-date (e.g., Fry et al., 2015, 2016; Breitschwerdt et al., 2016) have assumed the ^{60}Fe material will be coupled to the SNR gas, and most likely confined to the leading edge of the SNR. This paper relaxes this assumption, allowing the grains to decouple from the SNR gas earlier in the SNR evolution, potentially escaping the SNR. Additionally, we include the most relevant dust processes (drag, erosion, and charging) with a rudimentary treatment of the SNR's magnetic to potentially trap the dust grains with the SNR.

4.2 Motivation

Charged dust grains inside a magnetic field will spiral around magnetic fields lines (Northrop & Morfill, 1984). The radius of this spiraling, $r_{\rm gyro}$, is given by (Murray et al., 2004):

$$r_{\rm gyro} = 9.75{\times}10^{-4}\ {\rm pc} \left(\frac{\rho_{\rm gr}}{7.87\ {\rm g\ cm^{-3}}}\right) \left(\frac{172.5\ {\rm V}}{|U|}\right) \left(\frac{1\ \mu{\rm G}}{B}\right) \left(\frac{v_{\perp,{\rm gr}}}{175\ {\rm km\ s^{-1}}}\right) \left(\frac{a}{0.1\ \mu{\rm m}}\right)^2 \tag{4.1}$$

where $\vec{B}$ is the magnetic field and $\rho_{\rm gr}$ is the mass density, $\vec{v}_{\perp,{\rm gr}}$ is the velocity perpendicular to the magnetic field, a is the radius, and U is the potential of the grain. Additionally, the period of this spiraling can be determined:

$$\tau_{\rm gyro} = 34\ {\rm yr} \left(\frac{\rho_{\rm gr}}{7.87\ {\rm g\ cm^{-3}}}\right) \left(\frac{172.5\ {\rm V}}{U}\right) \left(\frac{1\ \mu{\rm G}}{B}\right) \left(\frac{a}{0.1\ \mu{\rm m}}\right)^2 \tag{4.2}$$

In the case of a magnetic field with varying magnitude, the spiraling dust grain will conserve adiabatic quantities (see e.g., §12.5 Jackson, 1998). Of particular interest for our purposes is the adiabatic invariant $p_\perp^2/B$, where $p_\perp$ is the momentum of the object perpendicular to the magnetic field such that $v^2 = v_\perp^2 + v_\parallel^2$. Since magnetic fields do not perform work on the grain, we know the speed of the grain at later times will be the same as when it entered the field, $v = v_0$. If the magnetic field increases with position, $B(r)$, then by the adiabatic invariance:

$$\Rightarrow \frac{v_\perp^2}{B(r)} = \frac{v_{\perp 0}^2}{B_0} \Rightarrow v_\parallel^2 = v_0^2 - v_\perp^2 \frac{B(z)}{B_0} \tag{4.3}$$

As the magnetic field increases, $v_\perp$ will increase, which means $v_\parallel$ will decrease in order to maintain the original speed of the grain. There will be a position, r_{bounce} where the right side of Equation 4.3 will be zero, and the grain's movement along the magnetic field lines will reverse direction. Essentially, the grain will "bounce" off of the stronger magnetic field (this is also referred to as a magnetic mirror in Jackson (1998)).

We can find a relation for the strength of the magnetic field in order to bounce a dust grain. At bounce ($B(r_{\text{bounce}}) \equiv B_{\text{bounce}}$):

$$v_0^2 = v_\perp^2 \frac{B_{\text{bounce}}}{B_0}\,, \tag{4.4}$$

and if we consider an average case ($v_\perp \sim v_\parallel$):

$$\langle v_\perp \rangle \sim \frac{\sqrt{2}}{2} v_0\,, \tag{4.5}$$

then magnetic field at bounce is:

$$\Rightarrow v_0^2 \approx \frac{1}{2} v_0^2 \frac{B_{\text{bounce}}}{B_0} \tag{4.6}$$

$$\Rightarrow B_{\rm bounce} \approx 2B_0\,. \tag{4.7}$$

If the magnetic field varies with some characteristic length scale, $\lambda_{\rm mag}$, then when $r_{\rm gyro} = \lambda_{\rm mag}$, the grain will be "captured" by the magnetic field. After capture, if the magnetic field strength doubles, the dust grain will be reflected. We will see this action is relevant when considering dust grains encountering shocked ISM material within a SNR.

4.3 Supernova Remnant Evolution

A SNR will transition through four main phases as it evolves (Ostriker & McKee, 1988; Padmanabhan, 2001; Draine, 2011; Janka et al., 2016). The first phase is Free Expansion (FE), and is characterized by a constant velocity after the explosion. The ejected material moves outward supersonically, and produces a shock wave in the surrounding, ambient material (hereafter referred to as the "forward shock"). The presence of an ambient medium causes the ejected material to slow down, but in the early phases of expansion when the mass of the ejected material far exceeds that of the swept up ambient material, this deceleration is negligible when examining the expansion of the forward shock. However, this slight deceleration creates a second shock wave (hereafter referred to as the "reverse shock" or RS), which communicates the presence of the ambient medium to the ejected material. Analytic solutions to this phase were found by Chevalier (1982); Chevalier et al. (1992) and Nadezhin (1985) (referred to as C-N); these self-similar solutions yield good descriptions for the position of the forward shock and incorporate the presence of a RS. In the FE phase, both the forward and reverse shocks are moving outward. There are, however, some difficulties in the C-N solutions; first, at the contact between the ejecta and ambient medium, the C-N density profile solutions produce either an infinity or null depending on the density profile of the ambient medium. Both cases are unphysical, and if we attempted

to examine dust dynamics in such a state, the grain would encounter an imaginary wall or vacuum. Additionally, the C-N solutions ignore the presence of Rayleigh-Taylor (R-T) instabilities along the RS. R-T instabilities drive the RS further inward (Blondin & Ellison, 2001; Blondin, 2001), and, when considering dust, the location of the RS is of extreme importance since its passage effectively halts the growth of dust grains within the ejecta.

As the forward shock sweeps up more material, the SNR transitions into the second phase, Energy/Adiabatic-Conserving. This phase is often called the Sedov-Taylor phase (S-T) after Sedov (1959) and Taylor (1950) who found self-similar descriptions to this phase's expansion. When the swept-up material is approximately equal in mass to the ejecta material, the RS will cease moving outward and be driven inward, deeper into the ejecta, eventually proceeding all the way to the center of the SNR. Studying dust dynamics during the S-T phase would be fairly straightforward since the gas density, velocity, and pressure within the SNR are described smoothly. However, because the dust grains are initially formed during the FE phase, a description that includes a transition from both phases is required. Truelove & McKee (1999) found analytic solutions for this transition, describing the position of the forward and reverse shocks through both phases, however, these do not include descriptions of the gas properties (except as initial conditions) needed to describe the grain dynamics as well as ignoring the effects of R-T instabilities along the RS.

As the SNR expands and cools, ions within the SNR will combine with electrons and radiate photons. As the SNR becomes radiative, the SNR will lose thermal pressure support and the expansion will be determined by the momentum within the shell (Blondin et al., 1998). This third phase is the Momentum-Conserving phase, with the SNR shell slowing as it collects more surrounding material (this phase is also referred to as the snowplow phase because of this accumulating action). The snowplow phase typically begins around 50,000 years after the SN, but since the typical grain lifetime

is around 100,000 years Draine (2011), a detailed examination of the grain properties at the end of the S-T phase will be needed first, since the dust could be severely (or, possibly, completely) ablated before reaching the snowplow phase.

Eventually the forward shock will slow to the sound speed of the ambient medium. At this point the SNR effectively stops expanding, and the SNR enters the Fade-away phase as the shock transitions into a sound wave into ambient medium. The SNR will eventually be dispersed through random processes in the ISM. Any dust grains that survive to this stage will behave the same as they would in the general ISM.

Before choosing and building our SNR environment, it would be beneficial to first mention the quantities of the SNR environment we require in order to accurately describe the dynamics of our dust grains. §4.5 will describe in much greater detail why these quantities are important. The density, velocity, and temperature (and how they evolve with time) within the SNR are required as these determine the drag experienced by the grains as well as the degree of erosion from the gas. The composition of the gas should also be detailed since larger ions such as O/Si/S in sufficient concentrations can enhance erosion beyond that of simply H/He. The grain's charge and the direction and strength of the SNR magnetic field are important since dust grains spiraling around magnetic field lines could potentially become trapped within the SNR. The charge is dependent on the material the dust grain which itself is dependent on where the dust is formed with the ejecta. Finally, the location of the dust grain's birthplace in the ejecta is important, since it also affects when it will encounter the RS.

4.4 Model Description

We need to relate the SNR's density, ρ, velocity, $\vec{v}$, pressure, P, temperature, T, and magnetic fields, $\vec{B}$, so the magnetohydrodynamic equations are the best starting point. Since we are dealing with a SN explosion, the thermal velocities between particles will

be small compared to the bulk velocity (meaning thermal conduction can be ignored), the plasma is collisionless (meaning resistivity and Ohmic heating due to electron-ion collisions can be ignored), and the ejecta velocity is radial and much greater than the escape velocity ($v_{\rm ej} \gg v_{\rm esc}$) for the central compact object (meaning Coriolis and gravitational effects can be ignored). Additionally, if we limit our examination to the early phases of the SNR expansion (FE and S-T phases), we can ignore radiative effects. This gives the Ideal MHD Equations (in Lagrangian form):

$$\frac{D\rho}{Dt} = -\rho \nabla \cdot \vec{v} \qquad \text{(Mass)} \tag{4.8}$$

$$\frac{D\vec{v}}{Dt} = -\frac{1}{\rho}\nabla P + \frac{1}{\rho}\vec{j} \times \vec{B} \qquad \text{(Momentum)} \tag{4.9}$$

$$\frac{DP}{Dt} = -\Gamma P \nabla \cdot \vec{v} \qquad \text{(Energy)} \tag{4.10}$$

$$\frac{D\vec{B}}{Dt} = \left(\vec{B} \cdot \nabla\right) \vec{v} - \vec{B}\left(\nabla \cdot \vec{v}\right) \qquad \text{(Induction)} \tag{4.11}$$

with $\frac{D}{Dt} = \frac{\partial}{\partial t} + \vec{v} \cdot \nabla$, $\vec{j} = \frac{1}{\mu_0}\nabla \times \vec{B}$, $\mu_0 = 4\pi/c^2$, and $\Gamma = 5/3$ for this work. Expanding the momentum equation (4.9):

$$\begin{aligned} \frac{D\vec{v}}{Dt} &= -\frac{1}{\rho}\nabla P + \frac{1}{\rho}\left(\frac{1}{\mu_0}\right)\nabla \times \vec{B} \times \vec{B} \\ &= -\frac{1}{\rho}\nabla P + \frac{1}{\rho\mu_0}\left(\left(\vec{B} \cdot \nabla\right)\vec{B} - \frac{1}{2}\nabla B^2\right) \end{aligned} \tag{4.12}$$

The first term, $\left(\vec{B} \cdot \nabla\right)\vec{B}$, represents magnetic tension ($\sim B^2/4\pi$) and the last term, $\frac{1}{2}\nabla B^2$, represents magnetic pressure ($\sim B^2/8\pi$). In a typical SN remnant during the FE and S-T phases, expanding at ~ 200 km s^{-1} with a peak density of $4m_H$ cm^{-3}, the ram pressure is $P_{\rm ram} = \rho v^2 \sim 10^{-9}$ dyne cm^{-2}. In contrast, the magnetic tension and pressure are much weaker, $P_{\rm mag} \sim 10^{-13}$ dyne cm^{-2}. Because of this, they can be

ignored, and Equations 4.8-4.10 simplify to:

$$\text{Basic Fluid Equations} \begin{cases} \dfrac{D\rho}{Dt} = -\rho \nabla \cdot \vec{v} \\ \dfrac{D\vec{v}}{Dt} = -\dfrac{1}{\rho} \nabla P \\ \dfrac{DP}{Dt} = -\Gamma P \nabla \cdot \vec{v} \end{cases} \tag{4.13}$$

These are the basic fluid equations, meaning that during the early stages of SNR evolution, the expansion can be determined without including the magnetic field influence.

4.4.1 Nucleosynthesis Products

Fry et al. (2015) determined that an ECSN to be the most likely source for the ^{60}Fe signal. This determination is based on the nucleosynthesis results in Wanajo et al. (2009, 2013, 2014), so we use the results of these nucleosynthesis simulations for several aspects of our model. First, the results of the nucleosynthesis simulations are the initial conditions for our hydrodynamics simulations. The nucleosynthesis results also describe the composition of the ejecta, allowing us to determine the type and concentration of elements interacting with the grains as they transit the SNR. Lastly, the nucleosynthesis result give the initial position of the radioisotopes within the ejecta. This allows us to determine the initial velocity and type of grains that will mostly likely be formed contained radioisotopes (Sarangi & Cherchneff, 2013, 2015; Biscaro & Cherchneff, 2014).

The progenitor is assumed to be an ECSN with a ZAMS mass of 8.8 $M_{\odot}$ with a 0.014 $M_{\odot}$ core that contains the SN synthesized products and a 1.249 $M_{\odot}$ envelope composed of 70% Hydrogen and 30% Helium (we assume large-scale convection that thoroughly mixes the envelope). This is similar to the treatment by Janka et al. (2008);

Hoffman et al. (2008). The envelope is assumed to be in hydrostatic equilibrium and a single isothermal sphere with a temperature of 3500 K and completely ionized ($\mu_{\rm envel} = 0.61$). The energy delivered as kinetic energy into the ejecta is $E_{\rm SN} = 1.5 \times 10^{50}$ erg (Wanajo et al., 2009).

4.4.2 Hydrodynamic Initial Conditions

The density, velocity, and pressure profiles are based on the results of the Wanajo et al. (2014) nucleosynthesis results, the expected configuration of an ECSN progenitor, and the properties of the Local Bubble at the time of the SN. The ejecta is divided into an inner core region and an outer shell region based on the Wanajo et al. (2014) results. The Wanajo et al. (2014) results contained values at different azimuths and radii, so we averaged the values across azimuths, and fit a power law profile to the density and velocity averages. A comparison of the averaged results and fits are shown in Figures 4.2(a) and 4.2(b); note that the core cutoff positions for density and velocity ($r_{\rm core,1}$ and $r_{\rm core,2}$ respectively) are slightly different in order to provide a better fit.

The progenitor of an ECSN is assumed to be a Super-AGB star (Smartt et al., 2009; Woosley & Heger, 2015) with an envelope that has been completely mixed due to its thermal-pulsing (TP-SAGB) phase (Herwig, 2005; Poelarends et al., 2008; Pumo et al., 2009; Pumo, 2010; Jones et al., 2016). This implies the progenitor will be a red super giant and have an extended, isothermal envelope. We chose an envelope temperature of 3500 K (the approximate surface temperature of Betelgeuse Freytag et al., 2002) with $\rho \propto r^{-2}$ and $v = 0$. The edge of the envelope, $r_{\rm envel}$ marks the edge of the progenitor, and we assume the presence of a pre-SN wind. Several studies have examined the winds and mass loss during the TP-SAGB phase (see e.g., Doherty et al., 2013, and references therein), and we assumed a mass loss of $\dot{M}_{\rm w} = 7 \times 10^{-5}\ M_{\odot}\ {\rm yr}^{-1}$ and a wind velocity of $v_{\rm w} = 10$ km s^{-1}.

The pre-SN stellar wind will extend until the ram pressure of the wind, $P_{\rm wind} =$

$\rho v_{\rm wind}^2$, equals the pressure of the ISM, $P_{\rm ISM}$ (Castor et al., 1975). Because the Local Bubble shows evidence of multiple SN, we assume the source of the ^{60}Fe signal to be the most recent SN and that SN would have occurred in region denser than currently observed in the Local Cloud but depleted compared to the Average ISM. Because of this, we assumed ISM values of the Local Cloud ($n_{\rm ISM} = 0.1$ cm^{-3}, $P_{\rm ISM} = 2.2 \times 10^{-13}$ dyn cm^{-2}).

Combining these parameters, we assume the following initial conditions for our hydrodynamic simulations:

$$\rho(r) = \begin{cases} \rho_{\rm core}(r) & r_{\rm cutoff} \leq r < r_{\rm core1} \\ \rho_{\rm shell}(r) & r_{\rm core1} \leq r < r_{\rm shell} \\ \rho_{\rm envel}(r) & r_{\rm shell} \leq r < r_{\rm envel} \\ \rho_{\rm wind}(r) & r_{\rm envel} \leq r < r_{\rm wind} \\ \rho_{\rm ISM} & r_{\rm wind} \leq r \end{cases} \tag{4.14}$$

where

$$\begin{aligned} \rho_{\rm core}(r) &= 1.51 \times 10^5 \text{ g cm}^{-3} \left(\frac{r}{9.52 \times 10^7 \text{ cm}} \right)^{-5/4} \\ \rho_{\rm shell}(r) &= 1.75 \text{ g cm}^{-3} \left(\frac{r}{1.46 \times 10^9 \text{ cm}} \right)^{-10} \\ \rho_{\rm envel}(r) &= 743.67 \text{ g cm}^{-3} \left(\frac{r}{7.68 \times 10^8 \text{ cm}} \right)^{-2} \\ \rho_{\rm wind}(r) &= \frac{\dot{M}_{\rm w}}{4\pi v_{\rm w} r^2} \\ \rho_{\rm ISM} &= \mu m_H n_{\rm ISM} \end{aligned} \tag{4.15}$$

and

$$
\begin{aligned}
r_{\text{cutoff}} &= 9.52 \times 10^{7}\ \text{cm} \\
r_{\text{core,1}} &= 2.52 \times 10^{8}\ \text{cm} \\
r_{\text{shell}} &= 8.01 \times 10^{8}\ \text{cm} \\
r_{\text{envel}} &= 4.51 \times 10^{11}\ \text{cm} \\
r_{\text{wind}} &= 3.99 \times 10^{19}\ \text{cm}
\end{aligned}
\tag{4.16}
$$

$$
v(r) = \begin{cases}
v_{\text{core}}(r) & r_{\text{cutoff}} \leq r < r_{\text{core2}} \\
v_{\text{shell}}(r) & r_{\text{core2}} \leq r < r_{\text{shell}} \\
v_{\text{envel}}(r) & r_{\text{shell}} \leq r < r_{\text{envel}} \\
v_{\text{wind}} & r_{\text{envel}} \leq r < r_{\text{wind}} \\
v_{\text{ISM}} & r_{\text{wind}} \leq r
\end{cases}
\tag{4.17}
$$

where

$$
\begin{aligned}
v_{\text{core}}(r) &= 1.81 \times 10^{9}\ \text{cm s}^{-1} \\
v_{\text{shell}}(r) &= 1.81 \times 10^{9}\ \text{cm s}^{-1} \left(\frac{r}{2.52 \times 10^{8}\ \text{cm}} \right)^{-10} \\
v_{\text{envel}}(r) &= 0\ \text{cm s}^{-1} \\
v_{\text{wind}}(r) &= 10\ \text{km s}^{-1} \\
v_{\text{ISM}} &= 0\ \text{cm s}^{-1}
\end{aligned}
\tag{4.18}
$$

and $r_{\rm core,2} = 5.88 \times 10^8$ cm.

$$P(r) = \begin{cases} P_{\rm core}(r) & r_{\rm cutoff} \leq r < r_{\rm core1} \\ P_{\rm shell}(r) & r_{\rm core1} \leq r < r_{\rm shell} \\ P_{\rm envel}(r) & r_{\rm shell} \leq r < r_{\rm envel} \\ P_{\rm wind}(r) & r_{\rm envel} \leq r < r_{\rm wind} \\ P_{\rm ISM} & r_{\rm wind} \leq r \end{cases} \tag{4.19}$$

$$\begin{aligned} P_{\rm core}(r) &= \rho(r) v(r)^2 \\ P_{\rm shell}(r) &= \rho(r) v(r)^2 \\ P_{\rm envel}(r) &= \frac{\rho(r) k_B T_{\rm envel}}{\mu_{\rm envel} m_H} \\ P_{\rm wind}(r) &= \rho(r) v(r)^2 \\ P_{\rm ISM} &= P_{\rm ISM} \end{aligned} \tag{4.20}$$

4.4.3 Magnetic Field

We divide the magnetic field of our simulation into three regions: the star/ejecta field, the stellar wind field, and the ISM field. In terms of the ejecta field, we expect a surface field $B \sim 1$ G (this is the average surface field for Betelgeuse, which is similar in mass to our expected progenitor Petit et al., 2013). From Padmanabhan (2001), $B \approx B_0 \left(r_0/r\right)^2$, and if we estimate the dust will decouple from the plasma at ~ 1 pc (a *very* rough estimate) then the stellar field will have weakened to: $B \sim 10^{-8}$ μG. Furthermore, because the stellar wind magnetic field is the surface field stretched

even further due to flux freezing within the pre-SN wind, we expect the stellar wind magnetic field to be weak as well. With reasoning, we set $B_{\rm star} = B_{\rm wind} = 0$.

For the ISM magnetic field, because we focus our examination within the Local Bubble, the site of multiple SN, we will assume the initial magnetic field to be non-uniform and weakened compared to the average ISM (~ 3.57 μG). Using Padmanabhan (2001) again, and the fact that $\rho \propto r^{-3}$:

$$\Rightarrow B \approx B_0 \left(\frac{\rho}{\rho_0}\right)^{2/3}, \tag{4.21}$$

so our initial magnetic field will have an average magnitude of $B_{\rm ini} \approx 0.77$ μG. Because the initial field will be non-uniform, we establish a grid of random values with a spacing of either $\lambda_{\rm mag} \sim 6$ pc or $\lambda_{\rm mag} \sim 0.1$ pc (a typical length scale for density fluctuations in the ISM, Balsara et al., 2001; Inoue et al., 2009, respectively). These random values give a uniform distribution in the azimuth and elevation components of the $\vec{B}$ field, with the magnitude given by the average value, $B_{\rm ini}$. In order to ensure the initial magnetic field has zero divergence, we use a radial basis function to interpolate between the random grid vector values (McNally, 2011). An inherent property of this type of interpolation ensures $\nabla \cdot \vec{B} = 0$ for our initial magnetic field even when the random grid values alone are not necessarily divergence free.

Although the early evolution of a SNR is independent of magnetic fields, it is still possible to determine the evolution of the magnetic fields in terms of the other fluid quantities (Chevalier, 1974). In order to determine the magnetic field, $\vec{B}$, we combine Equation 4.11 with the Mass Equation 4.8, $\frac{D}{Dt}\left(\frac{1}{\rho}\right) = \frac{\nabla \cdot \vec{v}}{\rho}$:

$$\frac{D\vec{B}}{Dt} = \left(\vec{B} \cdot \nabla\right)\vec{v} - \vec{B}\left(\rho \, \frac{D}{Dt}\left(\frac{1}{\rho}\right)\right) \Rightarrow \frac{1}{\rho}\frac{D\vec{B}}{Dt} + \vec{B} \, \frac{D}{Dt}\left(\frac{1}{\rho}\right) = \frac{1}{\rho}\left(\vec{B} \cdot \nabla\right)\vec{v}$$

$$\Rightarrow \frac{D}{Dt}\left(\frac{\vec{B}}{\rho}\right) = \left(\frac{\vec{B}}{\rho}\right) \cdot \nabla\vec{v} \tag{4.22}$$

When compared to the flux conservation Lagrangian derivative, $\frac{D}{Dt}(d\vec{l}) = d\vec{l} \cdot \nabla \vec{v}$, this means that the magnetic flux is "frozen in" to the fluid. Because Equation 4.22 relates the evolution of the magnetic field to the evolution of only the density (which can be determined using the fluid equations), we can solve for the evolution of the magnetic field using density.

For an infinitesimally small fluid element, the magnetic field will be uniform through the entire fluid element, and we decompose the vector $\vec{B}$ into a component parallel to the direction of expansion, $\vec{B}_{\parallel}$, and a component orthogonal to the direction of expansion, $\vec{B}_{\perp}$:

$$\vec{B}_{\perp} \equiv \vec{B} \times \hat{r}\,, \quad \vec{B}_{\parallel} \equiv \left(\vec{B} \cdot \hat{r}\right) \hat{r} \tag{4.23}$$

$$\vec{B} = \vec{B}_{\perp} + \vec{B}_{\parallel} \tag{4.24}$$

Using the flux freezing condition and spherical symmetry we find the following relations for the initial and final magnetic fields (for further detail, see Appendix 4.8):

$$B_{\parallel,fin} = B_{\parallel,ini} \left(\frac{r_{ini}}{r_{fin}}\right)^2 \tag{4.25}$$

$$B_{\perp,fin} = B_{\perp,ini} \left(\frac{\rho_{fin} r_{fin}}{\rho_{ini} r_{ini}}\right) \tag{4.26}$$

With this relation between the initial and final magnetic fields, we can relate their divergences as well:

$$\begin{aligned} \nabla \cdot \vec{B}_{fin} &= \nabla \cdot \vec{B}_{\perp,fin} + \nabla \cdot \vec{B}_{\parallel,fin} \\ &= \nabla \cdot \vec{B}_{\perp,ini} \left(\frac{\rho_{fin} r_{fin}}{\rho_{ini} r_{ini}}\right) + \nabla \cdot \vec{B}_{\parallel,ini} \left(\frac{r_{ini}}{r_{fin}}\right)^2 \\ &= \left(\frac{\rho_{fin} r_{fin}}{\rho_{ini} r_{ini}}\right) \nabla \cdot \vec{B}_{\perp,ini} + \left(\frac{r_{ini}}{r_{fin}}\right)^2 \nabla \cdot \vec{B}_{\parallel,ini} \end{aligned} \tag{4.27}$$

Because our initial magnetic field has been interpolated to be divergence free, the

magnetic field will remain divergence free at all times:

$$\nabla \cdot \vec{B}_{ini} = 0 \Rightarrow \nabla \cdot \vec{B}_{\perp,ini} = \nabla \cdot \vec{B}_{\parallel,ini} = 0 \Rightarrow \nabla \cdot \vec{B}_{fin} = 0\,. \tag{4.28}$$

4.4.4 Hydrodynamic Simulations

Our hydrodynamic simulations used the RT1D code written by Duffell (2016). This is a 1-D+, adaptive, moving mesh code that includes R-T instabilities in SNe. Although the code is one-dimensional, it includes the multi-dimensional effects of Rayleigh-Taylor instabilities as a modification. This enables simulations of non-radiative SNR expansion based on the basic fluid equations, that run from the FE through the S-T phases. As noted by Duffell, the incorporation of R-T instabilities eliminates the singularities inherent in the C-N solutions and provides a more accurate position of the RS than found by Truelove & McKee (1999). The simulations are run in characteristic units; these are dimensionless units of the hydrodynamic quantities (i.e., in characteristic units, density is given by $\rho^* = \rho/\rho_{\rm ch}$, where $\rho_{\rm ch}$ is the characteristic density for the SN environment). The characteristic values are defined as:

$$r_{\rm ch} \equiv \left(\frac{M_{\rm ej}}{\rho_{\rm ISM}}\right)^{1/3} = 9.4 \text{ pc} \qquad t_{\rm ch} \equiv \frac{M_{\rm ej}^{5/6}}{\rho_{\rm ISM}^{1/3} E_{\rm SN}^{1/2}} = 3800 \text{ yr}$$

$$M_{\rm ch} \equiv M_{\rm ej} = 1.263\ M_\odot \qquad \rho_{\rm ch} \equiv \rho_{\rm ISM} = 0.061 m_p \text{ cm}^{-3}$$

$$v_{\rm ch} \equiv \frac{r_{\rm ch}}{t_{\rm ch}} = 2400 \text{ km s}^{-1} \qquad P_{\rm ch} \equiv \rho_{\rm ch} v_{\rm ch}^2 = 6.1 \times 10^{-9} \text{ dyn cm}^{-2}$$

$$T_{\rm ch} \equiv \frac{\mu_{\rm ej} m_u P_{\rm ch}}{k_B \rho_{\rm ch}} = \frac{\mu_{\rm ej} m_u}{k_B} v_{\rm ch}^2 = 4.4 \times 10^8 \text{ K} \tag{4.29}$$

These definitions are based on Truelove & McKee (1999) and assume a uniform ambient medium (for power-law, i.e., stellar wind, mediums see also: Truelove & McKee,

1999; Laming & Hwang, 2003; Haid et al., 2016).[1] Additional definitions of characteristic values incorporating power-law ambient mediums (i.e., stellar winds) can be made (see e.g, Truelove & McKee, 1999), but since we are examining the SNR expansion both inside and outside the pre-SN stellar wind, the uniform case is more appropriate.

The hydrodynamics simulations were begun at $t = 300$ ms ($t^* = 2.52 \times 10^{-12}$) after the core bounce which corresponds to the end the Wanajo et al. (2014) results, and run through $t = 3.8$ Myr ($t^* = 1000$). This encompasses the entire FE and S-T phases. The position values began at the cutoff range, $r_{\rm cutoff} = 9.52 \times 10^7$ cm ($r^*_{\rm cutoff} = 3.33 \times 10^{-12}$) and extended through the outermost range, $R = 9400$ pc ($R^* = 1000$) and were initially divided into 1024 zones. The simulation was run, and results were generated at 1000 logarithmically-spaced time intervals. The RT1D code adapts its time steps to accurately simulate the hydrodynamics; over 100K time steps were used during the run, but only 1000 were output in order to save memory requirements. Each output includes the radial position of the zone's midpoint, zone radial width, density, velocity, pressure, mixture fracture (the fraction of the zone comprised of ejecta material), and the turbulent factor (which was a measure of the R-T fluctuations, for our purposes this was not used). Because many of the results had nearly power-law profiles, 2-D quintic spline interpolation functions were generated for the common logarithms of the SNR quantities (i.e., $\log \rho^*$, $\log |v^*|$, etc) done across $\log t^* \times \log r^*$. The temperature interpolation was done with $\log T^* = \log (P^*/\rho^*)$. Additionally, with the assumption of spherical symmetry, the mass enclosed by a

[1]The characteristic temperature, $T_{\rm ch}$, is more commonly defined as: $T_{\rm ch} = \frac{3}{16}\frac{\mu m_p}{k_B}$(Truelove & McKee, 1999; McKee & Draine, 1991). This is a result of characteristic values defined based on jump conditions: $P_{\rm ch} = \frac{\rho_{\rm ISM} v_{\rm ch}^2}{\Gamma + 1} = \frac{\rho_{\rm ch} k_B T_{\rm ch}}{\mu m_p}$, $\rho_{\rm ch} = \left(\frac{\Gamma + 1}{\Gamma - 1}\right) \rho_{\rm ISM}$ with $\Gamma = 5/3$. This description is a more accurate gauge of the SN, but since our use of characteristic units are confined to unit conversions, our conclusions will not be affected by the distinction.

sphere at a given radial position, r, is described by:

$$M_{\text{enclosed}} = \int_{r_{\min}}^{r} 4\pi\rho(r')r'^2 \, dr' \tag{4.30}$$

where $r_{\min}$ is the innermost zone position in the RT1D simulation. Given the enclosed mass, and assuming no mixing within the ejecta, the elemental composition of SNR can be determined at any point.[2] With the interpolation functions, we have means to determine the density, velocity, temperature, and composition at all location within the SNR.

4.5 Grain Processes

Now that we have constructed the SNR environment, we can examine the influences acting on the dust grain. The radioisotopes will be formed deep within the ejecta; as the SNR expands, the ejecta will cool and overdensities in the ejecta will form clouds (also referred to as clumps, Silvia et al., 2010, 2012). This will begin $\sim 1-5$ years after the SN. The radioisotopes will chemically bond with the surrounding elements forming molecules first, then combining to form larger and larger grains. We assume our primary radioisotopes (^{60}Fe, ^{26}Al, ^{53}Mn, ^{41}Ca) will form compounds like their stable isotopes. In the case of ^{60}Fe, the bulk of which forms in a primarily Fe-Ni region (see Figure 4.1), we assume it will condense and form into metallic Fe grains rather than silicates, oxides, or sulfides since the associated elements are not present in that region of the ejecta. Conversely, ^{26}Al, which is created in an O-rich region, will likely form into AlO and Al_2O_3 molecules, and some of the ^{53}Mn will likely form MnS since it is created in a S-rich region (Field, 1975). Knowing the type of compound

[2]Although the existence of R-T instabilities inherently requires the presence of mixing, the R-T instability determines the large-scale RS location, while mixing will produce small-scale asymmetries in the SNR composition. Since we are interested in the average attributes of SNR dust transport, we ignore the smaller scale mixing.

the radioisotope exists inside is important since different compounds have different densities, are more/less resistant to erosion, and absorb/emit electrons and photons differently.

The grains will continue to grow until the RS arrives. Up to this point, the ejecta gas, overdense clouds, and the dust grains within have been traveling together with negligible relative velocities, the RS will slow and heat the gas and send a shock wave through the cloud, crushing it and shattering some of the dust grains. Several studies have examined this process (Silvia et al., 2010, 2012; Biscaro & Cherchneff, 2016), and our examination of the dust grains will begin just after this processing. The cloud containing the dust grains will dissipate, and the dust grains will be exposed to the hot SNR gas. Because of their higher mass, the dust grains will have decoupled from the gas and will be moving with a large relative velocity to the gas. A number of influences will now act on the dust grain (see Dwek & Arendt, 1992, and references therein), and we will now examine the most important processes in greater detail. We assume the grains to be spherical in shape with radius, a, and uniform in composition.

To track the trajectory of a dust grain within the SNR, we will solve a system of 8 ordinary differential equations (ODEs):

$$\frac{d\vec{r}_{\rm gr}}{dt} = \vec{v}_{\rm gr} \qquad \frac{da}{dt} = \sum_k N_k(a, q, \rho, T, ...)$$
$$\frac{d\vec{v}_{\rm gr}}{dt} = \sum_k \vec{F}_k(a, q, \rho, T, ...) \qquad \frac{dq}{dt} = \sum_k J_k(a, q, \rho, T, ...) \tag{4.31}$$

where the summed processes are dependent on the grain properties (size, charge, etc.) and the SNR environment (density, temperature, etc.).

Our specific initial grain conditions will be given in §4.6, but in qualitative terms, our dust grains will begin at, t_0, which corresponds to the time the RS passes the

location of the grain plus three times the cloud crushing time:

$$t_0 = t_{\rm RS} + 3\tau_{cc} \tag{4.32}$$

where the cloud crushing time is defined in terms of the cloud radius, a_c and the relative velocity of the RS, $v_{\rm RS}$ (Klein et al., 1994):

$$\tau_{cc} = a_c / v_{\rm RS} \tag{4.33}$$

We assume a cloud size of $a_c = 10^{16}$ cm (Silvia et al., 2010). The initial velocity, v_0, is determined by the velocity of the surrounding gas at the time of condensation. Dust condensation can begin over a range of times ($\sim 100 - 1000$ days after the explosion Sarangi & Cherchneff, 2015), and we assume condensation took place at 500 days after the explosion.[3] The dust grain will retain this initial velocity through the passage of the RS until the cloud has dissipated (i.e., t_0). The initial position of the grain, r_0, is the location of the grain at the time the cloud dissipates. Because we begin immediately after the cloud dissipates, the initial grain size, a_0, will be the post-RS/post-shattering size. Since we do not model grain growth, we examine a range of sizes. Lastly, the initial charge will be zero, $q_0 = 0$ since the grains are formed in a cool, dense cloud.

4.5.1 Grain Dynamics

Drag Force

Because the dust grains have a relative velocity compared to the surrounding gas, they will experience drag. Drag will be due to collisions with gas particles, and, since the gas is ionized and the grains charged (see §4.5.3), Coulomb drag (also called plasma

[3]Because of free expansion and the fact that we are not modeling grain growth, our results are not sensitive to the condensation time.

drag) may also be relevant. The combined drag of both sources is given by (Draine & Salpeter, 1979; Draine, 2011):

$$F_{\rm drag} = 2\pi a^2 k_B T \left\{ \sum_j n_j \left[G_0\left(s_j\right) + Z_j^2 \phi^2 \ln\left(\Lambda / Z_j\right) G_2\left(s_j\right) \right] \right\} \tag{4.34}$$

$$G_0\left(s\right) \equiv \left(s^2 + 1 - \frac{1}{4s^2} \right) \mathrm{erf}(s) + \frac{1}{\sqrt{\pi}} \left(s + \frac{1}{2s} \right) \exp\left[-s^2\right] \tag{4.35}$$

$$G_2\left(s\right) \equiv \frac{\mathrm{erf}(s)}{s^2} - \frac{2}{s\sqrt{\pi}} \exp\left[-s^2\right] \tag{4.36}$$

$$\phi_j \equiv eU / k_B T \tag{4.37}$$

$$s_j \equiv \left(m_j v_{\rm rel}^2 / 2 k_B T \right)^{1/2} \tag{4.38}$$

$$\Lambda \equiv \frac{3}{2ae\left|\phi\right|} \left(\frac{k_B T}{\pi n_e} \right)^{1/2} \tag{4.39}$$

$$\mathrm{erf}(\chi) \equiv \frac{2}{\sqrt{\pi}} \int_0^{\chi} \exp\left[-\tau^2\right] d\tau \tag{4.40}$$

using cgs/esu units. The $G_0(s)$ function accounts for collisional drag, and the $G_2(s)$ function accounts for Coulomb drag. Approximations exist for both functions, but we used the exact forms given here for completeness. The drag force is summed over all gas species, j, within the gas (e.g, p^+, e^-, α, C, etc.), each with number density, n_j. The velocity parameter, s, depends on the relative velocity, $v_{\rm rel}$, mass of the impacting gas particle, m_j, and the temperature of the gas, T (we assume all constituents are at the same temperature, i.e., $T_j = T \; \forall \; j$). Similarly, the potential parameter, ϕ depends on the potential of the grain, $U = q/a$ where q is the charge of the grain. The charge number of the gas particle is Z_j, k is the Boltzmann constant, and e is the elementary charge.

Lorentz Force

Because there will be magnetic fields present within the SNR and the grain will be charged, we include the Lorentz force on the grain:

$$\vec{F}_{\rm mag} = \frac{q}{c}\vec{v}_{\rm rel} \times \vec{B} \tag{4.41}$$

Because of flux freezing, the magnetic field, $\vec{B}$, will be moving with the plasma, so we use the grain's relative velocity, $\vec{v}_{\rm rel} = \vec{v}_{\rm gr} - \vec{v}_{\rm gas}$ to the plasma.

4.5.2 Grain Sputtering

In addition to drag from the grains' high relative velocity with the gas, the grain will also be eroded/sputtered by impacts with gas particles. In addition to kinetic sputtering from bulk motion of gas onto the grains, at high temperatures, the thermal velocities of gas particles will also erode the grain. Because of high relative velocities and high temperatures within the SNR, we include both kinetic and thermal sputtering. The erosion rate due to sputtering (both kinetic and thermal) is given by (Dwek & Arendt, 1992), and we use the approach by Nozawa et al. (2006); Biscaro & Cherchneff (2016):

$$\frac{da}{dt} = -\frac{m_{sp}}{4\rho_{\rm gr}} \sum_j \frac{n_j}{s_j} \left(\frac{8k_B T}{\pi m_j}\right)^{1/2} \exp\left[-s_j^2\right] \int \sqrt{\epsilon_j} \exp\left[-\epsilon_j\right] \sinh\left(2s_j\sqrt{\epsilon_j}\right) Y_j^0(\epsilon_j) d\epsilon_j \tag{4.42}$$

where m_{sp} is the mass of the sputtered atom (i.e., the average atomic mass for the dust composition, $m_{sp,\rm Fe} = 56m_u$, $m_{sp,\rm FeO} = 36m_u$, $m_{sp,\rm Fe_2O_3} = 32m_u$, $m_{sp,\rm Fe_3O_4} = 33.1m_u$), and $\rho_{\rm gr}$ is the density of the dust grain. Additionally, the angle-averaged sputtering yield given by: $\langle Y_j(E_j)\rangle_\theta = 2Y_j^0(E_j)$ (Draine & Salpeter, 1979) with the backward

sputtering yield at normal incidence, $Y_j^0(E)$, given by (Bohdansky, 1984):

$$Y_j^0\left(\epsilon_j\right) = 4.2 \times 10^{14} \ \frac{\text{at}}{\text{ion}} \left(\frac{S_j(E)}{E_B}\right) \left(\frac{\alpha_j(\mu_j)}{\kappa\mu_j + 1}\right) \times \left(1 - \left(\frac{E_{th}}{E}\right)^{2/3}\right) \left(1 - \left(\frac{E_{th}}{E}\right)\right)^2 \tag{4.43}$$

where κ is a free parameter that is adjusted to fit experimental data, E_B is the surface binding energy, and $\mu_j = m_d/m_j$ is the ratio of the target atom mass, m_d, to the incident atom mass, m_j. The threshold energy, E_{th}, to induce sputtering is given by (Andersen & Bay, 1981; Bohdansky, 1984):

$$E_{th} = \begin{cases} \dfrac{E_B}{g_j(1-g_j)} & \text{for } m_j/m_d \leq 0.3 \\ 8E_B\left(\dfrac{m_j}{m_d}\right)^{1/3} & \text{for } m_j/m_d > 0.3 \end{cases} \tag{4.44}$$

where $g_j = 4m_j m_d \left(m_j + m_d\right)^{-2}$ is the maximum fraction energy transfer in a head-on elastic collision. The nuclear stopping cross-section, $S_j(E)$, is given by (Sigmund, 1981):

$$S_j(E) = 4\pi a_{sc} Z_j Z_d e^2 \frac{m_j}{m_j + m_d} \varsigma_j(\epsilon_j)\,, \tag{4.45}$$

and the screening length, a_{sc}, for interaction between nuclei is:

$$a_{sc} = 0.885 a_0 \left(Z_j^{2/3} + Z_d^{2/3}\right)^{-1/2}\,, \tag{4.46}$$

where $a_0 = 0.529$ Å is the Bohr radius. An approximation of the function, $\varsigma_j(\epsilon_j)$ is given by Matsunami et al. (1984):

$$\varsigma_j(\epsilon_j) = \frac{3.441\sqrt{\epsilon_j}\ln\left(\epsilon_j + 2.718\right)}{1 + 6.35\sqrt{\epsilon_j} + \epsilon_j\left(6.882\sqrt{\epsilon_j} - 1.708\right)} \tag{4.47}$$

Table 4.1: Summary of Sputtering Yield Parameters

Dust Species	E_B [eV]	Z_d	m_d	κ
Fe	4.31	26	56	0.23
FeO	4.98	17	36	0.15
Fe_2O_3	4.98	15.2	32	0.15
Fe_3O_4	4.98	15.7	33.1	0.15
Al_2O_3	8.5	10	20.4	0.08

Values are from (Nozawa et al., 2006, and references therein). The binding energy and κ parameters for FeO and Fe_2O_3 are assumed to be the same as Fe_3O_4.

where the reduced energy, ϵ_j, is:

$$\epsilon_j = \frac{m_d}{m_j + m_d} \frac{a_{sc}}{Z_j Z_d e^2} E \tag{4.48}$$

The function $\alpha_j(\mu_j)$, depends on the energy distribution deposited into the target, and we used the derivation by Nozawa et al. (2006) for $\mu_j \in [0.3, 56]$:

$$\alpha_j(\mu_j) = \begin{cases} 0.2 & \mu_j \leq 0.5 \\ 0.1\mu_j^{-1} + 0.25\left(\mu_j - 0.5\right)^2 & 0.5 < \mu_j \leq 1 \\ 0.3\left(\mu_j - 0.6\right)^2 & 1 < \mu_j \end{cases} \tag{4.49}$$

4.5.3 Grain Charging

As grains move within the SNR, they will acquire/lose electrons and ions due to impacts with the plasma or photons. Several processes can influence the total charge

of the grain, so the total charging rate, dq/dt is:

$$\frac{dq}{dt} = \sum_k J_k \tag{4.50}$$

which is summed over k processes of currents, J_k. These currents are due to impinging plasma particles, $J_{\rm imp}$, and the associated secondary electrons emitted, $J_{\rm see}$, transmitted plasma particles, $J_{\rm trans}$, and photoelectron emission, J_γ. The following derivations are the same as used by Kimura & Mann (1998).

Impinging Ions/Electrons

Charging by impinging plasma particles is caused by incident ions/electrons impacting the surface of the grain, sticking, and altering the grain charge. It is given by (Dwek & Arendt, 1992):

$$J_{\rm imp} = 2\pi e \sum_j Z_j \int_{v_0}^{\infty} dv_{\rm th} \int_0^{\pi} d\theta \sigma_j(v_{\rm th}) f_j(v_{\rm th}, \theta) v_{\rm th}^3 \sin\theta \tag{4.51}$$

where $v_{\rm th}$ is the thermal velocity. The minimum impinging velocity, v_0, is the given by:

$$v_0 = \begin{cases} 0 & Z_j\phi_j \leq 0\,, \\ \\ (2Z_j eU/m_j)^{1/2} & Z_j\phi_j > 0\,, \end{cases} \tag{4.52}$$

with the collisional cross-section, $\sigma_j(v_{\rm th})$, given by:

$$\sigma_j(v_{\rm th}) = \pi a^2 \left(1 - \frac{2Z_j eU}{m_j v_{\rm th}^2}\right) \tag{4.53}$$

Because the dust grains will potentially have large relative velocities to the gas, as well as large thermal velocities, we assume a Maxwellian velocity distribution, $f_j(v_{\rm th}, \theta)$:

$$f_j(v_{\rm th}, \theta) = n_j \left(\frac{m_j}{2\pi k_B T}\right)^{3/2} \exp\left[-\frac{m_j}{2k_B T}\left(v_{\rm th}^2 + v_{\rm rel}^2 - 2v_{\rm th} v_{\rm rel}\cos\theta\right)\right] \tag{4.54}$$

where θ is the angle between the thermal and relative velocities.

Secondary Electron Emission

If the impinging plasma particles have sufficient initial energy, $E_0 = 2k_B T + \frac{1}{2}m_j v_{\rm rel}^2 + Z_j eU$ (Draine & Salpeter, 1979; McKee et al., 1987; Kimura & Mann, 1998), then after initially ejecting an electron, there is sufficient energy to eject additional electrons. In this situation, the current of secondary electrons, $J_{\rm see}$, is:

$$J_{\rm see} = 2\pi e \sum_j \delta_j(E_0) \int_{\epsilon_{min}}^{\infty} d\epsilon \rho_j(\epsilon) \int_{v_0}^{\infty} dv_{\rm th} \int_0^{\pi} d\theta \sigma_j(v_{\rm th}) f_j(v_{\rm th}, \theta) v_{\rm th}^3 \sin\theta \tag{4.55}$$

where the minimum required energy is $\epsilon_{min} = \max(0, eU)$. The type and energy of impacting plasma particles will determine the effectiveness of secondary emission, so the secondary electron yield, $\delta_j(E_0)$, is given for electrons by (Draine & Salpeter, 1979):

$$\delta_e(E_0) = \delta_m \frac{8(E_0/E_m)}{(1 + E_0/E_m)^2}\left[1 - \exp\left(-\frac{4a}{3\lambda_{\rm esc}}\right)\right] f_1\left(\frac{4a}{3R}\right) f_2\left(\frac{a}{\lambda_{\rm esc}}\right) \tag{4.56}$$

where the fitting functions, f_1 and f_2, are given by:

$$f_1(\chi) = \frac{1.6 + 1.4\chi^2 + 0.54\chi^4}{1 + 0.54\chi^4} \tag{4.57}$$

$$f_2(\chi) = \frac{1 + 2\chi^2 + \chi^4}{1 + \chi^4} \tag{4.58}$$

Table 4.2: Escape Length, $\lambda_{\rm esc}$, Parameters for Iron

Dust Species	q_e	$r_m(q_e)$
Fe	1.5662	1.1891
FeO	1.5918	1.1631
Fe_2O_3	1.5935	1.1611
Fe_3O_4	1.5993	1.1561

Electron stopping ranges are based on outputs from the CASINO software (Drouin et al., 2007).

and the escape length for electrons, $\lambda_{\rm esc}$ is:

$$\lambda_{\rm esc} = R_e(E_m)/r_m(q_e)^{q_e} \tag{4.59}$$

where the value of r_m is given for various materials in Table 4.2. The maximum yield from a bulk solid, δ_m, at energy, E_m, is assumed to be 1.3 and 400 eV respectively CRC Handbook (2008). The secondary yield for ions is given by the empirical formula in Draine & Salpeter (1979):

$$\delta_{\rm ion}(E_0) = 0.1 Z_j^2 \frac{1 + (m_H/m_j)(E_0/\phi_1)}{\left[1 + (m_H/m_j)(E_0/\phi_2)\right]^2} \begin{cases} 1 & U \leq 0\,, \\ 1 + \left(\dfrac{U}{1\ \mathrm{V}}\right) & U > 0\,, \end{cases} \tag{4.60}$$

where $\phi_1 = 500$ eV and $\phi_2 = 35$ keV.

Lastly, the energy distributions ρ_j for secondary electrons emitted by electrons and

ions are given by:

$$\rho_e(E) = \frac{E}{2\phi_e^2}\left[1 + \frac{1}{2}\left(\frac{E}{\phi_e}\right)^2\right]^{-3/2} \tag{4.61}$$

$$\rho_{\rm ion}(E) = \frac{1}{\phi_{\rm ion}}\left[1 + \frac{1}{2}\left(\frac{E}{\phi_{\rm ion}}\right)^2\right]^{-2} \tag{4.62}$$

where the most probable energies are $\phi_e = 2$ eV and $\phi_{\rm ion} = 1$ eV.

Transmission of Ions/Electrons

The transmission (also referred to tunneling, Chow et al., 1993) current of ions/electrons, $J_{\rm tran}$, accounts for the plasma particles with sufficient velocity to penetrate completely through the grain without being captured:

$$J_{\rm tran} = -2\pi e \sum_j Z_j \int_{v_1}^{\infty} dv_{\rm th} \int_0^{\pi} d\theta \sigma_j(v_{\rm th}) f_j(v_{\rm th}, \theta) v_{\rm th}^3 \sin\theta \tag{4.63}$$

where the minimum velocity, v_1, required to pass through the grain is (Draine & Salpeter, 1979; McKee et al., 1987; Kimura & Mann, 1998):

$$v_1 = \begin{cases} \dfrac{\left(2k_BT + \frac{1}{2}m_j v_{\rm rel}^2\right)\psi_j}{m_j} & Z_j\phi_j \leq 0\,, \\ \dfrac{\left(2k_BT + \frac{1}{2}m_j v_{\rm rel}^2\right)\left(\psi_j + Z_j\phi_j\right)}{m_j} & Z_j\phi_j > 0\,. \end{cases} \tag{4.64}$$

From Draine & Salpeter (1979), the energy, $\left(k_BT + \frac{1}{2}m_j v_{\rm rel}^2\right)\psi_j$, required to penetrate a grain is given by:

$$\left(k_BT + \frac{1}{2}m_j v_{\rm rel}^2\right)\psi_j = \begin{cases} \Delta_j & Z_j < 0\,, \\ \Delta_j + E_H & Z_j > 0\,. \end{cases} \tag{4.65}$$

Additionally, we assume that the ions emerge neutral because of recombination if their energy is below the Bohr Energy, $E_H = (m_j/m_e)I_H$ with $I_H = 13.6$ eV.

The penetration threshold energy, Δ_j, is found using an energy-range relation and the size of the dust grain (Fitting, 1974):

$$R_j(\Delta_j) \equiv 4a/3 \tag{4.66}$$

The energy-range relation is based on measured stopping ranges for various particles into materials, and we used outputs from the SRIM software (Ziegler & Biersack, 1985; Ziegler et al., 2010) for ion and the CASINO software (Drouin et al., 2007) for electron stopping in materials and fit power-law profiles to the results in the form:

$$R_j(E) = R_{0,j}E^{\alpha_j} \tag{4.67}$$

A compilation of the fit values are listed in Table 4.3.

Photoelectron Emission

The dust grains will be exposed to UV photons, and, depending on the grain material, electrons will be emitted from the surface of the grain. The photoelectric current, J_γ, then is given by:

$$J_\gamma = e\int_{W+\epsilon_{min}}^{\infty} d(h\nu)C_{\rm abs}(h\nu)\mathbb{F}_\gamma(h\nu)Y_\gamma(h\nu)\int_{\epsilon_{min}}^{\epsilon_{max}} d\epsilon\rho_\gamma(\epsilon) \tag{4.68}$$

with $\epsilon_{max} = h\nu - W$, h is Planck's constant, ν is the photon frequency, and W is the work function required to emit an electron. The photoelectric yield, $Y_\gamma(h\nu)$, is the number of electrons emitted per absorbed photon (Draine & Salpeter, 1979):

$$Y_\gamma(h\nu) = \frac{(h\nu - B + E_{\rm min})^2 - E_{\rm min}^2}{(h\nu)^2 - E_{\rm min}^2}\left[1 - \left(1 - \frac{\lambda_{\rm esc}}{a}\right)^3\right] \tag{4.69}$$

where $B = 8$ eV and $E_{\min} = 6$ eV. Following the example of Kimura & Mann (1998), we set $B = W$. The energy distribution, $\rho_\gamma(E)$, of photoelectrons (Grard, 1973):

$$\rho_\gamma(E) = \frac{E}{\phi_\gamma^2} \exp\left[-\frac{E}{\phi_\gamma}\right] \tag{4.70}$$

where $\phi_\gamma = 1$ eV.

Because the SNR is expected to be non-radiative for our examination, we assume the photon flux, $\mathbb{F}_\gamma(h\nu)$, is a blackbody at temperature, T, at the location of the grain inside the SNR or the average interstellar background (see e.g., Draine, 2011) outside the SNR. Additionally, the absorption cross-section of the grain, $C_{\rm abs}(h\nu)$, is dependent on the photon energy, grain size, and complex index of refraction. The complex indices of refraction for iron from Pollack et al. (1994) were used and $C_{\rm abs}(h\nu)$ was calculated using Mie theory and the procedure from Bohren & Huffman (1983). However, this method is extremely calculation intensive, and in order to simplify calculations, the $C_{\rm abs}(h\nu)$ approximation given by Draine & Salpeter (1979) was used:

$$C_{\rm abs}(h\nu) = \frac{\pi a^3}{a + 0.01\ \mu\text{m}}\,. \tag{4.71}$$

This approximation shows good agreement with calculation using Mie theory for iron within the region we are interested in. A comparison for various grain sizes are shown in Figure 4.4.

Simplified Charging Description

As should be obvious from the previous charging sections, including all of the relevant charging processes is extremely calculation intensive. However, if we compare the gyro

period (Equation 4.2):

$$\tau_{\rm gyro} = 34 \text{ yr} \left(\frac{\rho_{\rm gr}}{7.87 \text{ g cm}^{-3}}\right) \left(\frac{2}{|\phi|}\right) \left(\frac{1 \ \mu\text{G}}{B}\right) \left(\frac{10^6 \text{ K}}{T}\right) \left(\frac{a}{0.1 \ \mu\text{m}}\right)^2 , \tag{4.72}$$

to a basic approximation of the charging time (for negative charging, Shukla & Mamun, 2002):

$$\tau_{\rm charge} = 0.06 \text{ yr} \sqrt{\frac{T}{10^6 \text{ K}}} \left(\frac{0.1 \text{ cm}^{-3}}{n_{\rm ISM}}\right) \left(\frac{0.1 \ \mu\text{m}}{a}\right) \left(\frac{1}{1 + \sqrt{\frac{m_p}{m_e}} \exp\left[-\left(\frac{\phi}{2}\right)\right]}\right) , \tag{4.73}$$

we see the charging time is much less than the gyro period ($\tau_{\rm charge} \ll \tau_{\rm gyro}$), allowing us to use an analytic approximation to the grain change when solving for the grain's gyroscopic motions. In order to use a faster description of grain charging processes, we used the formulation derived by Shull (1978) and extended with an analytic fit by McKee et al. (1987) (meaning we no longer solve for dq/dt in our system of ODEs). The fit by McKee et al. approximates the grain potential parameter, ϕ, by:

$$\phi = \phi_0(1 - \psi) + \psi\phi_1 \tag{4.74}$$

where

$$\begin{aligned} \phi_0 = &- 0.5 + 4.17\chi - 2.65\chi^2 + 0.525\chi^3 + 1.4 \exp\left[-a/\lambda_{\rm esc}\right] \\ &- 2 \exp\left[-0.126 \left(\left(\frac{v_{\rm rel}}{10^7 \text{ cm s}^{-1}}\right) \left(\frac{10^5 \text{ K}}{T}\right)\right)^{0.6}\right] \end{aligned} \tag{4.75}$$

and

$$\phi_1 = 0.9 \left(\frac{10^5 \text{ K}}{T}\right) \tag{4.76}$$

The function, ψ, is defined as:

$$\psi = \exp\left[-\left(\frac{T_{\rm cr}}{T}\right)^4\right] \tag{4.77}$$

with the critical temperature, $T_{\rm cr}$:

$$T_{\rm cr} = 1.7 \times 10^5 \text{ K}\left(1 - \exp\left[-\left(\frac{a}{\lambda_{\rm esc}}\right)^{0.36}\right]\right) \tag{4.78}$$

and

$$\chi = 0.1\zeta\sqrt{\frac{10^5 \text{ K}}{T}} \tag{4.79}$$

The flux parameter, ζ, is a gauge the UV flux received by the grain. Since we have assumed the SNR is non-radiative, we set $\zeta = 0$. We also establish potential limits to account for field emission:

$$\begin{aligned} \phi_0 &\leq \phi_{0,\rm max} \\ \phi_{\rm min} \leq \phi &\leq \phi_{\rm max} \end{aligned}$$

$$\begin{aligned} \phi_{\rm min} &= -1.16\left(\frac{a}{0.01\ \mu\text{m}}\right)\left(\frac{10^5 \text{ K}}{T}\right) \\ \phi_{\rm max} &= 34.8\left(\frac{a}{0.01\ \mu\text{m}}\right)\left(\frac{10^5 \text{ K}}{T}\right) \end{aligned} \tag{4.80}$$

Lastly, in the event the grain emerges from the SNR, we set the potential of the grain to 5.6 V since it will be in interstellar space and subject to the ISRF (Draine & Salpeter, 1979; Draine, 2011). This completes our description of the grain charge so

that:

$$U(r) = \begin{cases} \phi k_B T/e & r < R_{\rm SN} \\ 0 \text{ V} & r = R_{\rm SN} \\ 5.6 \text{ V} & r > R_{\rm SN} \end{cases} \tag{4.81}$$

4.6 Results

We examined the trajectories for ^{60}Fe-containing dust grains in a SNR expanding into an ISM with a non-uniform magnetic field with a characteristic length, $\lambda_{\rm mag} = 6$ pc. We assumed the grains contained material originally at 0.6×10^9 cm at the beginning of the hydrodynamic simulation; this corresponds to the highest concentration of ^{60}Fe within the ejecta (see Figure 4.1). The ^{60}Fe was assumed to condense into metallic-Fe grains at 500 days after the SN which corresponds to $r_{\rm gr}$ = cm and $v_{\rm gr}$ = km s^{-1}. The grain proceeded until encountering the RS at $t = 5 \times 10^3$ yr. After the cloud dissipates and the grain is assumed to be first exposed to the shocked SNR environment, the simulation begins at $t_0 = 6700$ yr, $r_0 = 2.6$ pc, $v_0 = 375$ km s^{-1}. We examined a variety of post-RS grain sizes ranging from $0.001 - 1$ μm. Figure 4.5 shows a sample result for an initial $a = 0.1$-μm grain; the grain does experience some drag and sputtering, but they are relatively minor since the relative velocity $v_{\rm rel} \approx 175$ km s^{-1}. There is also little to no deflection of the grain's trajectory while the grain is traveling through pre-SN circumstellar material. This is because there is no magnetic field in this material, but shortly after encountering shocked ISM material, the frozen-in ISM magnetic field reflects the grain back into the SNR. These features appear as 'U'-shaped trajectories in the upper, center panel of Figure 4.5.

4.7 Conclusions

These preliminary results show that the inclusion of R-T instabilities is important; Figure 4.7 shows the grains enter the shocked medium as early as 6700 years, rather than later at $\sim 2 \times 10^5$ yr when the RS proceeds inward to the center of the SNR. By entering the shocked plasma early, grain growth is halted earlier limiting the size of the grains.

The inclusion of magnetic fields from pre-SN ISM material is important to tracking dust movement within the SNR. Dust is not distributed throughout the SNR, but confined much deeper within the SNR. The possibility of a Sco-Cen progenitor ($D \sim$ 130 pc) as the source of the ^{60}Fe is extremely unlikely given that magnetic fields restrict the movement of the dust grains. Although Sco-Cen have yielded a larger, more powerful progenitor (e.g., 15-$M_\odot$ CCSN), the result may be similar because the ISM magnetic field and the non-uniform magnetic field arrangement are the limiting factors in the dust grains' propagation, not the explosive energy ($E_{\rm SN}$). Tuc-Hor is still a likely source, as the simulation showed consistent dust propagation out to $\sim$60 pc, which is the distance to Tuc-Hor.

Grains are not confined to the shell region as assumed by Fry et al. (2015, 2016); Breitschwerdt et al. (2016), but spread throughout the interior of the SNR. This potentially explains the extended signal from Wallner et al. (2016), but negates the proposal by Fry et al. (2015) of using time-resolved samples as an alternate gauge of the SN's distance. On the other hand, the time-resolved samples will yield a measure of the SNR's propagation and internal dust distribution.

The bouncing of dust grains also alters the assumption of a plane wave arrival of SN dust grains into the Solar System. Although, the dependence will likely weaken with time, it appears possible that after the SNR passes over the Solar System that dust grains will bounce off the SNR shell and approach Earth from a direction nearly

opposite of the SN! Further characterization of this passage is needed to determine the viability of using lunar samples to determine the direction to the SN as proposed by Fry et al. (2016).

Additional simulations using other radioisotopes are planned. Based the preliminary results, it appears ^{26}Al and ^{41}Ca (which form in the front portion of the ejecta making them more likely to encounter the RS before ^{60}Fe) will not form as long, as large, and since their density is less than metallic Fe, will be much more sensitive to sputtering and the magnetic fields. A portion of ^{53}Mn is slightly further back and may form MnS, but the bulk of ^{41}Ca and ^{53}Mn are deeper in the ejecta than ^{60}Fe. The question remains as to what type of dust, if any, they will form into. Additional simulations are also planned to fully characterize the dust grains' movement within the SNR. These include varying the condensation location/time, the ISM density and magnetic field, the inclusion of a turbulent magnetic field along the forward shock (Inoue et al., 2009; Ji et al., 2016), examining the case of a lack of an H/He envelope around the pre-SN star (Fremling et al., 2016), and the grain composition/sizes further.

4.8 Flux Freezing with Spherical Symmetry

In the case of a spherical expansion of a plasma, the magnetic fields will be "frozen in" the plasma as it expands. If the expansion of the fluid can be determined entirely by the basic (i.e., non-MHD) fluid equations, then it is possible to solve for the magnetic field as the plasma expands. Using the integral definition of magnetic flux: $\Phi = \int \vec{B} \cdot d\vec{A}$, the initial and final magnetic fluxes through the surface containing a fluid element will be the same, i.e., $\Phi_{ini} = \Phi_{fin}$. Since we are following a particular fluid element, the mass contained within will remain the same as well, i.e., $m_{ini} = m_{fin}$.

Using a spherical coordinate system with the origin at the center of the expansion,

we define a fluid element with differential volume:

$$dV = r^2 \sin\theta \; dr \; d\theta \; d\phi \tag{4.82}$$

and differential areas:

$$dA_{\text{face}} = r^2 \sin\theta \; d\theta \; d\phi = r^2 \; d\Omega \tag{4.83}$$

$$dA_{\text{top}} = r \sin\theta \; dr \; d\phi \tag{4.84}$$

$$dA_{\text{side}} = r \; dr \; d\theta \tag{4.85}$$

with dA_{face} the surface facing the direction of expansion, dA_{top} the upper surface, and dA_{side} one of the side surfaces of the fluid element. The remaining three surfaces of the fluid element have the same areas, but because of the Gauss' Law ($\oint \vec{B} \cdot d\vec{A} = 0$), we only focus on three sides.

As the fluid element moves away from the origin, by spherical symmetry, the angular properties of the fluid element will remain the same:

$$d\theta_{ini} = d\theta_{fin} \,, \quad d\phi_{ini} = d\phi_{fin} \,, \quad \sin\theta_{ini} = \sin\theta_{fin} \tag{4.86}$$

$$\sin\theta_{ini} \; d\theta_{ini} \; d\phi_{ini} = \sin\theta_{fin} \; d\theta_{fin} \; d\phi_{fin} \Rightarrow d\Omega_{ini} = d\Omega_{fin} \tag{4.87}$$

Additionally, the fluid element will compress and expand, but while it's mass will remain constant, it's density will change:

$$\rho_{ini} = \frac{m_{ini}}{r_{ini}^2 \; dr_{ini} \; d\Omega_{ini}} \,, \qquad \rho_{fin} = \frac{m_{fin}}{r_{fin}^2 \; dr_{fin} \; d\Omega_{fin}} \tag{4.88}$$

$$\Rightarrow \rho_{ini} r_{ini}^2 \; dr_{ini} = \rho_{fin} r_{fin}^2 \; dr_{fin} \Rightarrow \frac{dr_{ini}}{dr_{fin}} = \frac{\rho_{fin} r_{fin}^2}{\rho_{ini} r_{ini}^2} \tag{4.89}$$

For an infinitesimally small fluid element, the magnetic field will be uniform through

the entire fluid element, and we can decompose the vector $\vec{B}$ into a component parallel to the direction of expansion, $\vec{B}_{\parallel}$, and a component orthogonal to the direction of expansion, $\vec{B}_{\perp}$:

$$\vec{B}_{\perp} \equiv \vec{B} \times \hat{r}\,, \quad \vec{B}_{\parallel} \equiv \left(\vec{B} \cdot \hat{r}\right) \hat{r} \tag{4.90}$$

$$\vec{B} = \vec{B}_{\perp} + \vec{B}_{\parallel} \tag{4.91}$$

With these definitions, we can calculate the flux through each surface:

$$d\Phi = \vec{B} \cdot d\vec{A} \Rightarrow \tag{4.92}$$

$$d\Phi_{\text{face}} = B_{\parallel} r^2 \; d\Omega \Rightarrow B_{\parallel,ini} r_{ini}^2 \; d\Omega_{ini} = B_{\parallel,fin} r_{fin}^2 \; d\Omega_{fin}$$

$$B_{\parallel,fin} = B_{\parallel,ini} \left(\frac{r_{ini}}{r_{fin}}\right)^2 \tag{4.93}$$

Defining α as the angle between the normal of the top surface and $\vec{B}_{\perp}$:

$$d\Phi_{\text{top}} = B_{\perp} \cos\alpha \; r \sin\theta \; dr \; d\phi$$

$$\Rightarrow B_{\perp,ini} \cos\alpha_{ini} \; r_{ini} \sin\theta_{ini} \; dr_{ini} \; d\phi_{ini} = B_{\perp,fin} \cos\alpha_{fin} \; r_{fin} \sin\theta_{fin} \; dr_{fin} \; d\phi_{fin}$$

$$B_{\perp,fin} = B_{\perp,ini} \left(\frac{\cos\alpha_{ini}}{\cos\alpha_{fin}}\right) \left(\frac{r_{ini}}{r_{fin}}\right) \left(\frac{dr_{ini}}{dr_{fin}}\right)$$

Using Equation 4.89:

$$B_{\perp,fin} = B_{\perp,ini} \left(\frac{\cos\alpha_{ini}}{\cos\alpha_{fin}}\right) \left(\frac{r_{ini}}{r_{fin}}\right) \left(\frac{\rho_{fin} r_{fin}^2}{\rho_{ini} r_{ini}^2}\right) \tag{4.94}$$

$$\Rightarrow B_{\perp,fin} = B_{\perp,ini} \left(\frac{\cos\alpha_{ini}}{\cos\alpha_{fin}}\right) \left(\frac{\rho_{fin} r_{fin}}{\rho_{ini} r_{ini}}\right) \tag{4.95}$$

$$d\Phi_{\text{side}} = B_{\perp} \sin\alpha \; r \sin\theta \; dr \; d\phi \tag{4.96}$$

$$\Rightarrow B_{\perp,ini} \sin\alpha_{ini} \; r_{ini} \sin\theta_{ini} \; dr_{ini} \; d\phi_{ini} = B_{\perp,fin} \sin\alpha_{fin} \; r_{fin} \sin\theta_{fin} \; dr_{fin} \; d\phi_{fin}$$

$$B_{\perp,fin} = B_{\perp,ini}\left(\frac{\sin\alpha_{ini}}{\sin\alpha_{fin}}\right)\left(\frac{r_{ini}}{r_{fin}}\right)\left(\frac{dr_{ini}}{dr_{fin}}\right)$$

Using Equation 4.89:

$$B_{\perp,fin} = B_{\perp,ini}\left(\frac{\sin\alpha_{ini}}{\sin\alpha_{fin}}\right)\left(\frac{r_{ini}}{r_{fin}}\right)\left(\frac{\rho_{fin}r_{fin}^2}{\rho_{ini}r_{ini}^2}\right) \tag{4.97}$$

$$\Rightarrow B_{\perp,fin} = B_{\perp,ini}\left(\frac{\sin\alpha_{ini}}{\sin\alpha_{fin}}\right)\left(\frac{\rho_{fin}r_{fin}}{\rho_{ini}r_{ini}}\right) \tag{4.98}$$

In order for both Equations 4.95 and 4.98 to be true:

$$\Rightarrow \frac{\cos\alpha_{ini}}{\cos\alpha_{fin}} = \frac{\sin\alpha_{ini}}{\sin\alpha_{fin}} = 1 \Rightarrow \tag{4.99}$$

$$B_{\perp,fin} = B_{\perp,ini}\left(\frac{\rho_{fin}r_{fin}}{\rho_{ini}r_{ini}}\right) \tag{4.100}$$

Combining Equations 4.93 and 4.100 gives a means of relating initial conditions and final densities to the final magnetic field.

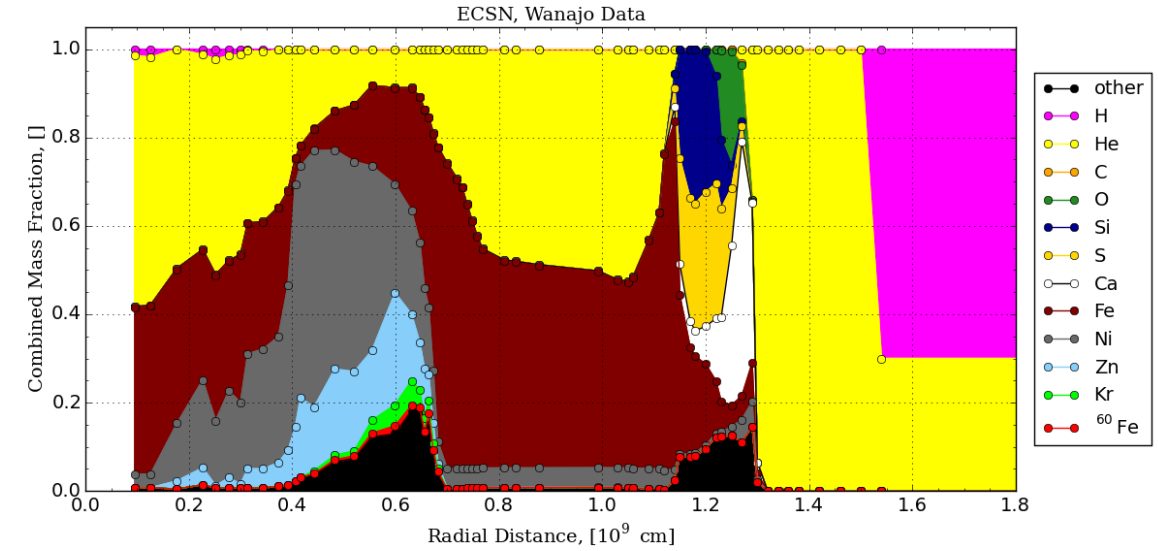

(a)

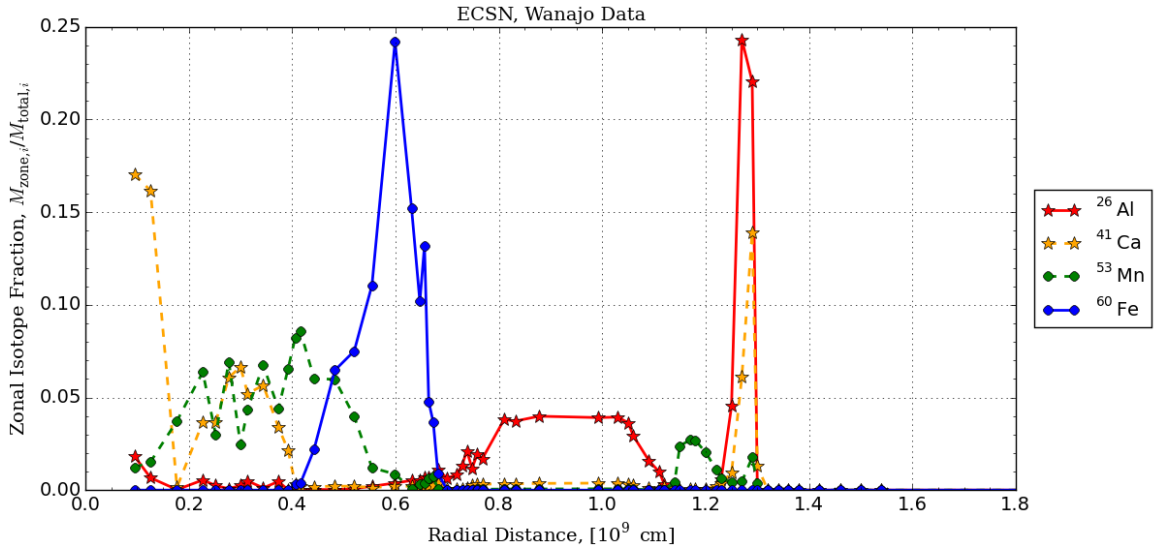

(b)

Figure 4.1: *Nucleosynthesis products within each zone. The upper panel shows the mass fractions for the main stable nucleosynthesis products, and the lower panel shows the relative distribution of the main radioisotopes. Note that the mass fractions for each element are stacked not absolute; to find the absolute mass fraction for an element, subtract the value of the element plotted just below it. By comparing the concentrations of the radioisotopes in Figure 4.1(b) to the stable products in Figure 4.1(a), we can estimate the most likely dust molecules the radioisotopes will condense into.*

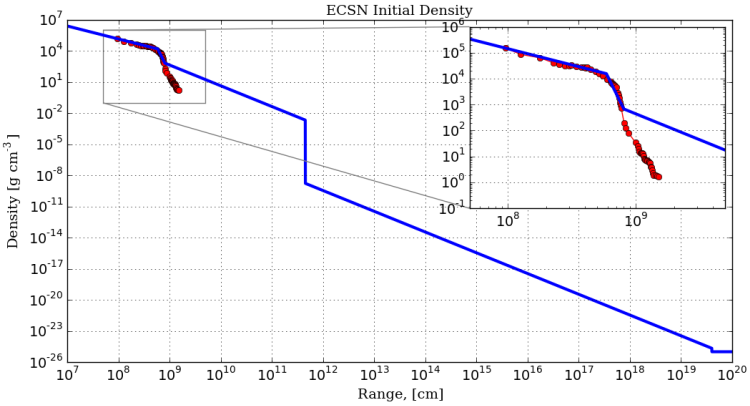

(a)

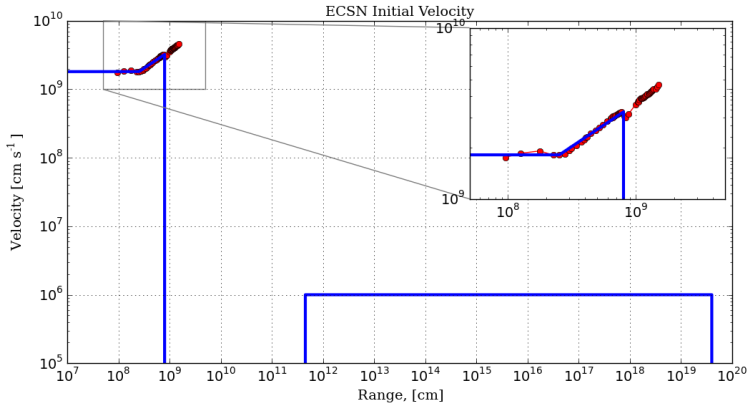

(b)

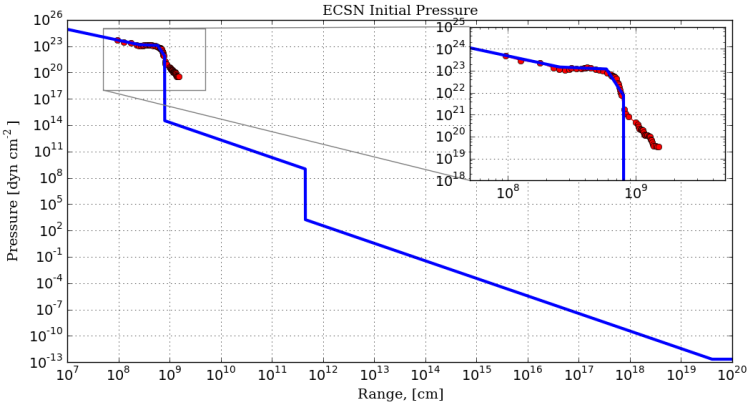

(c)

Figure 4.2: *Initial Density, Velocity, and Pressure Profiles. Our initial profiles is shown in blue with the azimuthally-averaged Wanajo et al. (2014) ECSN results plotted in red. Because our model included an outer envelope (similar to Janka et al., 2008) the envelope profile contains some of the nucleosynthesis products. The composition of the envelope was adjusted to include the nucleosynthesis products' mass, but these products were given the initial density, velocity, and pressure of the envelope.*

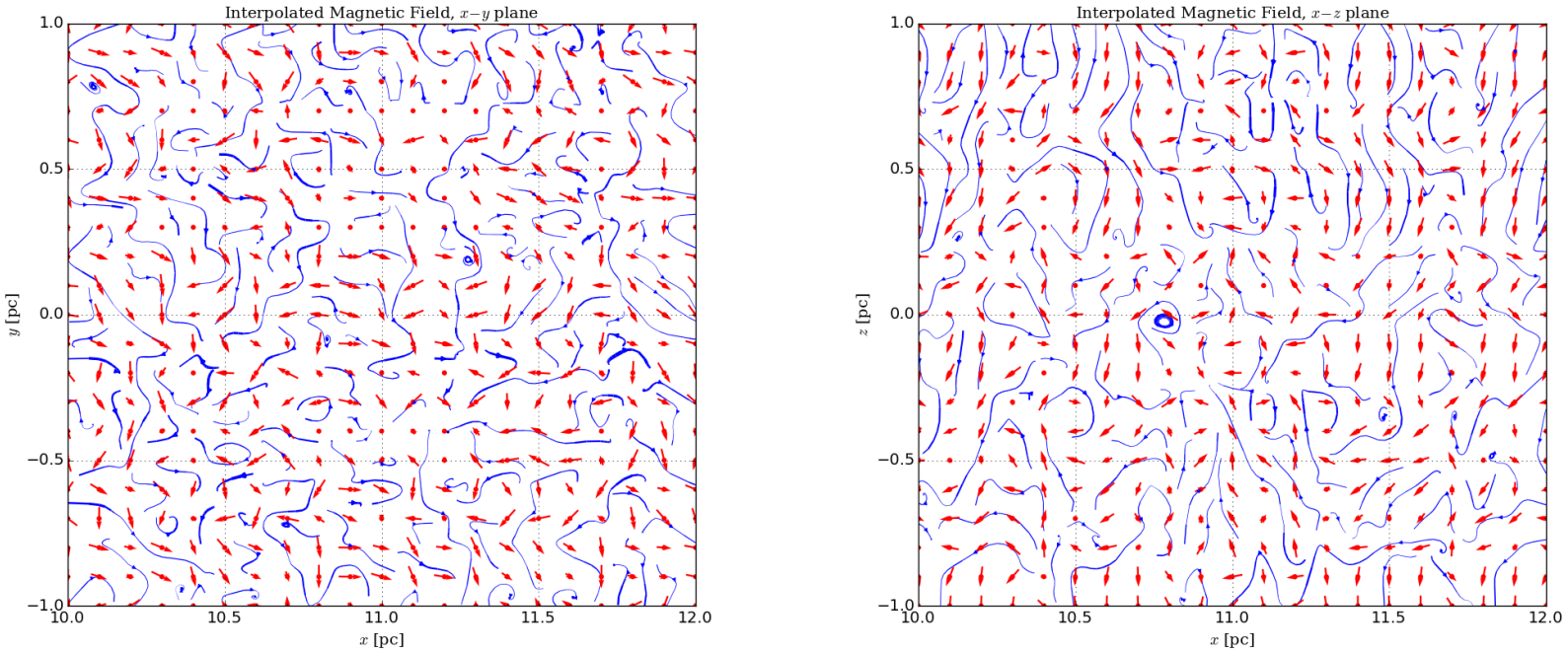

(a) (b)

Figure 4.3: *Sample interpolated values for the random magnetic field components. The red arrows are the random magnetic field grid vectors, $\vec{B}$ projected onto the x-y and x-z planes, and the blue streamlines are the interpolated field. The field has been interpolated in such a way as to match the vectors at each grid point while remaining divergence free ($\nabla \cdot \vec{B} = 0$).*

Table 4.3: Stopping Ranges for Various Particles onto Iron

$$R_{\text{incident}\rightarrow\text{target}} = R_0 \left(\frac{E}{1\ \text{keV}} \right)^{\alpha}$$

Incident[a,b]	Target	R_0 [nm]	α	Target	R_0 [nm]	α	Target	R_0 [nm]	α	Target	R_0 [nm]	α
e^-	Fe	5.1457	1.5662	FeO	6.3182	1.5918	Fe_2O_3	7.1477	1.5935	Fe_3O_4	7.2054	1.5993
H	Fe	7.8944	0.9667	FeO	9.6643	0.9550	Fe_2O_3	10.7754	0.9523	Fe_3O_4	11.0338	0.9528
He	Fe	4.6270	0.9490	FeO	5.4609	0.9632	Fe_2O_3	6.0215	0.9682	Fe_3O_4	6.1815	0.9669
C	Fe	2.2539	0.8049	FeO	2.5068	0.8319	Fe_2O_3	2.7192	0.8396	Fe_3O_4	2.8070	0.8369
N	Fe	2.0788	0.7794	FeO	2.3009	0.8047	Fe_2O_3	2.4935	0.8115	Fe_3O_4	2.5524	0.8131
O	Fe	1.9576	0.7627	FeO	2.1625	0.7851	Fe_2O_3	2.3461	0.7897	Fe_3O_4	2.4180	0.7884
Ne	Fe	1.7949	0.7360	FeO	1.9881	0.7520	Fe_2O_3	2.1468	0.7577	Fe_3O_4	2.2237	0.7551
Mg	Fe	1.6854	0.7061	FeO	1.8679	0.7221	Fe_2O_3	2.0332	0.7212	Fe_3O_4	2.1006	0.7183
Si	Fe	1.5552	0.6753	FeO	1.7466	0.6831	Fe_2O_3	1.9039	0.6824	Fe_3O_4	1.9618	0.6836
S	Fe	1.5055	0.6499	FeO	1.7055	0.6527	Fe_2O_3	1.8370	0.6594	Fe_3O_4	1.9132	0.6539
Ca	Fe	1.4367	0.6139	FeO	1.6412	0.6151	Fe_2O_3	1.7841	0.6196	Fe_3O_4	1.8487	0.6154
Fe	Fe	1.4116	0.5679	FeO	1.6464	0.5652	Fe_2O_3	1.8055	0.5646	Fe_3O_4	1.8499	0.5672
Ni	Fe	1.4014	0.5609	FeO	1.6536	0.5536	Fe_2O_3	1.8228	0.5530	Fe_3O_4	1.8722	0.5538
Zn	Fe	1.4128	0.5413	FeO	1.6734	0.5360	Fe_2O_3	1.8379	0.5367	Fe_3O_4	1.8874	0.5362
Kr	Fe	1.4238	0.5076	FeO	1.6968	0.5048	Fe_2O_3	1.8721	0.5052	Fe_3O_4	1.9276	0.5042

[a] - *Electron stopping ranges are based on outputs from the CASINO software (Drouin et al., 2007).*

[b] - *Ion stopping ranges are based on outputs from the SRIM software (Ziegler & Biersack, 1985; Ziegler et al., 2010).*

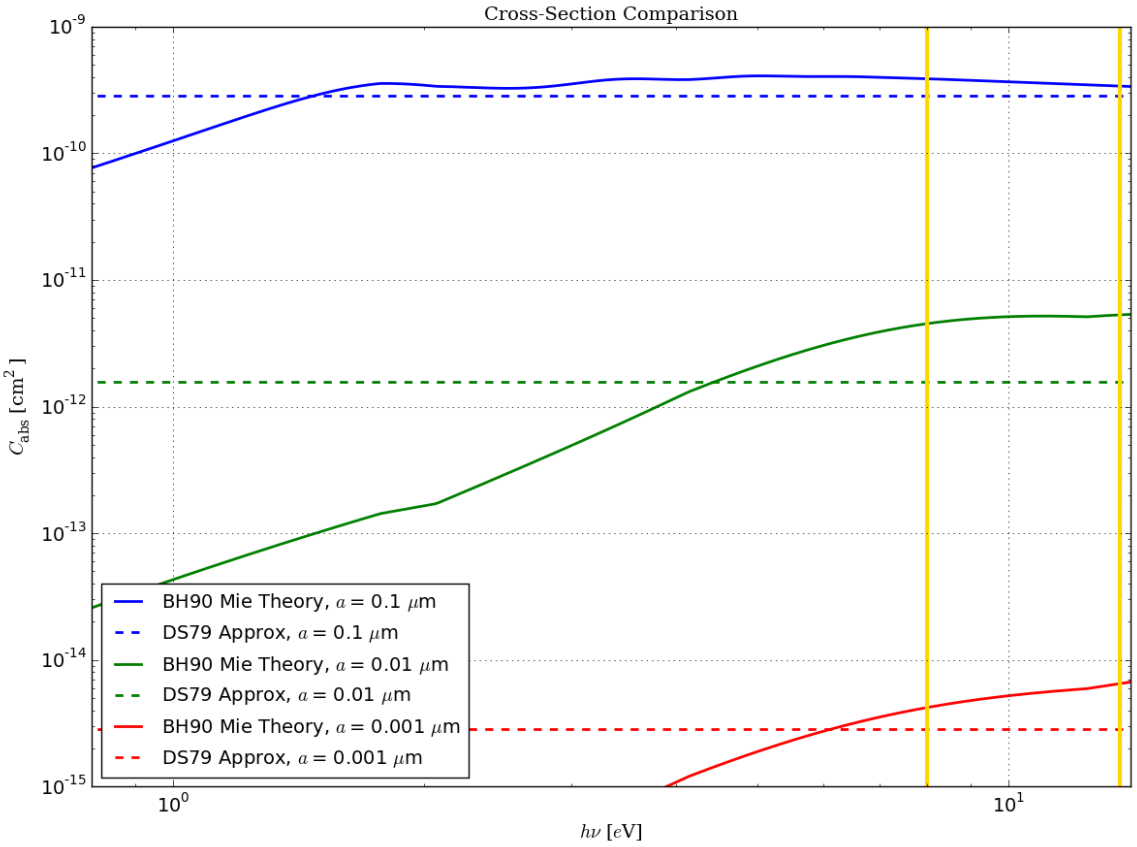

Figure 4.4: *Comparison for Absorption Cross-Section, $C_{\rm abs}$, calculations. The $C_{\rm abs}$ using Mie theory is shown with solid lines, and the approximation used by Draine & Salpeter (1979) is shown with dashed lines. For the energy range appropriate for the photoelectron emission ($\sim 8 - 13.6$ eV, shown with dotted, yellow, vertical lines), the approximation provides a reasonable approximation with far less calculations.*

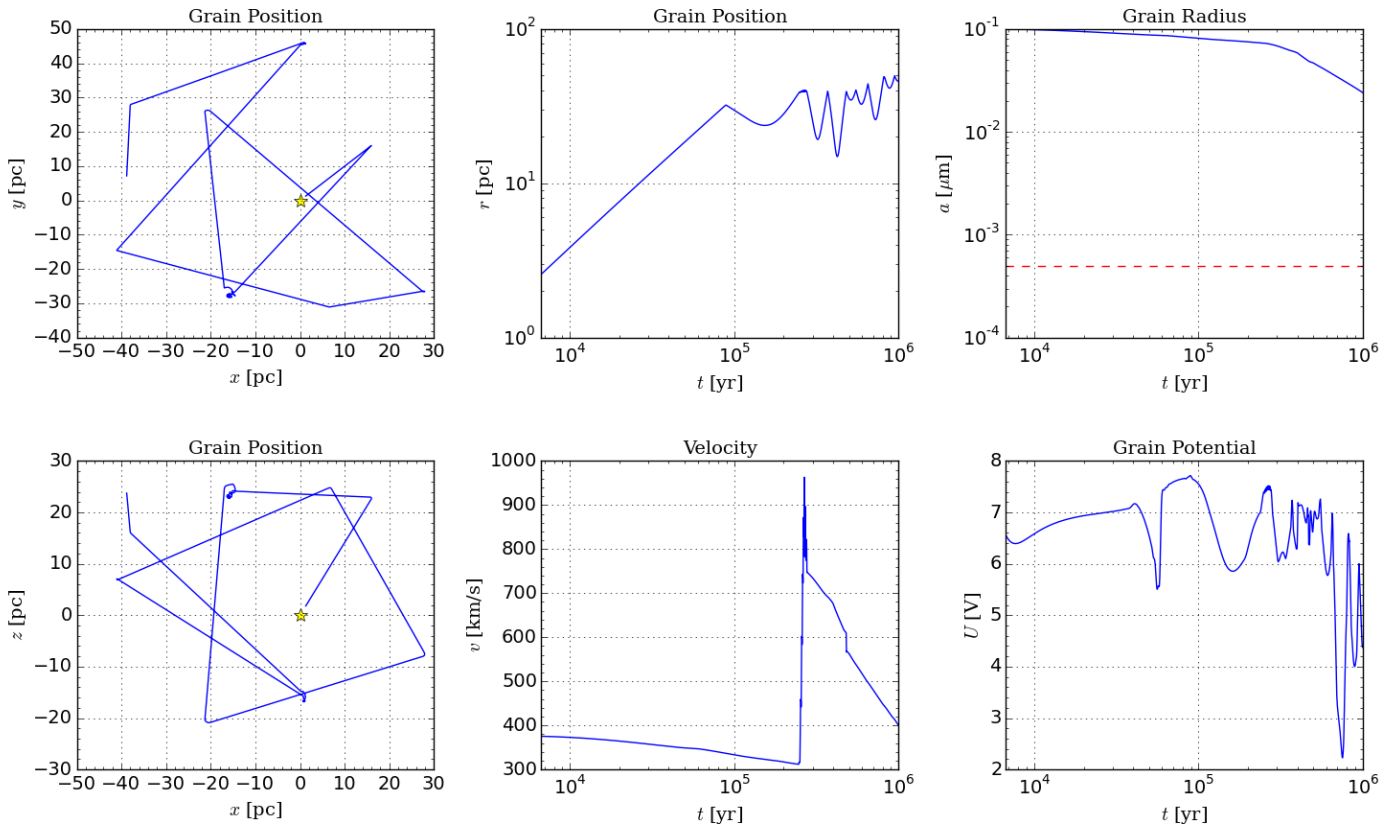

Figure 4.5: *Summary of grain parameters for a sample 0.1-μm metallic Fe-grain. The left panels are projections of the grain's positions onto the $x-y$- (upper) and $x-z$-planes (lower) with the yellow star representing the site of the SN. The upper center plot shows the grain's radial position. The first deflection occurs just before $t = 10^5$ yr, but at the second encounter ($t \approx 2.5 \times 10^5$ yr), the grain is temporarily trapped in the magnetic field, accelerated (sharp spike in lower center), and escapes at $t \approx 3 \times 10^5$ yr. This leads to the large kinetic sputtering shown by the sharp decline in the grain radius (upper right). Note, the grain potential (lower right) makes sharp fluctuations, but only varies a few Volts. The dashed, red line on the Grain Radius plot represents the sputtering limit; below this, the grain is assumed to have been destroyed.*

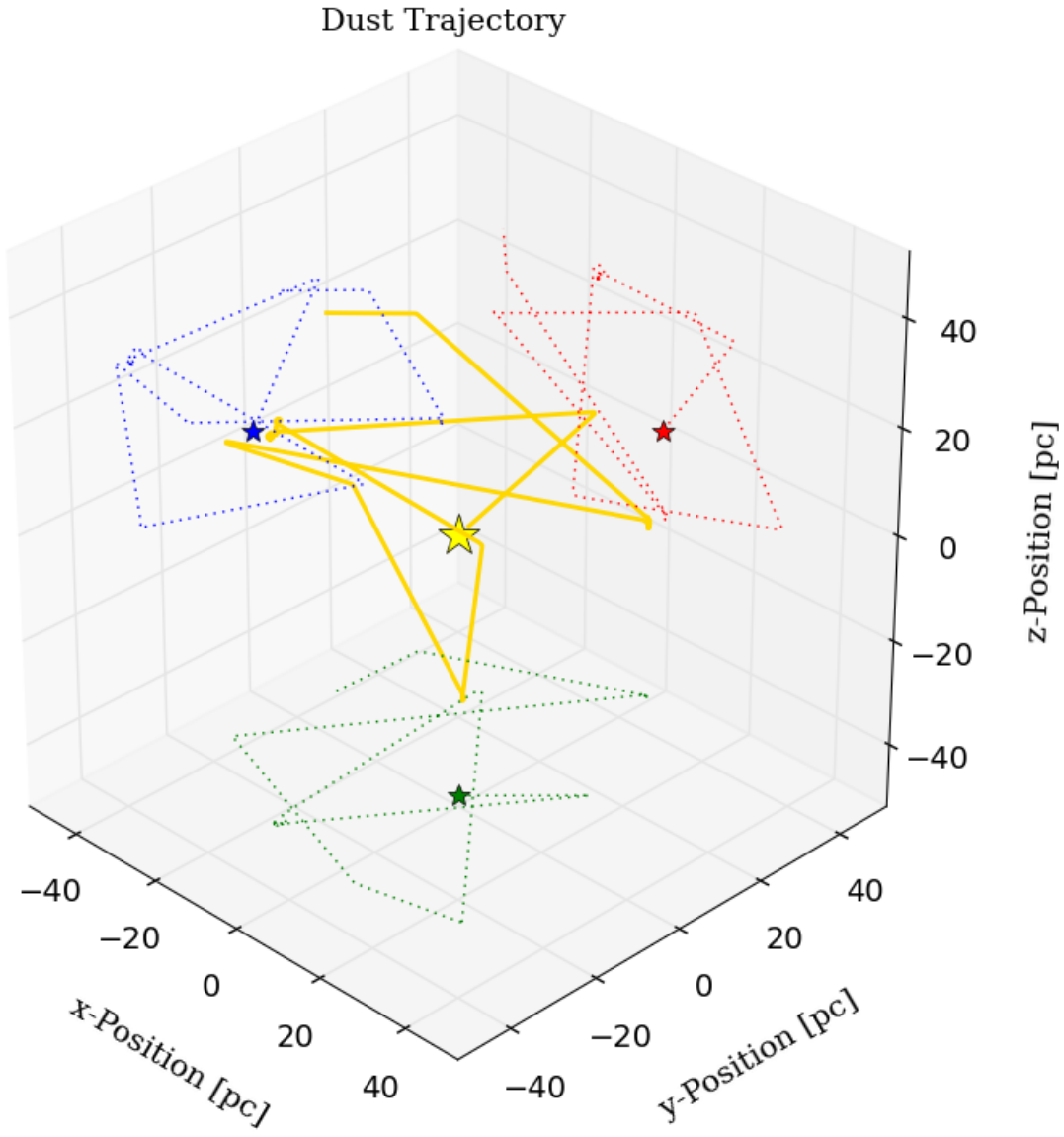

Figure 4.6: *3-dimensional plot of a sample 0.1-μm metallic Fe-grain. The yellow lines are the 3-D plot of the grain trajectory with the green, red, and blue lines showing the $x-y$-, $x-z$-, and $y-z$-planes respectively. The stars represent the location of the SN.*

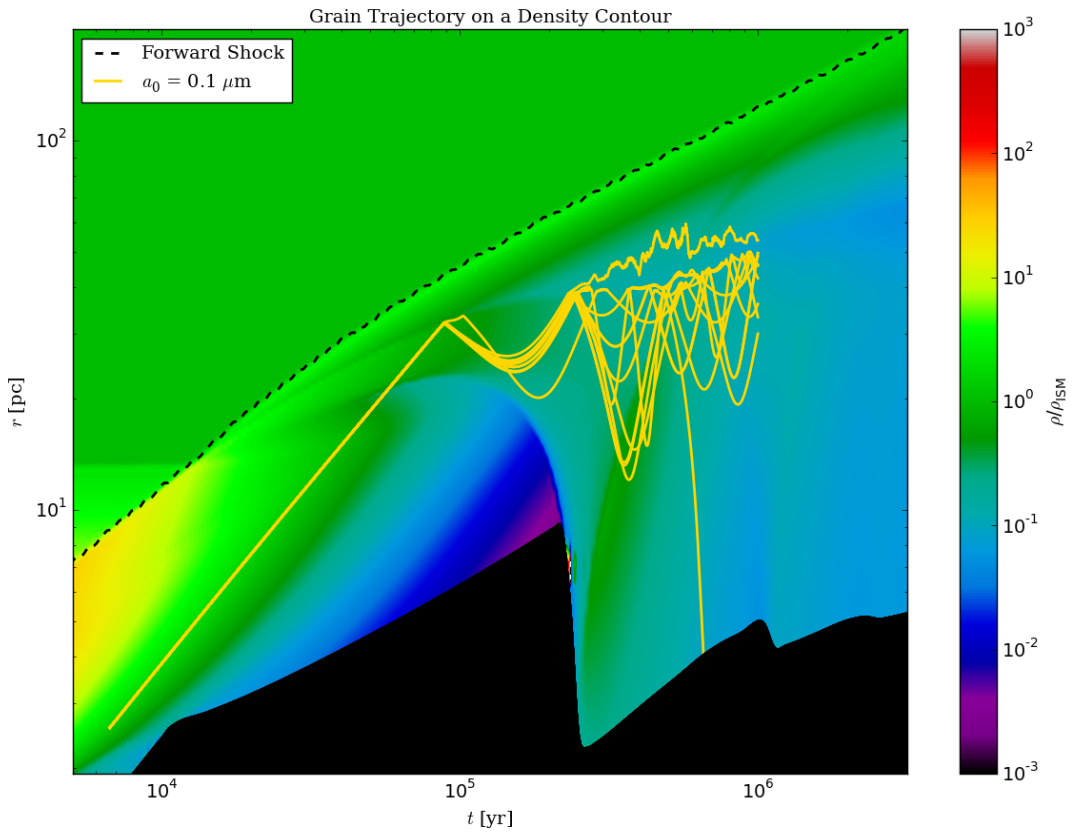

Figure 4.7: *Multiple trajectories of metallic Fe-grains on a density contour. Ten trajectories (plotted in yellow) are shown with an initial grain radius of $a = 0.1$ μm; note that most grains remain in the $20 - 40$ pc region while bouncing within the shell. The furtherest trajectory (appears as a noisy trajectory) shows oscillations indicative of trapping within layers of magnetic fields, and the shortest trajectory shows the grain bouncing back into the inner ejecta. The forward shock is shown with the dashed, black curve, and the inner most limit of the hydrodynamic simulations are shown with the blacked-out region at the bottom of the chart.*

Chapter 5

Conclusions and Future Work

The preceding material shows that the Earth has been showered with SN shrapnel at least once, maybe twice. The progenitor was mostly likely a SN, specifically an CCSN. As the material passed through the Solar System, it experienced little deflection until reaching the atmosphere, where it was vaporized and distributed across the globe. The final distribution on the ocean floor is dependent on upper atmosphere and oceanic processes.

Within the SNR, dust survival is highly dependent on where it forms. The location of birth determines the composition of the dust grain, when the reverse shock passes, and the initial velocity of the grain. The composition determines the grain's density and charging properties. The inclusion of R-T instabilities are important as these affect the position of the reverse shock, allowing it to pass sooner, thereby halting grain formation earlier. The inclusion of the magnetic field within the shocked ISM material is also important because when charged dust grains reach the shocked ISM they will be reflected, trapped, and/or accelerated by the magnetic fields. In short, SN dust traveled a rough road to reach Earth.

Clearly, there are a number of questions left to be answered. Some can/will be addressed prior to publication of the material in Chapter 4:

1) How does the propagation of dust containing $^{26}Al_2O_3$ or ^{53}MnS differ from dust containing ^{60}Fe?

2) How does the propagation vary without the H/He envelope around the ECSN?

3) How does the propagation/magnetic field vary with an average ISM density?

4) What would be the minimum dust grain size required to escape the SNR?

5) What is the propagation of pre-SN dust from the SAGB phase?

Follow-on work from material in Chapter 4 would extend the hydrodynamic code to include the transition of the SNR into snow-plow phase (possibly into the fade-away phase). Grain processing would be adapted to include grain shattering, grain heating/sublimation, and field emission. Examination of nucleosynthesis in larger

progenitors (e.g., 15-$M_{\odot}$, 19-$M_{\odot}$, etc. CCSN, Rauscher et al., 2002) could also be performed.

With regards to open questions of the field, one future focus should be looking for additional isotopes. The lack of detection for ^{26}Al and ^{244}Pu can be explained with an ECSN progenitor, but the detection of additional isotopes can tell us a great deal about SN nucleosynthesis, dust formation, and the distance to the source. A first examination should be ^{53}Mn, with ^{41}Ca in follow-on measurements. Although some ^{53}Mn is produced in the outer portion of ECSN ejecta, the majority comes from deeper in the ejecta (even deeper than ^{60}Fe), and most SNe produce roughly the same amount of ^{53}Mn as ^{60}Fe. AMS has the capability to make very precise measurements of ^{53}Mn (Poutivtsev et al., 2010), and these measurements were mentioned by Feige et al. (2013), but have yet to be completed/published.

Additional work can be done with the deposition of dust onto the Moon. The lack of an appreciable atmosphere makes the lunar surface a possible means of determining the direction to the source of ^{60}Fe, but a number of properties still need to be characterized: after impact, how much of the vaporized dust will be ejected versus remain on the surface; how deeply will the ^{60}Fe dust grains penetrate the lunar surface; how does the composition of the lunar surface affect deposition? In addition, if the dust reflection found in Chapter 4 actually occurs, this would alter the directionality expected from lunar samples, and the angular distribution of arriving dust grains would need to be determined. Answering these questions will allow us to better apply the lunar measurements of Fimiani et al. (2016).

One major question is where did the SN occur: Sco-Cen, Tuc-Hor, or somewhere else? The Sco-Cen association has more stars, several are massive enough to produce a SN, but the association is very far away ($\gtrsim$ 100 pc). Tuc-Hor has fewer stars, none are currently large enough to produce a SN (there could have been in the past, however), but the association is fairly close ($\sim$ 60 pc). Identification of the source

of the ^{60}Fe would tell us about dust propagation (and potentially the magnetic field within the Local Bubble). Lunar samples have already been mentioned as a possible means of determining direction to the source. Additionally, just before a star explodes, a significant of portion of the star's Fe-core is dissociated, producing huge amounts of neutrinos that help drive the explosion. Most of the energy released in a SN is deposited into neutrinos (about a hundred times the kinetic component). Because SNe are essentially neutrino bombs, we could potentially use a technique originally suggested for the solar neutrino problem (Cowan & Haxton, 1982). The neutrinos from the SN would travel to (and through the) Earth largely undisturbed, but some will interact with terrestrial molybdenum (Mo) producing radioactive technetium (Tc). By measuring the concentration of Tc to Mo, and subtracting the background produced by solar neutrinos, it may be possible to compare the estimated neutrino flux from distances to Sco-Cen and Tur-Hor (Nguyen & Johnson, 2007).

The detection of the SN 2.2 Myr ago and possibly another $\sim$ 7.5 Myr ago points to the deeper question of how often does Earth get splashed with SN material? There are no near-Earth candidates today, but in the past there has been least one, maybe two, that we know of but probably more we do not. Understanding the near-Earth SN rate and how it relates to the broader galactic SN rate, will tell us about the star formation history of the galaxy, the SN history of the Local Bubble, and potentially the mass extinction rate on Earth.

Something to remember about SNe is that even though they are incredibly destructive, they are also essential to our existence. The production of heavy elements are essential life. We can rest assured that our demise will not come at the hands of a SN and marvel at the their ability to do what ancient alchemists only dreamed of: make gold from thin air. The existence of near-Earth SNe provide a means where we can study directly some of the most spectacular galactic events. They also tell us we are not isolated within this Solar System, and that objects from light-years away can

reach us (just like something out of a disaster movie!).

References

Abt, H. A. 2011, AJ, 141, 165

Adams, S. M., Kochanek, C. S., Beacom, J. F., Vagins, M. R., & Stanek, K. Z. 2013, ApJ, 778, 164

Alvarez, L., Alvarez, W., Asaro, F., & Michel, H. 1980, Sci, 208, 4448, 1095-1108

Ammosov, A. E., Berezhko, E. G., Konstantinov, A. N., et al. 1991, Akademiia Nauk SSSR Izvestiia Seriia Fizicheskaia, 55, 2037

Andersen, H. H., & Bay, H. L. 1981, Sputtering by Particle Bombardment I: Physical Sputtering of Single-Element Solids, 145

Archer, D. E., & Johnson, K. 2000, Global Biogeochemical Cycles, 14, 269

Athanassiadou, T. & Fields, B. D. 2011, New Astron., 16, 4, 229-241

Atri, D., & Melott, A. L. 2014, Astroparticle Physics, 53, 186

Balsara, D., Benjamin, R. A., & Cox, D. P. 2001, ApJ, 563, 800

Barkan, A., D'angelo, N., & Merlino, R. L. 1994, Physical Review Letters, 73, 3093

Beech, M. 2011, Ap&SS, 336, 287

Benítez, N., Maíz-Apellániz, J., & Canelles, M. 2002, Physical Review Letters, 88, 081101

Berger, E., Fong, W., & Chornock, R. 2013, ApJ, 774, LL23

Berghöfer, T. W. & Breitschwerdt, D. 2002, A&A, 390, 299-306

Bignami, G. F., & Caraveo, P. A. 1996, ARA&A, 34, 331

Binns, W. R., Israel, M. H., Christian, E. R., et al. 2016, Science, 352, 677

Biscaro, C., & Cherchneff, I. 2014, A&A, 564, A25

Biscaro, C., & Cherchneff, I. 2016, A&A, 589, A132

Bishop, S. & Egli, R. 2011, Icarus, 212, 2, 960-962

Blondin, J. M., & Ellison, D. C. 2001, ApJ, 560, 244

Blondin, J. M., Wright, E. B., Borkowski, K. J., & Reynolds, S. P. 1998, ApJ, 500, 342

Blondin, J. M. 2001, Young Supernova Remnants, 565, 59

Bocchio, M., Marassi, S., Schneider, R., et al. 2016, A&A, 587, A157

Bohdansky, J. 1984, Nuclear Instruments and Methods in Physics Research B, 2, 587

Bohren, C. F., & Huffman, D. R. 1983, New York: Wiley, 1983,

Book, D. L. 1994, Shock Waves, 4, 1, 1-10

Book, D. L. 1994, Shock Waves, 4, 1, 1-10

Boyd, P. W., & Ellwood, M. J. 2010, Nature Geoscience, 3, 675

Breitschwerdt, D., de Avillez, M. A., Feige, J., & Dettbarn, C. 2012, Astronomische Nachrichten, 333, 486

Breitschwerdt, D., Feige, J., Schulreich, M. M., et al. 2016, Nature, 532, 73

Bruland, K. W., Orians, K. J., & Cowen, J. P. 1994, Geochim. Cosmochim. Acta, 58, 3171

Burns, J.A., Lamy, P.L., & Soter, S. 1979, Icarus, 40, 1

Castor, J., McCray, R., & Weaver, R. 1975, ApJ, 200, L107

Cherchneff, I., & Dwek, E. 2009, ApJ, 703, 642

Cherchneff, I., & Dwek, E. 2010, ApJ, 713, 1

Cherchneff, I., & Sarangi, A. 2011, The Molecular Universe, 280, 228

Cherchneff, I. 2013, EAS Publications Series, 60, 175

Chevalier, R. A., Blondin, J. M., & Emmering, R. T. 1992, ApJ, 392, 118

Chevalier, R. A. 1974, ApJ, 188, 501

Chevalier, R. A. 1982, ApJ, 258, 790

Chmeleff, J., von Blanckenburg, F., Kossert, K., & Jakob, D. 2010, Nuclear Instruments and Methods in Physics Research B, 268, 192

Chow, V. W., Mendis, D. A., & Rosenberg, M. 1993, J. Geophys. Res., 98, 19

Chu, Y.-H. 2008, IAUS, 250, 341-354

Cintala, M. J. 1992, J. Geophys. Res., 97, 947-973

Collette, A., Sternovsky, & Z., & Horanyi, M. 2014, Icarus, 227, 89-93

Cook, D. L., Berger, E., Faestermann, T., et al. 2009, LPI, 40, 1129

Cowan, G. A., & Haxton, W. C. 1982, Science, 216, 51

Cox, D. P., & Helenius, L. 2003, ApJ, 583, 205

Lide, D. R. 2008, CRC Handbook of chemistry and physics: a ready-reference book of chemical and physical data, 89th edition. Ed. David R. Lide. Boca Raton, FL: CRC Press, 2008,

Cremonese, G., Borin, P., Lucchetti, A., Marzari, F., & Bruno, M. 2013, A&A, 551, A27

Croot, P. L., Streu, P., & Baker, A. R. 2004, Geophys. Res. Lett., 31, L23S08

Dartnell, L. R. 2011, Astrobiology, 11, 551

Davies, M. E., & Colvin, T. R. 2000, J. Geophys. Res., 105, 20277

Davies, M. E., Colvin, T. R., & Meyer, D. L. 1987, J. Geophys. Res., 92, 14177

Dhomse, S. S., Saunders, R. W., Tian, W., Chipperfield, M. P., & Plane, J. M. C. 2013, Geophys. Res. Lett., 40, 4454

Doherty, C. L., Gil-Pons, P., Lau, H. H. B., Lattanzio, J. C., & Siess, L. 2014, MNRAS, 437, 1, 195-214

Dragt, A. J. 1965, Reviews of Geophysics and Space Physics, 3, 255

Draine, B. T., & Salpeter, E. E. 1979, ApJ, 231, 77

Draine, B. T., & Sutin, B. 1987, ApJ, 320, 803

Draine, B. T. 2003, ARA&A, 41, 241

Draine, B. T. 2011, Physics of the Interstellar and Intergalactic Medium. Princeton University Press, 2011. ISBN: 978-0-691-12214-4

Drouin, D., Couture, A. R., Joly, D., et al. 2007, Scanning, 29, 92

Duffell, P. C. 2016, ApJ, 821, 76

Dutkiewicz, S., Follows, M. J., & Parekh, P. 2005, Global Biogeochemical Cycles, 19, GB1021

Dutkiewicz, S., Ward, B. A., Monteiro, F., & Follows, M. J. 2012, Global Biogeochemical Cycles, 26, GB1012

Dwek, E., & Arendt, R. G. 1992, ARA&A, 30, 11

Dwek, E., Foster, S. M., & Vancura, O. 1996, ApJ, 457, 244

Dwek, E. 2016, arXiv:1605.01957

Ejzak, L. M., Melott, A. L., Medvedev, M. V., & Thomas, B. C. 2007, ApJ, 654, 373

Ellis, J., & Schramm, D. N. 1995, Proceedings of the National Academy of Science, 92, 235

Ellis, J., Fields, B. D., & Schramm, D. N. 1996, ApJ, 470, 1227

Faherty, J., Walter, F. M., & Anderson, J. 2007, Ap&SS, 308, 225

Feige, J., Wallner, A., Winkler, S. R., et al. 2012, PASA, 29, 2, 109-114

Feige, J., Wallner, A., Fifield, L. K., et al. 2013, EPJWC, 63, 03003

Feige, Jenny. "The connection between the local bubble and the ^{60}Fe anomaly in the deep sea hydrogenetic ferromanganese crust." Master's thesis, University of Vienna, 2010. `http://othes.univie.ac.at/8920/`

Feige, J. "Supernova-Produced Radionuclides in Deep-Sea Sediments Measured with AMS." Doctoral Dissertation, University of Vienna, 2014. `http://othes.univie.ac.at/35089/`

Feng, W., Marsh, D. R., Chipperfield, M. P., et al. 2013, Journal of Geophysical Research (Atmospheres), 118, 9456

Field, G. B. 1975, The Dusty Universe, 89

Fields, B. D., & Ellis, J. 1999, NewA, 4, 6, 419-430

Fields, B. D., Hochmuth, K. A., & Ellis, J. 2005, ApJ, 621, 2, 902-907

Fields, B. D., Athanassiadou, T., & Johnson, S. R. 2008, ApJ, 678, 1, 549-562

Fields, B. D. 2004, New Astron. Rev., 48, 119

Fimiani, L., Cook, D. L., Faestermann, T., et al. 2012, LPI, 43, 1279

Fimiani, L., Cook, D. L., Faestermann, T., et al. 2014, LPI, 45, 1778

Fimiani, L., Cook, D. L., Faestermann, T., et al. 2016, Physical Review Letters, 116, 151104

Fitoussi, C., Raisbeck, G. M., Knie, K., et al. 2008, PhRvL., 101, 12, 121101

Fitting, H.-J. 1974, Physica Status Solidi Applied Research, 26, 525

Florinski, V., Pogorelov, N. V., Zank, G. P., Wood, B. E., & Cox, D. P. 2004, ApJ, 604, 700

Fremling, C., Sollerman, J., Taddia, F., et al. 2016, arXiv:1606.03074

Freytag, B., Steffen, M., & Dorch, B. 2002, Astronomische Nachrichten, 323, 213

Frisch, P. C., Andersson, B.-G., Berdyugin, A., et al. 2012, ApJ, 760, 106

Frisch, P. C. 1995, Space Sci. Rev., 72, 499

Fry, B. J., Fields, B. D., & Ellis, J. R. 2015, ApJ, 800, 71

Fry, B. J., Fields, B. D., & Ellis, J. R. 2016, arXiv:1604.00958

Fuchs, B., Breitschwerdt, D., de Avillez, M. A., Dettbarn, C., & Flynn, C. 2006, MNRAS, 373, 3, 993-1003

Fujita, Y., Ohira, Y., & Takahara, F. 2010, ApJ, 712, L153

Gehrels, N., Laird, C. M., Jackman, C. H., et al. 2003, ApJ, 585, 1169

Goriely, S., Bauswein, A., & Janka, H.-T. 2011, ApJ, 738, 2, L32

Grard, R. J. L. 1973, J. Geophys. Res., 78, 2885

Gray, M. D., & Edmunds, M. G. 2004, MNRAS, 349, 491

Green, D. A. 2000, IAU Joint Discussion, 6,

Gustafson, B.A.S. 1994, Annual Review of Earth and Planetary Sciences, 22, 553

Haid, S., Walch, S., Naab, T., et al. 2016, MNRAS,

Herwig, F. 2005, ARA&A, 43, 435

Hoffman, R. D., Müller, B., & Janka, H.-T. 2008, ApJ, 676, L127

Hoppe, P., & Zinner, E. 2000, J. Geophys. Res., 105, 10371

Inoue, T., Yamazaki, R., & Inutsuka, S.-i. 2009, ApJ, 695, 825

Jackson, J. D. 1998, Classical Electrodynamics, 3rd Edition, by John David Jackson, pp. 832. ISBN 0-471-30932-X. Wiley-VCH , July 1998., 832

Janev, R. K., Ralchenko, Y. V., Kenmotsu, T., & Hosaka, K. 2001, Journal of Nuclear Materials, 290, 104

Janka, H.-T., Müller, B., Kitaura, F. S., & Buras, R. 2008, A&A, 485, 199

Janka, H.-T., Melson, T., & Summa, A. 2016, arXiv:1602.05576

Ji, S., Oh, S. P., Ruszkowski, M., & Markevitch, M. 2016, arXiv:1603.08518

Jickells, T. D., An, Z. S., Andersen, K. K., et al. 2005, Science, 308, 67

Jones, A. P., Tielens, A. G. G. M., & Hollenbach, D. J. 1996, ApJ, 469, 740

Jones, S., Roepke, F. K., Pakmor, R., et al. 2016, arXiv:1602.05771

Kachelrieß, M., Neronov, A., & Semikoz, D. V. 2015, Physical Review Letters, 115, 181103

Katsiaris, G. A., & Psillakis, Z. M. 1987, Ap&SS, 132, 165

Kimura, H., & Mann, I. 1998, ApJ, 499, 454

Kivelson, M. G., & Russell, C. T. 1995, Introduction to Space Physics, Edited by Margaret G. Kivelson and Christopher T. Russell, pp. 586. ISBN 0521451043. Cambridge, UK: Cambridge University Press, April 1995.,

Klein, R. I., McKee, C. F., & Colella, P. 1994, ApJ, 420, 213

Knie, K., Korschinek, G., Faestermann, T., et al. 1999, PhRvL, 83, 1, 18-21

Knie, K., Korschinek, G., Faestermann, T., et al. 2004, PhRvL, 93, 17, 171103

Korschinek, G., Faestermann, T., Knie, K. & Schmidt, C. 1996, Radiocarbon, 38, 68

Korschinek, G., Bergmaier, A., Faestermann, T., et al. 2010, Nuclear Instruments and Methods in Physics Research B, 268, 187

Kozasa, T., Nozawa, T., Tominaga, N., et al. 2009, Cosmic Dust - Near and Far, 414, 43

Lafon, J.-P. J., Lamy, L., & Millet, J. 1981, A&A, 95, 295

Laming, J. M., & Hwang, U. 2003, ApJ, 597, 347

Langevin, Y., & Arnold, J. R. 1977, AREPS, 5, 449-489

Lattimer, J. M., & Schramm, D. N. 1974, ApJ, 192, L145

LefèVre, N., & Watson, A. J. 1999, Global Biogeochemical Cycles, 13, 727

Li, L.-X., & Paczyński, B. 1998, ApJ, 507, L59

Limongi, M., & Chieffi, A. 2006, ApJ, 647, 1, 483-500

Linde, T.J., & Gombosi, T.I. 2000, J. Geophys. Res., 105, 10411

Looney, L. W., Tobin, J. J., & Fields, B. D. 2006, ApJ, 652, 1755

Mamajek, E. E. 2016, IAU Symposium, 314, 21

Mathis, J.S., Rumpl, W., & Nordsieck, K.H. 1977, ApJ, 217, 425

Matsunami, N., Yamamura, Y., Itikawa, Y., et al. 1984, Atomic Data and Nuclear Data Tables, 31, 1

Matsuura, M., Dwek, E., Meixner, M., et al. 2011, Sci, 333, 6047, 1258-1261

McCullough, P. R., Fields, B. D., & Pavlidou, V. 2002, ApJ, 576, L41

McKee, C. F., & Draine, B. T. 1991, Science, 252, 397

McKee, C. F., Hollenbach, D. J., Seab, G. C., & Tielens, A. G. G. M. 1987, ApJ, 318, 674

McNally, C. P. 2011, MNRAS, 413, L76

Melott, A. L., & Thomas, B. C. 2011, Astrobiology, 11, 343

Metzger, B. D., Martínez-Pinedo, G., Darbha, S., et al. 2010, MNRAS, 406, 2650

Meynadier, L., Valet, J.-P., Bassinot, F. C., Shackleton, N. J., & Guyodo, Y. 1994, E&PSL, 126, 109-127

Micelotta, E. R., Dwek, E., & Slavin, J. D. 2016, A&A, 590, A65

Moore, J. K., & Braucher, O. 2008, Biogeosciences, 5, 631

Moore, J. K., Doney, S. C., & Lindsay, K. 2004, Global Biogeochemical Cycles, 18, GB4028

Murray, N., Weingartner, J.C., & Capobianco, C. 2004, ApJ, 600, 804

Nadezhin, D. K. 1985, Ap&SS, 112, 225

Nath, B. B., Laskar, T., & Shull, J. M. 2008, ApJ, 682, 1055-1064

Nava, D. F., & Philpotts, J. A. 1973, Ge Co A, 37, 4, 963-973

Niciejewski, R., Skinner, W., Cooper, M., et al. 2011, Journal of Geophysical Research (Space Physics), 116, A05302

Nishiizumi, K., Imamura, M., Kohl, C. P., et al. 1979, E&PSL, 44, 3, 409-419

Nishiizumi, K., Arnold, J. R., Kubik, P. W., & Sharma, P. 1990, LPI, 21, 895

Nomoto, K., Thielemann, F.-K., & Yokoi, K. 1984, ApJ, 286, 644-658

Northrop, T. G., & Morfill, G. E. 1984, Advances in Space Research, 4, 63

Nozawa, T., Kozasa, T., Umeda, H., Maeda, K., & Nomoto, K. 2003, ApJ, 598, 785

Nozawa, T., Kozasa, T., & Habe, A. 2006, ApJ, 648, 435

Nozawa, T., Kozasa, T., Habe, A., et al. 2007, ApJ, 666, 955

Nguyen, V. T., & Johnson, C. W. 2007, Astroparticle Physics, 27, 233

Ostriker, J. P., & McKee, C. F. 1988, Reviews of Modern Physics, 60, 1

Padmanabhan, T. 2000, Theoretical Astrophysics - Volume 1, Astrophysical Processes, by T. Padmanabhan, pp. 622. Cambridge University Press, December 2000. ISBN-10: 0521562406. ISBN-13: 9780521562409. LCCN: QB461 .P33 2000, 622

Padmanabhan, T. 2001, Theoretical Astrophysics - Volume 2, Stars and Stellar Systems, by T. Padmanabhan, pp. 594. Cambridge University Press, July 2001. ISBN-10: 0521562414. ISBN-13: 9780521562416. LCCN: QB801 .P23 2001, 594

Parekh, P., Follows, M. J., & Boyle, E. 2004, Global Biogeochemical Cycles, 18, GB1002

Parker, E. N. 1958, ApJ, 128, 664

Parker, E. N. 1963, New York, Interscience Publishers, 1963.

Paul, M., Valenta, A., Ahmad, I., et al. 2001, ApJ, 558, 2, L133-L135

Paul, M., Valenta, A., Ahmad, I., et al. 2003, NuPhA, 719, C29-C36

Paul, M., Valenta, A., Ahmad, I., et al. 2007, J. Radioanal Nucl Chem., 272, 2, 243-245

Petit, P., Aurière, M., Konstantinova-Antova, R., et al. 2013, Lecture Notes in Physics, Berlin Springer Verlag, 857, 231

Piran, T., Korobkin, O., & Rosswog, S. 2014, arXiv:1401.2166

Plait, P. C. 2009, Death From the Skies!: The Science Behind the End of the World (New York, NY: Penguin Books)

Plane, J. M. C., Feng, W., Dawkins, E. C. M. 2015, Chemical Reviews, 115(10), 4497-4541

Plane, J. M. C. 2012, Chemical Society Reviews, Vol. 41, p. 6507-6518, 2012, 41, 6507

Poelarends, A. J. T., Herwig, F., Langer, N., & Heger, A. 2008, ApJ, 675, 614-625

Pollack, J. B., Hollenbach, D., Beckwith, S., et al. 1994, ApJ, 421, 615

Pollack, J.B., Hollenbach, D., Beckwith, S., et al. 1994, ApJ, 421, 615

Poutivtsev, M., Dillmann, I., Faestermann, T., et al. 2010, NIMPB, 268, 7-8, 756-758

Preibisch, T., & Mamajek, E. 2008, Handbook of Star Forming Regions, Volume II, 5, 235

Pumo, M. L., Turatto, M., Botticella, M. T., et al. 2009, ApJ, 705, L138

Pumo, M. L. 2010, Memorie della Societa Astronomica Italiana Supplementi, 14, 115

Raisbeck, G. M., Yiou, F., Bourles, D., Lorius, C., & Jouzel, J. 1987, Nature, 326, 273

Raisbeck, G., Tran, T., Lunney, D., et al. 2007, NIMPB, 259, 1, 673-676

Rauscher, T., Heger, A., Hoffman, R. D., & Woosley, S. E. 2002, ApJ, 576, 1, 323-348

Rho, J., Kozasa, T., Reach, W. T., et al. 2008, ApJ, 673, 271-282

Ruderman, M. A. 1974, Science, 184, 1079

Rugel, G., Faestermann, T., Knie, K., et al. 2009, Physical Review Letters, 103, 072502

Sarangi, A., & Cherchneff, I. 2013, ApJ, 776, 107

Sarangi, A., & Cherchneff, I. 2015, A&A, 575, A95

Saunders, R. W., Dhomse, S., Tian, W. S., Chipperfield, M. P., & Plane, J. M. C. 2012, Atmospheric Chemistry & Physics, 12, 4387

Savchenko, V., Kachelrieß, M., & Semikoz, D. V. 2015, ApJ, 809, L23

Scalo, J. M., Haff, P. K., Switkowski, Z. E., & Tombrello, T. A. 1977, Physics Letters B, 70, 137

Schindewolf OH. 1954. Ueber die moeglichen Ursachen der grossen erdgeschichtlichen Faunenschnitte. Neues Jahrb. Geol. Palaeontol. Monatshefte 10:45765

Sedov, L. I. 1959, Similarity and Dimensional Methods in Mechanics, New York: Academic Press, 1959,

Seitenzahl, I. R., Ciaraldi-Schoolmann, F., Röpke, F. K., et al. 2013, MNRAS, 429, 1156

Shklovskii, I. S., & Sagan, C. 1966, Intelligent life in the universe by I. S. Shklovskii [and] Carl Sagan. Authorized translation by Paula Fern. San Francisco: Holden-Day, 1966.

Shklovskij, I. S. 1969, Supernovae (New York, NY: Interscience Publishers)

Shu, F. H. 1992, The physics of astrophysics. Volume II: Gas dynamics., by Shu, F.H. University Science Books, Mill Valley, CA (USA), 1992, ISBN 0-935702-65-2

Shukla, P. K., & Mamun, A. A. 2002, Introduction to dusty plasma physics P. K. Shukla, A. A. Mamun. Bristol; Philadelphia: Institute of Physics Publishing, c2002. (Series in plasma physics),

Shull, J. M. 1977, ApJ, 215, 805

Shull, J. M. 1978, ApJ, 226, 858

Siess, L. 2010, A&A, 512, A10

Sigmund, P. 1981, Sputtering by Particle Bombardment I: Physical Sputtering of Single-Element Solids, 9

Silvia, D.W., Smith, B.D., & Shull, J.M. 2010, ApJ, 715, 1575

Silvia, D.W., Smith, B.D., & Shull, J.M. 2012, ApJ, 748, 12

Slavin, J. A., Smith, E. J., Sibeck, D. G., Baker, D. N., & Zwickl, R. D. 1985, J. Geophys. Res., 90, 10875

Slavin, J. D., Frisch, P. C., Heerikhuisen, J., et al. 2010, Twelfth International Solar Wind Conference, 1216, 497

Smartt, S. J., Eldridge, J. J., Crockett, R. M., & Maund, J. R. 2009, MNRAS, 395, 1409

Smith, D. S., Scalo, J., & Wheeler, J. C. 2004, Icarus, 171, 229

Spitzer, L., Jr., & Jenkins, E. B. 1975, ARA&A, 13, 133-164

Sterken, V. J., Altobelli, N., Kempf, S., et al. 2012, A&A, 538, A102

Sterken, V. J., Altobelli, N., Kempf, S., et al. 2013, A&A, 552, A130

Symbalisty, E., & Schramm, D. N. 1982, Astrophys. Lett., 22, 143

Tanvir, N. R., Levan, A. J., Fruchter, A. S., et al. 2013, Nature, 500, 547

Taylor, G. 1950, Proceedings of the Royal Society of London Series A, 201, 159

Tetzlaff, N., Torres, G., Neuhäuser, R., & Hohle, M. M. 2013, MNRAS, 435, 879

Thomas, B. C., Melott, A. L., Field, B. D., & Anthony-Twarog, B. J. 2008, Astrobiology, 8, 9

Thomas, B. C., Engler, E. E., Kachelrieß, M., et al. 2016, arXiv:1605.04926

Tielens, A. G. G. M., Seab, C. G., Hollenbach, D. J., & McKee, C. F. 1987, ApJ, 319, L109

Truelove, J. K., & McKee, C. F. 1999, ApJS, 120, 299

Tsyganenko, N. A. 1989, Planet. Space Sci., 37, 5

Tur, C., Heger, A., & Austin, S. M. 2010, ApJ, 718, 357

Ventura, P., Criscienzo, M. Di, Schneider, R., et al. 2012, MNRAS, 424, 3, 2345-2357

Wagner, J. S., Kan, J. R., & Akasofu, S.-I. 1979, J. Geophys. Res., 84, 891

Wallner, C., Faestermann, T., Gerstmann, U., et al. 2000, Nuclear Instruments and Methods in Physics Research B, 172, 333

Wallner, C., Faestermann, T., Gerstmann, U., et al. 2004, New Astron. Rev., 48, 145

Wallner, A., Faestermann, T., Feige, J., et al. 2015, Nature Communications, 6, 5956

Wallner, A., Bichler, M., Buczak, K., et al. 2015, Physical Review Letters, 114, 041101

Wallner, A., Feige, J., Kinoshita, N., et al. 2016, Nature, 532, 69

Wanajo, S., Nomoto, K., Janka, H. T., Kitaura, F. S., & Müller, B. 2009, ApJ, 695, 208

Wanajo, S., Janka, H.-T., & Müller, B. 2013, ApJ, 774, 1, L6

Wanajo, S., Sekiguchi, Y., Nishimura, N., et al. 2014, ApJ, 789, L39

Wasserburg, G. J., Busso, M., Gallino, R., & Nollett, K. M. 2006, NuPhA, 777, 5-69

Weingartner, J. C., & Draine, B. T. 2001, ApJ, 548, 296

Woosley, S. E., & Heger, A. 2015, ApJ, 810, 34

Zel'dovich, Y. B., & Raizer, Y. P. 1967, New York: Academic Press, 1966/1967, edited by Hayes, W.D.; Probstein, Ronald F.,

Zhao, F.-Y., Strom, R. G., & Jiang, S.-Y. 2006, ChJAA, 6, 635

Ziegler, J. F., & Biersack, J. P. 1985, Treatise on Heavy-Ion Science, by Bromley, D. Allan, ISBN 978-1-4615-8105-5. Springer-Verlag US, 1985, p. 93, 93

Ziegler, J. F., Ziegler, M. D., & Biersack, J. P. 2010, Nuclear Instruments and Methods in Physics Research B, 268, 1818

Zuckerman, B., & Webb, R. A. 2000, ApJ, 535, 959

Zuckerman, B., Song, I., & Webb, R. A. 2001, ApJ, 559, 388